

5929

JNCASR LIBRARY

5929



621.312 44 P08

JNCASR

5929

LIBRARY

Studies of Polymer based Solar Cells and Performance Limiting Factors

A Thesis

Submitted for the Degree of
DOCTOR OF PHILOSOPHY

by

DHRITIMAN GUPTA



CHEMISTRY AND PHYSICS OF MATERIALS UNIT
JAWAHARLAL NEHRU CENTRE FOR ADVANCED SCIENTIFIC
RESEARCH

(A Deemed University)
Bangalore – 560 064

SEPTEMBER 2008

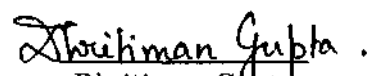
To my parents

621.312 44
POB

DECLARATION

I hereby declare that the matter embodied in the thesis entitled "**Studies of Polymer based Solar Cells and Performance Limiting Factors**" is an authentic record of research work carried out by me at the Chemistry and Physics of Materials Unit, Jawaharlal Nehru Centre for Advanced Scientific Research, Bangalore, India under the supervision of Prof. K. S. Narayan and that it has not been submitted elsewhere for the award of any degree or diploma.

In keeping with the general practice in reporting scientific observations, due acknowledgment has been made whenever the work described is based on the findings of other investigators.


Dhritiman Gupta



JAWAHARLAL NEHRU CENTRE FOR ADVANCED SCIENTIFIC RESEARCH

Jakkur, Bangalore 560064, India

K. S. Narayan

PHONE: 91 80 22082822

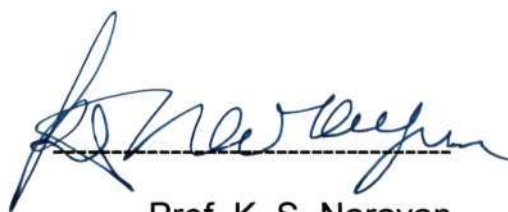
FAX: 91 80 22082766

E-MAIL: narayan@incasr.ac.in

September 4th 2008

Certificate

I hereby certify that the matter embodied in this thesis entitled “Studies of Polymer based Solar Cells and Performance Limiting Factors” has been carried out by Mr. Dhritiman Gupta at the Chemistry and Physics of Materials Unit, Jawaharlal Nehru Centre for Advanced Scientific Research, Bangalore, India under my supervision and that it has not been submitted elsewhere for the award of any degree or diploma.



Prof. K. S. Narayan

Acknowledgments

In my attempt to pursue my career as a graduate student, I have always been endowed with proper guidance, encouragements and supports. I would like to take this opportunity to acknowledge the contribution of those who stay behind the scene.

First of all I want to thank my research supervisor Prof. K. S. Narayan for giving me such an interesting topic to work on. His constant guidance, never ending enthusiasm and positive attitude has helped me to grow myself as an independent researcher. I am grateful to him for his invaluable suggestions and discussing and sharing innovative ideas relentlessly. His training has helped me to bring a positive change in my attitude and boosting my confidence. I am also sincerely thankful to his family members for their hospitality in home during festive seasons and support during my stay in JNCASR.

I want to thank our collaborator Prof. S. Ramakrishnan and his students Dr. Nagesh Kollishetty and Viswanathan. I am grateful to Prof. RK for many fruitful interactions and supports. It was really a treat to work with my collaborators Dr. Nagesh Kolishetty, Dr. Dinesh Kabra, Monojit Bag and Sabyasachi Mukhopadhyay.

I would like to thank Prof. C. N. R. Rao, FRS, Chairman of CPMU, JNCASR for being a source of inspiration and providing wonderful experimental facilities to carry out research work.

My all time companions in the lab were my colleagues. I was fortunate to have such a wonderful people as my labmates. I want to acknowledge our past lab members, Drs and seniors, A. G. Manoj, Soumya Dutta, Dinesh Kabra, Vasuda Bhatia, and my present labmates Arun, Manu, Monojit, Sachi, Shruti, Vini, Hemant, Jasmeet, Ankit, Radha, Shriram.

I would like to thank all the CPMU and TSU faculties and Dr. Satish Patil in

SSCU, IISc.

I would like to thank Mr. Srinath in electronics lab and Mr. Arokianathan in workshop. Their help was truly 'instrumental' .

All my friends and batchmates, Gopal, Surbhi, Gayatri, Jaita, Partha, Shibu, KP, Kiran, Subhra, Pradeepa, Keerti, Shrini, Snigdhadip, Ashish, Sairam, Saikrishna, Chandrasekhar, Ashishda, Motinda deserve an earnest thank for making my stay enjoyable. A special thank to Surbhi for taking pain in reading the manuscript of the thesis.

I want to thank Dr. Arup Roy for all his encouragements during the tough times and also for doing partial correction of this thesis.

Finally I owe my deep hearted gratitude to my parents and all other family members for their constant support and encouragements. They always have given priority to my interests and helped me to put a focussed effort. Without their support and encouragement this would not have been possible.

Preface

Polymer-polymer blend based bulk heterojunction solar cells are attractive due to their excellent miscibility, wide spectral response from both the donor and acceptor components and balanced charge carrier transport. Blend of variable band gap MEHPPV polymers as donors and cyano-PPV as acceptor forms an interesting system for studying energy transfer and charge transfer processes. This combination of polymers also enable harvesting of large part of solar spectrum. Studies on variable bangap MEHPPV based ternary blend devices and the role of different interfaces in the optoelectronic transport process is carried out. The energy funneling from a blue absorbing polymer to a green absorbing polymer and subsequent exciton dissociation at the donor-acceptor interface is shown to provide a viable route for photovoltaic devices having broad spectral response. In the blend films the contribution of different heterojunctions is identified and quantified using scanning photocurrent contrast microscopy. The fill-factor of the MEHPPV based devices reveal a general trend of value of 30% which is considered to be a direct outcome of low mobility prevailing in these materials.

Factors affecting the fill-factor in solar cells are addressed and identified under bulk and contact limited regime. The bulk material properties are known to affect the fill-factor in two possible ways, namely, a strong field dependence of exciton dissociation rate and unbalanced electron and hole mobility. An identifiable direct signature of these effects manifests in form of the shape of current density-voltage (JV) characteristics in the fourth quadrant. The strong field dependence of exciton dissociation rate can give rise to the characteristic 'S'-shaped current-voltage characteristics. A probable limiting factor for efficiency and fill-factors of organic solar cells originates from the cathode-polymer interface. We utilize various forms of cathode layer such as Aluminium (Al), Calcium (Ca), oxidized Ca and low melting point alloys in model systems to emphasize this aspect in our studies. The current-voltage response in the fourth quadrant indicates a general trend of convex shaped

JV-characteristics for illuminated devices with good cathode-polymer interfaces and linear or concave JV responses for inefficient cathode-polymer interfaces.

Power conversion efficiency estimates in organic solar cells have been found to be dependent on device active area. The scaling of efficiency with different active area has been addressed by studying these devices as a function of electrode area and incident beam size. Sources of current from the external region cannot be merely attributed to the optical effects such as, scattering in the ITO/polymer interface due to surface roughness and optical waveguiding inside ITO and Glass. Additional processes also appear to be contributing such as, lateral diffusion of the carriers around the periphery. Spatially resolved local photocurrent measurements outside the overlap region are employed to find the extent of lateral diffusion length of these charge carriers.

Publications

D. Gupta, D. Kabra, K. Nagesh, S. Ramakrishnan and K. S. Narayan, "An efficient bulk-heterojunction photovoltaic cell based on energy transfer in graded-bandgap polymers", *Advanced Functional Materials*, **17**, 226 (2007).

D. Gupta, M. Bag and K. S. Narayan, "Correlating reduced fill-factor in polymer solar cells to contact effects", *Applied Physics Letters*, **92**, 093301 (2008).

(Top 10 most downloaded articles in March 2008)

D. Gupta, S. Mukhopadhyay and K. S. Narayan, "Fill-factor in polymer solar cells", *Solar Energy Materials and Solar Cells* (2008), doi:10.1016/j.solmat.2008.06.001

D. Gupta, M. Bag and K. S. Narayan, "Size dependent efficiency in organic solar cells", (Communicated).

J. S. Chawla, **D. Gupta** and K. S. Narayan, "Semiconducting polymer coated single wall nanotube field-effect transistors discriminate holes from electrons", *Applied Physics Letters*, **91**, 043510 (2007).

Also selected for publication in *Virtual Journal of Nanoscience and Technology*, **16**(6) (2007).

K. Nagesh, **D. Gupta**, D. Kabra, S. Ramakrishnan and K. S. Narayan, "Tunable two-colour patterning of MEHPPV from a single precursor", *Journal of Materials Chemistry*, **17**, 1682 (2007).

V. Bhatia, **D. Gupta**, D. Kabra and K. S. Narayan, "Optical and electrical features of surface ordered regio-regular polyhexylthiophene", *Journal of Material Science*,

18, 925 (2007).

M. Bag, **D. Gupta**, N. Arun and K. S. Narayan, "Deformation of conducting metallic liquid drop in electric field for contacts in molecular electronics", (Communicated).

RESEARCH NEWS

"Plastic Solar cell makes light work", Chemistry World, 24th July 2006

List of Figures

1.1	List of important polymers for solar cell application	5
1.2	Degenerate ground state of polyacetylene and soliton	6
1.3	Heterojunctions	6
1.4	Schematic representation of carrier photogeneration process	10
1.5	Schematic diagram showing fate of an exciton at the heterojunction	10
1.6	Schematic representation of Gaussian DOS	19
1.7	Mobility spatial distribution function	19
1.8	Polymer solar cell architectures	30
1.9	Current status of solar cell efficiency values	30
2.1	Schematic representation of device operation under external voltage sweep	38
2.2	Schematic representation of photo-physical processes under short- circuit and open-circuit condition	46
3.1	Regioregular and regiorandom P3HT	56
3.2	P3HT chain-orientation on functionalized substrates	57
3.3	Grazing angle X-ray diffraction of oriented P3HT chains	57
3.4	Chemical structure of MEHPPV and CNPPV and the absorption spectra	60
3.5	Chemical structure and HOMO, LUMO levels of PCBM	60
3.6	Chemical structure of PEDOT/PSS	62
3.7	Schematic diagram of patterning procedure of the active polymer layer	65
3.8	Electroluminescence spectra of HC and LC	65
3.9	Solar cell IV-measurement set up	68
3.10	Intensity modulated photocurrent measurement set-up	68
3.11	Wide-field photocurrent contrast microscopy set-up	71

3.12	Spatially resolved photocurrent scan in 1D	71
3.13	Time of flight signal of MEHPPV devices	73
3.14	Set-up for transient photocurrent measurements	74
4.1	Chemical structures of variable band gap MEHPPV polymers	80
4.2	Absorption and photoluminescence spectra of HC and LC	80
4.3	Absorption spectra of polymer blends	82
4.4	Photoluminescence spectra of polymer blends	82
4.5	PL quenching efficiency of HC:CNPPV and LC:CNPPV blends	85
4.6	IPCE of ternary polymer blend device	85
4.7	Schematic representation of the photophysical process in the active polymer layer	87
4.8	Derivative of photocurrent and absorption profile	87
4.9	Wide-field photocurrent contrast images of ternary polymer blend	91
4.10	Histogram plot of area fractions contributing to the photocurrent	91
4.11	Current-voltage characteristics of solar cell devices	93
4.12	Postulated blend morphology for near ideal photovoltaics	95
4.13	PL spectrum of vertically graded HC-LC composite	95
5.1	Donor acceptor pairs with balanced mobility-lifetime product	100
5.2	Schematic diagram of photocurrent in the fourth quadrant plotted in log-log scale	102
5.3	Field dependence of photocurrent	102
5.4	JV-characteristics of Al cathode device	104
5.5	JV-characteristics of a Ca-cathode device	104
5.6	AFM topography image of Al electrode	106
5.7	Thickness dependence of FF	106
5.8	JV-characteristics of MEHPPV-CNPPV blend solar cell	109
5.9	Low melting point alloy as a printable cathode	109
6.1	JV characteristics and area-scaling	113
6.2	Area scaling of J_{SC} in second set of samples	113
6.3	IV-characteristics with restricted and flooded illumination	114
6.4	Schematic diagram of optical scattering inside the substrates	116
6.5	Intensity profile of the light spot focused on the substrate	116

6.6	Simulation of spreading of lightspot inside polymer medium using Fourier optics formalism	117
6.7	Spatially resolved photocurrent scanning on ITO electrode	119
6.8	Spatially resolved photocurrent scanning on Al electrode	119
6.9	Photocurrent measurement with two light probes	120
6.10	Variation of J_{SC} with different sized spot illumination	120
A.1	Photocurrent contrast and confocal microscopic images of ternary blend devices containing non-solvent	130

Contents

Preface	vii
List of Figures	xiii
1 Introduction	1
1.1 Historical background	1
1.2 Photogeneration of charge carriers	4
1.2.1 Exciton dissociation in blends of polymers	7
1.3 Transport of charge carriers	12
1.3.1 Time of flight (TOF) technique	14
1.3.2 Gaussian disorder model (GDM)	17
1.3.3 Space-charge limited TOF current transients	23
1.3.4 Distribution of mobility in thin films	25
1.4 Optoelectronic device perspective	26
1.4.1 Polymer field effect transistor (PFET)	27
1.4.2 Organic light emitting diode (OLED)	27
1.4.3 Photodetectors and solar cell	29
1.4.4 Device architecture and current status	31
1.5 Thesis outline	34
2 Organic/Polymer Solar Cells	37
2.1 Introduction	37
2.2 Device operation and electrical characterization	37
2.3 Physical processes in BJH-OSC under zero external field	39
2.4 Theoretical modeling: drift-diffusion equation	43
2.5 Steady-state space charge effect	49

2.6	Summary	53
3	Materials, Fabrication and Measurements	55
3.1	Introduction	55
3.2	Materials	56
3.2.1	Poly(3-hexylthiophene)(P3HT)	56
3.2.2	Poly[2-methoxy-5-(2-ethylhexyloxy)-1,4-phenylene vinylene]	59
3.2.3	[6,6]-phenyl-C ₆₁ -butyric acid methyl ester	61
3.3	Device fabrication method	63
3.4	Measurements	66
3.4.1	Absorption coefficient and photoluminescence (PL) measurement	66
3.4.2	Solar cell JV-characteristics measurements	67
3.4.3	Intensity modulated photocurrent spectroscopy (IMPS)	69
3.4.4	Wide-field photocurrent microscopy	70
3.4.5	Spatially resolved photocurrent scan in 1D	72
3.4.6	Transient photocurrent measurements	74
3.4.7	Grazing incidence X-ray diffraction (GIXRD) measurement	75
4	Efficient polymer solar cell based on energy transfer in graded-bandgap polymers	77
4.1	Introduction	77
4.2	Variable band gap donor systems	79
4.2.1	Absorption and PL spectra of the blend	81
4.3	Intensity modulated photocurrent spectra	83
4.4	Wide-field photocurrent imaging of ternary blend device	90
4.5	JV-characteristics	92
4.6	Summary	94
5	Correlating contact effects to the reduced Fill-Factor	97
5.1	Introduction	97
5.2	Field dependence of photocurrent	101
5.3	Cathode-polymer interface effect on FF	103
5.4	MEHPPV-CNPPV blend device	107
5.5	Interface manipulation with meltable cathode	108

5.6 Summary	110
6 Effect of cathode dimension and geometry on performance of solar cell	111
6.1 Introduction	111
6.2 P3HT:PCBM solar cell characteristics	112
6.3 Optical effects	115
6.4 Spatially resolved photocurrent scan	118
6.5 Summary	123
7 Summary and Future Directions	125
Appendix to Chapter 4	129
References	133

CHAPTER 1

INTRODUCTION

1.1 Historical background

Polymers are generally insulating materials and were known for the huge applicability of these in “plastics” which are widely used as substitutes for traditional materials like wood, ceramics and metals. Plastics were technologically less attractive until 1977, when Alan Heeger, Alan McDiarmid, H. Shirakawa invented a hugely potential form of material called “conducting polymers” [1]. The discovery fetched them the year’s Noble prize in Chemistry in 2000, as well as opened up the gateway of fourth generation electronics called “organic polymer based electronics” [2, 3]. As compared to the inorganic silicon based technology, this new technology is still in its adolescence. The performance of organic-based devices is certainly not comparable to that of the silicon technology, but it has its own unique set of characteristics to offer. Combination of semiconducting electronic property and mechanical aspects similar to plastics give it an edge over the inorganic silicon based technology where mechanical flexibility is difficult to achieve.

A major breakthrough in the field of organic electronics is the 1986 report by C. W. Tang at Kodak of the first solar cell based on conjugated organic molecule [4]. This was followed by the phenomenal discovery of electroluminescent organic device made of multilayers of vacuum-deposited dye films in 1987 by Tang and Vanslyke [5]. Shortly thereafter Sir Richard Friend and his group in Cambridge

discovered electroluminescence in a conjugated polymer system [6]. After almost 10 years of the first report of organic solar cell, Heeger and his group discovered photovoltaic effect in an intermixed polymer network [7], thereby opening the path for the fabrication of organic solar cells. Polymer field effect transistors from small conjugated oligomers [8, 9, 10] was also a major breakthrough in this field. Since then a steady progress has been observed with prototype devices performing at par with their inorganic counterpart. Integrated transistor driven display was one of the early breakthroughs [11, 12, 13]. The solution processibility of these conjugated polymer enabled their use in the form of polymer-blends as the active material in development of photodetectors [14], colour-sensors [15, 16], all-polymer integrated circuits [17], light emitting FETs [18], and radio-frequency identification circuitry [19]. With the recent noteworthy advancements like, spatially controlled light emitting ambipolar FET [20], an organic rectifier circuit working in MHz frequency range [21] and logic circuits based on flexible woven substrates [22], organic electronics has found its own niche in the development of semiconductor industry.

Conjugated polymers as opposed to their insulating saturated counterpart have interesting electronic properties. 'Conjugated' meaning the alternative double ($\sigma+\pi$) and single (σ) bond in the backbone. The simplest conjugated polymer is polymerized form of acetylene $(\text{CH})_x$ known as polyacetylene (PA). There are two conformational isomers of this polymer, viz. cis-PA and trans-PA. In trans-PA single bonds result from the overlap between sp^2 -hybrids and double bonds comprise of an sp^2 σ -bond and a π -bond (resulting from overlap of p_z electrons of the neighbouring atoms in the direction normal to the x-y plane in which zig-zag polymer chain lies). Since π -electrons are easily available for conduction we may think that there is one valence electron per repeated CH-unit. This implies PA is a quasi one dimensional metal. Quasi 1D metals tend to distort spontaneously

(structurally) [23] such that the spacing between the successive atoms along the chain is modulated and this distortion leads to a pairing of successive sites along the chain or dimerization. The dimerization opens up an energy gap at the Fermi surface, thereby lowering the energy of occupied states and stabilizing the distortion. The competition between the lowering of the electronic energy and the increase in elastic energy of the polymer (caused by distortion) leads to an equilibrium bond-length modulation which is of the order of 0.003-0.004 nm in PA. Thus the lattice instability removes the high-density of states at the Fermi-surface and renders the system a semiconductor.

Conjugated polymers can be divided into two classes, those with a non-degenerate ground state and a degenerate ground state. As shown in the Figure 1.2, the polyacetylene chain can be dimerized in two distinct patterns (A or B) both having the same energy. Hence the ground state is doubly-degenerate. Therefore structural defects that are interfaces between these two patterns may occur. Such a bond alteration defect is called soliton. A soliton can be delocalized over the polymer chain. Most of the fluorescent, light emitting polymers (generally used in organic light emitting diodes (OLEDs)) contain phenyl rings and have non-degenerate ground state (C) (Figure 1.2).

In order to increase the conductivity polymers can also be doped to generate excess number of quasiparticles but in a completely different manner as compared to the conventional semiconductors. In conjugated polymers, doping implies a chemical redox reaction that involves partial addition or removal of electrons to/from the conjugated backbone. Typically there are three ways to dope a conventional conjugated polymer: (i) chemical doping, (ii) photogeneration and (iii) charge injection. Chemical doping is done with electron donors (e.g. Na) or acceptors (e.g. AsF_5 or I_2). From photovoltaics point of view the optical doping is most relevant.

We shall discuss this in detail in the following section.

1.2 Photogeneration of charge carriers

Conjugated polymers have a band gap lying in the range of 1 eV to 3 eV. Photoexcitation gives rise to formation of quasi particles called “exciton” which consists of electron-hole pair with some lattice deformation. The dielectric constant of the organic materials is lower ($\epsilon_r \sim 3-4$) compared to inorganic semiconductors ($\epsilon_r \sim 12$). The binding energy of the excitons in the organic materials are $\sim 0.4 - 1$ eV [24] (which corresponds to a coulomb radius of $r_c \sim 1$ nm) as compared to their inorganic counterpart where it is mostly Wannier-like with large coulomb radius (> 10 nm) and low binding energies ~ 10 meV. The weak intermolecular interaction in some conjugated polymer systems promote the generation of Frenkel type excitons with mostly singlet character (one up spin and one down spin, with net spin zero). However singlet excitons can give rise to triplet states with total spin one (both up or both down, with net spin one) by a non-radiative process called the inter-system crossing (ISC). The transition from triplet excited state to singlet ground state violates the rule of no change of electron spin during change of electronic state and is therefore called a spin forbidden transition. This transition is prompted by spin-orbit coupling through the presence of doped heavy atoms in the polymer matrix. Triplet states are lower energy states and have longer lifetime. Dissociating triplet excitons into free electrons and holes can also provide a viable route to better PV-devices [25].

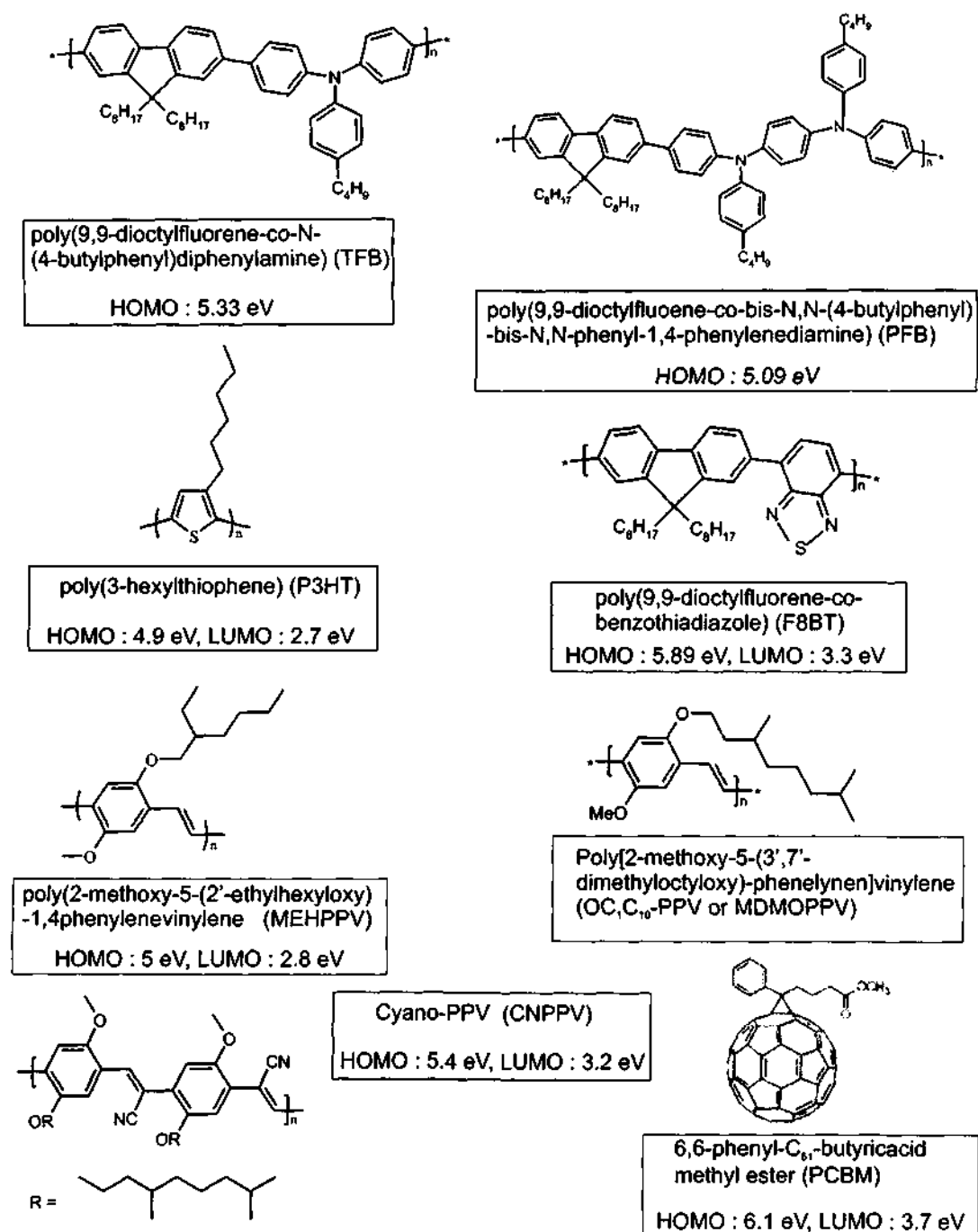


Figure 1.1: List of important donor (MEHPPV, P3HT, PFB, TFB, MDMO-PPV) and acceptor (CNPPV, PCBM, F8BT) kind of polymers with their highest occupied molecular orbital (HOMO) and lowest unoccupied molecular orbital (LUMO) levels.

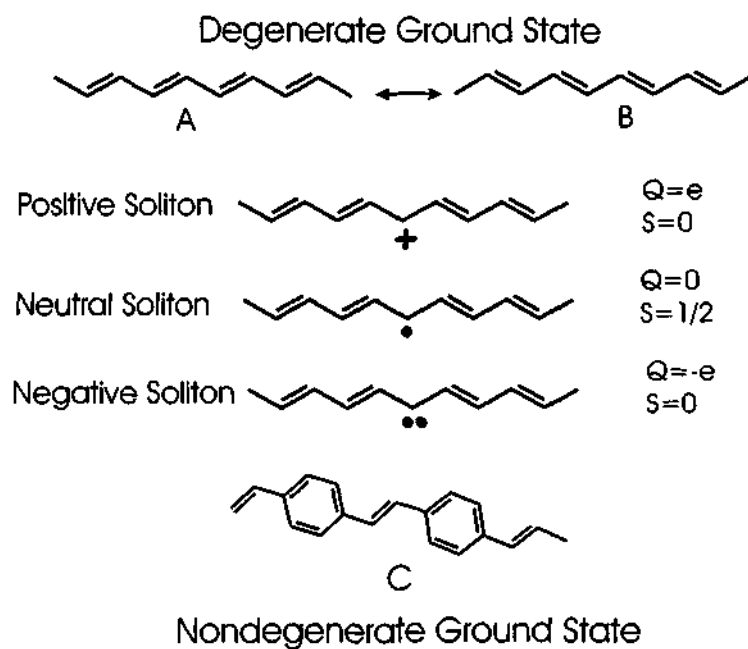


Figure 1.2: Schematic representation of degenerate and non-degenerate ground state in conjugated polymers.

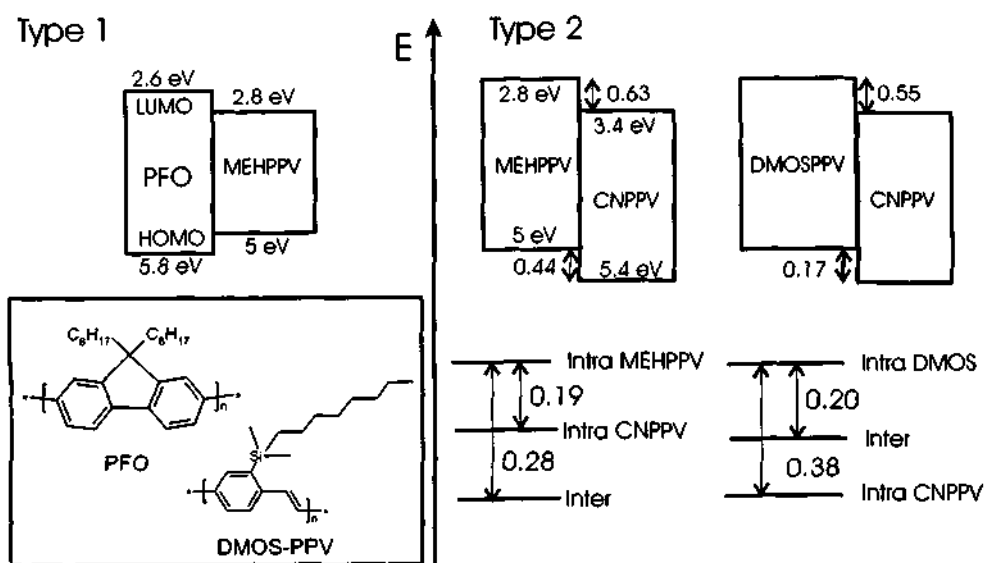


Figure 1.3: Two types of heterojunctions are shown. In Type 1 heterojunction energy transfer is seen [26] and in Type 2 heterojunction either energy transfer or charge transfer can take place depending upon the relative energy of intra-chain and inter-chain excitons [27].

1.2.1 Exciton dissociation in blends of polymers

In order to get current from the device the photogenerated excitons have to be dissociated into free charge carriers. The only way to raise the yield of photoionization is by doping with electron acceptors or donors. The close intermixing of donor-acceptor (D-A) kind of polymers gives rise to the heterojunction in molecular level. Heterojunctions can be of two different types depending on the relative position of the HOMO and LUMO levels (Figure 1.3). (i) In type 1 heterojunction the bandgap of acceptor is nested within the bandgap of the donor polymer (straddling gap). In these systems, excitons from the high band gap polymer (donor) can be non-radiatively transferred to the low band gap polymer (acceptor) by dipole-dipole coupling provided there is a good overlap between the absorption spectrum of donor and photoluminescence spectrum of the acceptor [26]. (ii) In type 2 heterojunction both the ionization potential (IP) and the electron affinity (EA) of the donor is higher than that of the acceptor (staggered gap). These kind of heterojunctions are the prerequisite for efficient exciton break-up by charge transfer reaction at the interface. The condition for efficient charge transfer is $(E_g^{\text{donor}} - E_{\text{ex}}) > (\text{IP}_{\text{donor}} - \text{EA}_{\text{acceptor}})$, where E_{ex} is the binding energy of the exciton [28].

However in few cases energy transfer is a favourable process in type 2 heterojunctions consequently, the device show low photocurrent yield and high luminescence quantum yield leading to very efficient OLEDs [29]. The energy or charge transfer takes place depending on the relative energies of the intra A-chain and intra D-chain exciton and interchain or charge-transfer (CT) exciton (coulombically bound e-h pair with electron in the acceptor chain and hole in the donor chain). This was demonstrated for MEHPPV-CNPPV and DMOSPPV-CNPPV interfaces [27]. In the DMOSPPV-CNPPV interface the lowest energy state is the intra-CNPPV

exciton (Figure 1.3). Hence the exciton prefers to be transferred completely in the CNPPV chain (energy transfer). In the MEHPPV-CNPPV interface the lowest energy state is the CT-excitonic state. Hence this interface facilitates charge transfer. The CT-exciton in type 2 heterojunction is bound by strong coulomb interaction. Its dissociation requires additional energy.

The fate of a bound CT-state is either to decay to ground state by radiative/noradiative recombination channel or to escape the mutual Coulombic potential by electric field (F) and temperature (T) activated diffusion process. The first ever theory to calculate the probability that two oppositely charged carriers are separated by an external electric field as a function of initial separation r_0 and orientation of the field θ , was given by L. Onsager [30, 31]. Onsager calculated the probability of escaping recombination of a coulombically bound e-h pair with initial separation distance r_0 which undergo a Brownian random walk under the combined influence of their mutual coulomb attraction and external electric field. The dissociation probability is given by (Equation 1.1).

$$P_\epsilon(r_0, \theta, T, F) = e^{-(A+B)} \sum_{m,n=0}^{\infty} \frac{A^m}{m!} \frac{B^{m+n}}{(m+n)!} \quad (1.1)$$

where $A = 2\rho/r_0$, $B = \beta r_0(1 + \cos \theta)$, $\rho = e^2/8\pi\epsilon\epsilon_0 k_B T$, $\beta = eF/2k_B T$, F is the electric field and k_B is the Boltzmann constant. Here θ represents the orientation of applied field F , with respect to the radius vector r between e-h pair. Defining $g(r, \theta)$ as the distribution of initial separation distance of the thermalized geminate carriers, the quantum efficiency of charge carrier generation is derived as

$$\eta = \phi_0 \int P(r_0, \theta, T, F) g(r_0, \theta) d^3r \quad (1.2)$$

where ϕ_0 is the yield of thermalized pairs per absorbed photon. This theory

considered only thermalized carriers and does not incorporate any carrier dynamics during thermalization.

Braun [32] extended Onsager's theory by pointing out that electron-hole (e-h) pair has a finite lifetime determined by its phonon-assisted non-radiative decay rate k_f to the ground state. It implies that an initially optically excited ionized state $\{A^-D^+\}$ has many chances for ultimate dissociation before it relaxes (Figure 1.4). The e-h pair can separate into free carriers with electric field dependent rate constant $k_{\text{diss}}(F)$. In Braun's model, the probability that a bound polaron pair dissociates into free electron and hole is given by Equation 1.3,

$$P(r, F, T) = \frac{k_{\text{diss}}(F)}{k_{\text{diss}}(F) + k_f} \quad (1.3)$$

The dissociation rate k_{diss} depends on carrier mobility. As a result dissociation efficiency also depends on charge carrier mobility. A hugely successful donor-acceptor system is a PPV-type donor blended with fullerene (C_{60}) or a soluble derivative of it, such as (6,6)-phenyl- C_{61} -butyric acid methyl ester (PCBM). Charge transfer reaction takes place in this blend within 45 fs timescale [33]. This ultrafast charge transfer makes this system suitable as active layer material for photovoltaics. High photocurrent density ($\sim 10 \text{ mA/cm}^2$) achieved from these systems proves that the majority of the photogenerated charge carriers escape recombination and get collected in the electrodes facilitated by the built-in electric field. Using Braun's formalism, the observed high quantum efficiency ($\sim 60 \%$) was modeled by Mihailetschi et. al. [34]. Experimentally observed electric field dependence of photocurrent was modeled based on broad distribution of e-h pair distances centered at 1.3 nm and using $1/k_f \sim 1 \mu\text{s}$. The probability factor given by Equation 1.3 was integrated over the distribution of separation distance to achieve the total probability.

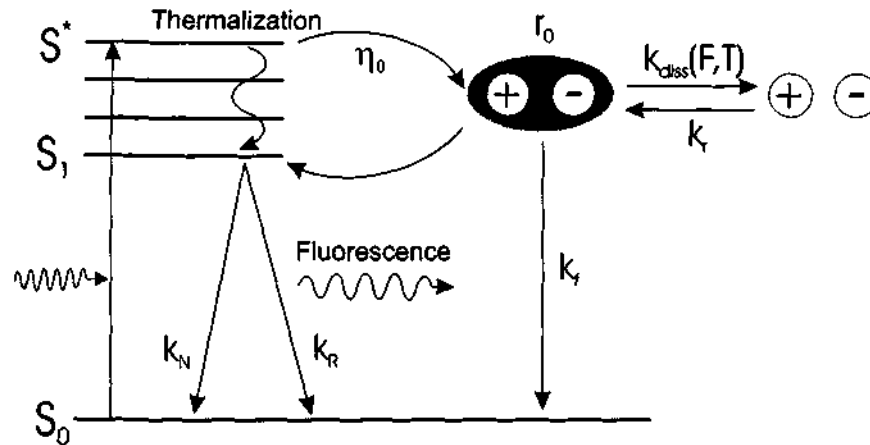


Figure 1.4: Schematic representation of carrier photogeneration process as described by Onsager model [31] and later modified by Braun [32]. The carrier after bimolecular recombination is not essentially lost but it can form an intermediate bound polaron pair which can act as a precursor for free charge carrier generation.

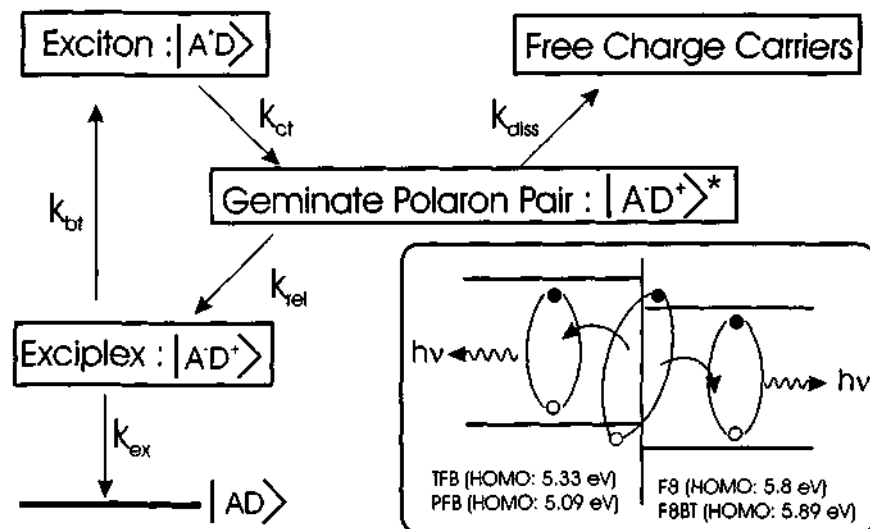


Figure 1.5: Above scheme summarizes the fate of an exciton at the interface. Photogenerated exciton gets dissociated and form geminate polaron pair with rate constant k_{ct} . This geminate pair can either relax into a lower energy luminescent state, called exciplex (k_{rel}) or can dissociate (k_{diss}). The exciplex state then can either decay to ground state (k_{ex}) or it can back transfer to a bulk exciton in the donor or acceptor chain (k_{bt}). The energy difference between F8BT exciton and TFB/F8BT exciplex state is 0.12 eV, PFB/F8BT exciplex is 0.25 eV [29, 35]. The exciplex formed between PFB/F8, backtransfers as bulk exciton in PFB chain [36].

$$P(T, F) = N_f \int_0^{\infty} P(x, T, F) f(x) dx \quad (1.4)$$

where $f(x) = x^2 e^{-x^2/a^2}$ is the distribution function of donor-acceptor separation and $N_f = 4/\pi^{1/2} a^3$ is the normalization factor. The electron mobility and hole mobility was in the range of $\mu_e = 2.0 \times 10^{-7} \text{ m}^2/\text{Vs}$ and $\mu_h = 1.4 \times 10^{-8} \text{ m}^2/\text{Vs}$. Both Onsager and Braun's theory however disregard any temperature or field activated process to regenerate bulk excitons from geminate e-h polaron pair at the donor-acceptor interface.

This phenomenon was demonstrated by Morteani et. al. in blends of poly(9,9-dioctylfluorene-co-benzothiadiazole) (F8BT) with poly(9,9-dioctylfluorene-co-bis-N,N-(4-butylphenyl)diphenylamine) (PFB) and F8BT with poly(9,9-dioctylfluorene-co-N-(4-butylphenyl)diphenylamine) (TFB). These two blend systems revealed quite different characteristics. In PFB:F8BT blends, the heterojunction is efficient for high charge separation yields (4 % photocurrent external quantum efficiency) and low electroluminescence (EL) efficiencies ($< 0.64 \text{ lm/W}$), whereas TFB:F8BT systems display low photocurrents but very high EL efficiencies [29, 37, 38]. These observations prompted the proposition of formation of an intermediate excitonic species termed as 'exciplex' in these blend systems [29, 39, 40]. Exciplexes possess both intramolecular excitonic character as well as intermolecular charge-transfer character and have lower energy than the charge transfer state. The long radiative decay times of these species promotes the endothermic transfer to bulk exciton [35, 36]. In photovoltaic device, this endothermic energy transfer (exciplex \rightarrow exciton) 'regenerates' the bulk exciton and provides one of the lossy pathway. Upon optical excitations there can be three kind of photogenerated species existing in the interface: (i) "primary" excitons generated in the bulk by optical excitation,

(ii) exciplexes, generated from the bulk exciton, (iii) “secondary” excitons, generated via endothermic back transfer from the exciplexes. Each of these excitations contribute to the zero-field PL. Geminate e-h pair thus can either dissociate into free charge carriers with rate constant k_{diss} or it can relax into luminescent exciplex state with rate constant k_{rel} . The ratio $k_{\text{diss}}/k_{\text{rel}}$ is strongly field dependent and determines the degree of luminescence quenching (Figure 1.5).

Free charge carrier generation yield is therefore hugely dependent on these branching ratios and interfaces between polymers also play crucial role. The separation probability strongly depends on mobility numbers of the individual donor and acceptor components. Separated hole polaron (hereafter referred to as hole) and electron polaron (hereafter referred to as electrons) transport through the polymer chains is markedly different from the conventional band-transport that exist in crystalline semiconductors. A semiconducting polymer chain is always associated with structural defects likes kinks and twists which give rise to variation in conjugation length and interaction energies. This give rise to energetic spread in the transport sites. In the following section we shall give a brief overview of the charge carrier transport in organic materials.

1.3 Transport of charge carriers

Transport in conjugated polymer is largely akin to the disordered or amorphous material due to their aperiodic crystal structure. Unlike well defined band structure of crystalline solids, localized energy states are likely to appear within bandgap of disordered systems. As a consequence, the transport occurs via “hopping” between energetically accessible sites. “Hopping” essentially means “phonon assisted quantum mechanical tunneling”. Charge carriers hop between the states either by

absorbing or by emitting phonons which dictate the upward or downward jump respectively in the energy landscape. A carrier may either hop a small distance with high activation energy (energetic distance between the sites) or hop over a long distance with low activation energy. With lowering temperature, the phonon gets frozen, minimizing the probability of a carrier to hop to a higher energetic nearest neighbour. At this stage, carriers tend to hop to a larger distance rather than to the nearest neighbour. This process is called the “variable range hopping mechanism”. The temperature dependence of carrier transport strongly depends on the density of the localized states. Mott dealt with the hopping transport in a constant density of states (DOS) where he considered the hopping over large distance and hopping to high energies as equally important [41]. In such a system, the temperature dependence of conductivity σ is given by,

$$\sigma = \sigma_0(T) \exp \left[-(T_0/T)^{\frac{1}{1+d}} \right] \quad (1.5)$$

where d is the dimensionality of the system and $T_0^{3d} = c/k_B N(E_F)L^3$ with c is the proportionality constant, k_B is the Boltzmann constant, $N(E_F)$ is the density of states at the Fermi level and L is the localization length. Later Miller and Abraham proposed a hopping model [42]. The hopping rate from occupied site i to unoccupied localized state j depends on the height of the energetic barrier ($\epsilon_i - \epsilon_j$) and the distance r_{ij} (Equation 1.6):

$$\nu_{ij} = \nu_0 \exp \left(-2\gamma a \frac{r_{ij}}{a} \right) \times \begin{cases} \exp \left(-\frac{\epsilon_j - \epsilon_i}{kT} \right) & \text{for } \epsilon_j > \epsilon_i, \\ 1 & \text{for } \epsilon_j < \epsilon_i \end{cases} \quad (1.6)$$

The frequency pre-factor ν_0 is called the attempt-to-hop frequency, r_{ij} is the

jump distance between site i and j (normalized to the intersite distance a). $2\gamma a$ controls the electronic coupling among the hopping sites through exchange interaction. Adequate attempts have been made to obtain the conductivity in disordered materials considering different DOS. The shape of the DOS is important for the description of the charge transport because it reflects the disorder of the sample. In case of organic semiconductors, the shape is often assumed to be a Gaussian. Before discussing the theoretical approaches to explain the experimental observations, we shall briefly review the experimental techniques to study the transport properties in organic solids. The most important experimental parameter to describe the transport is the charge carrier mobility and its dependence on electric field and temperature. Among several other techniques to measure charge carrier mobility, time-of-flight technique stands out to be the most primitive one.

1.3.1 Time of flight (TOF) technique

The most useful way to extract mobility from photocurrent transients was time of flight (TOF) method. In TOF method, a thick film (thickness $d \sim \text{few } \mu\text{m}$) of amorphous organic material, sandwiched between two electrodes, one of them essentially a blocking contact, is illuminated by a short pulse of laser light which generates a sheet of charge carriers (in order to ensure surface photogeneration, αd should be $\gg 1$, where α is the absorption coefficient) that traverses through the sample thickness d under the external applied voltage (V) and gets collected in the counter electrode. The resultant photocurrent transient give rise to the current spike, immediately after the onset of the light pulse, followed by a constant current region or so called 'plateau' region, then a 'shoulder' region and finally a long decaying 'tail'. The 'shoulder' or the onset of the tail region gives the estimate of

the carrier traversal time t_{tr} . The mobility μ [cm^2/Vs] is given by Equation 1.7,

$$t_{tr} = d^2/\mu V \quad (1.7)$$

The ‘plateau’ is the signature of the constant drift velocity of the carrier packet and under this condition the transport is considered to be nondispersive. Conversely if the drift velocity of a sheet of carriers started at $t = 0$ at the front electrode decreases as the packet traverses the sample, a plateau is not observed and the transients become featureless and the transport is called dispersive. Hence the mean arrival time of carriers becomes an ill-defined quantity and difficult to extract from the transient curves.

In order to extract the carrier transit time in case of dispersive transport it is imperative to plot the photocurrent transient in log-log scale as proposed by Scher and Montroll in the theory developed for amorphous inorganic materials [43]. Plotting the time dependence of current in a double logarithmic scale reveals plots intersecting at $t = t_{tr}$,

$$\begin{aligned} I(t) &\sim \text{const} \times t^{-(1-\alpha)} \quad \text{for } t/t_{tr} < 1 \\ &\sim \text{const} \times t^{-(1+\alpha)} \quad \text{for } t/t_{tr} \gg 1 \end{aligned}$$

with $0 < \alpha < 1$ is the dispersion parameter. The slopes of these two portions add up to give a value = -2. The photocurrent transients when plotted in a log-log scale also reveal an interesting ‘shape invariance’ to the electric field and sample thickness. For different applied field and temperature the plots of $\ln[i(t)/i(t_{tr})]$ Vs t/t_{tr} superpose on each other. This invariance of the shape of the photocurrent transients was designated as ‘universality’ by Scher and Montroll [43]. This univer-

sal current trace was first quantitatively demonstrated by Scharfe et. al. [44, 45] by their study on amorphous arsenic triselenide. One more important aspect of their study was the revelation that the plot of $1/t_{tr}$ Vs F/L (L is the sample thickness) yields a straight line with slope $\simeq 2$, i.e, $t_{tr}^{-1} \propto (F/L)^2$. Hence the mobility as derived from Equation 1.7 becomes proportional to (F/L) . Dependence of carrier drift mobility on sample thickness is the most unusual thing and was ascribed as 'anomalous transport properties' which could not be explained by traditional concept of statistical spreading of a propagating Gaussian carrier packet. Scher and Montroll developed a transport model for $I(t)$ which describes the dynamics of a carrier packet executing a time-dependent random walk in presence of an external field and an absorbing boundary. The time dependence of the random walk was governed by hopping time distribution $\psi(t)$. The dispersion of the hopping time distribution was proposed to be a inverse power law (Equation 1.8)

$$\psi(t) \sim \text{const} \times t^{-(1+\alpha)}, \quad 0 < \alpha < 1 \quad (1.8)$$

This assumption originated from the fact that in an amorphous material there is large dispersion in the separation distance between the hopping sites or the so called 'positional disorder' of the hopping sites. Hence the waiting time between two successive hops has broad distribution given by Equation 1.8. As a consequence, mean carrier of the propagating packet moves with a velocity which decreases with time as it gets separated from the peak which remains fixed at the point of origin ($\sigma_x/\langle l \rangle \approx t^{-(1+\alpha)}$, where, $\langle l \rangle = \langle x \rangle$ is the mean particle displacement and $\sigma_x^2 = \langle (x - \langle x \rangle)^2 \rangle$ is the variance). This is contrary to the Gaussian transport where, the peak of the Gaussian packet and the mean carrier packet are located in the same position and move with same velocity ($\sigma_x/\langle l \rangle = \text{const.}$).

1.3.2 Gaussian disorder model (GDM)

Amorphous inorganic materials has many commonality with the disordered polymeric materials. Therefore Scher and Montroll method, when applied to disordered polymeric systems could successfully explain many of the transport features albeit few drawbacks. It does not take into account the fluctuations in the site energy or the ‘energetic disorder’ and fails to explain the temperature dependence of the dispersive nature of the transients as has been observed experimentally in many disordered solids. Furthermore, for several systems, deviation from universality were observed depending on the temperature [46, 47]. The tail broadening parameter W (Equation 1.9) of the TOF signals which is the measure of the degree of dispersion also revealed interesting properties at different temperature. W is defined as,

$$W = \frac{(t_{1/2} - t_0)}{t_{1/2}} \quad (1.9)$$

where $t_{1/2}$ is the time for the transient to decay to one-half of its plateau value and t_0 is time defined by the intersection of the asymptotes of the plateau and trailing edge of the transient. The thickness dependence of W at constant field often revealed controversial behavior. For N,N'-diphenyl-N,N'-bis(3-methylphenyl)-(1,1'-biphenyl)-4,4'-diamine (TPD) doped polycarbonate, Yuh and Stolka [48] showed that W scales approximately as $L^{-1/2}$ ($18 \leq L \leq 70 \mu\text{m}$), while the measurements on p-diethylaminobenzaldehyde diphenylhydrazone (DEH) doped polystyrene by Schein et. al. [49] revealed L independence ($W \approx 0.4$, for $3 \leq L \leq 40 \mu\text{m}$). Borsenberger et. al. [50] related the dispersion W of a nondispersive TOF signal to the energetic disorder parameter ($\sigma_E/k_B T$) of the sample and showed that the functional dependence of W on L undergoes a characteristic change from a W

$\propto L^{-1/2}$ (at lower value of $\sigma_E/k_B T$) to $W = \text{constant}$ (at large value of energetic disorder, $\sigma_E/k_B T > 4$). Experimentally the constant behavior was observed at 180 K, while at 298 K the behavior changed to inverse square root dependence. It prompted the prediction that the scaling behavior stems out as an inherent property of transport processes involving Gaussian-type energetic disorder and is not bound to the observation of what was conventionally referred to as dispersive transport, although both the phenomena have the same physical origin.

In order to explain the observed temperature behavior Bassler [51, 52] proposed a model for charge transport using the distribution of localized states as Gaussian (Figure 1.6). The energy of hopping sites was derived from the Gaussian distribution with standard deviation σ_E (Equation 1.10).

$$\rho(\varepsilon) = (2\pi\sigma_E^2)^{-1/2} \exp\left(-\frac{\varepsilon^2}{2\sigma_E^2}\right) \quad (1.10)$$

The degree of energetic disorder is specified by $\sigma_E (= \langle(\varepsilon - \langle\varepsilon\rangle)^2\rangle^{1/2})$ and is termed as diagonal disorder. Experimental values of σ_E are in the range of 70-150 meV ($\sigma_E/k_B T \sim 3-6$ at room temperature). The hopping rate between sites i and j is given by Equation 1.6.

In order to introduce off-diagonal disorder (exchange interaction among the two sites to fluctuate in a random manner), the wave function overlap parameter $2\gamma a$ in Equation 1.6 was expressed by the sum of two site-specific contributions, $2\gamma a = \Gamma_{ij} = \Gamma_i + \Gamma_j$, each varying randomly according to a Gaussian probability density of standard deviation $\delta\Gamma$. The variance of Γ_{ij} ($\Sigma = \sqrt{2}\delta\Gamma$) is called the off-diagonal disorder. The relaxation of the carrier, generated randomly within an

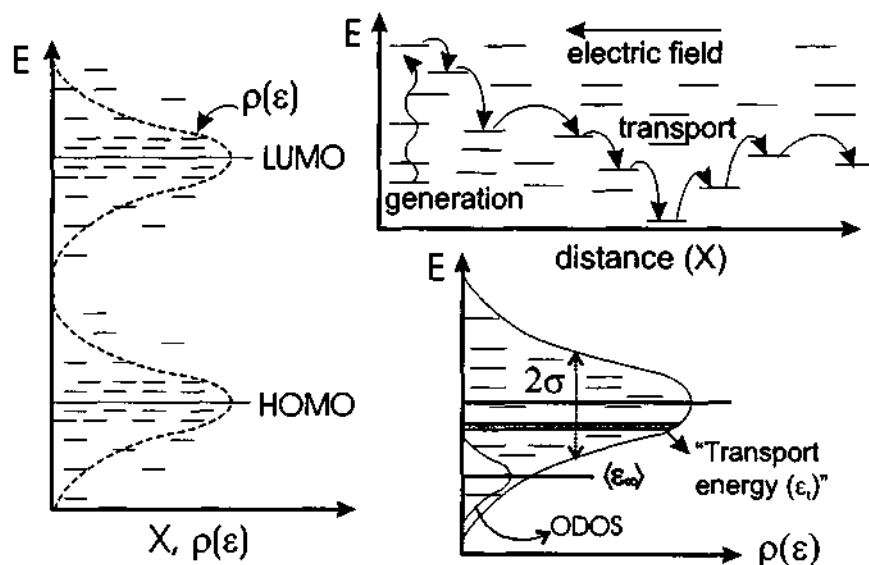


Figure 1.6: Gaussian density of states with the width of the DOS characterized by the disorder parameter σ_E and in the range of 70-150 meV. Qualitatively the energy relaxation of a carrier in Gaussian DOS has been shown. From energy levels above transport energy (ϵ_t) it falls down in energy via hops to spatially neighbouring states with lower energy. After a hop to a site below the transport state, it has to hop upward towards transport energy to take part in transport. ϵ_t plays the role of mobility edge [53]. Figure has been adapted from [54].

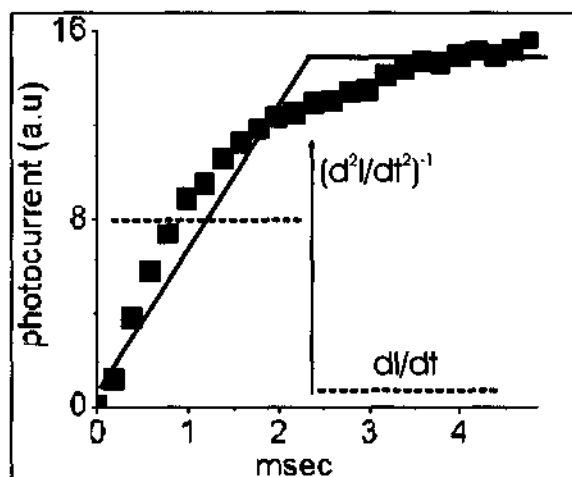


Figure 1.7: The solid line represents an ideal photocurrent turn-on response for a single well-defined mobility value. The data points were obtained from a MEHPPV sample illuminated by a green LED, chopped at a frequency of 100 Hz, applied bias 36V (ITO -ve, Al +ve). Scheme has been adapted from [55].

empty Gaussian density of states (DOS) was simulated using Monte-Carlo algorithm and it was revealed that the carrier tends to relax towards the tail states. The probability density of occupied states (ODOS) is also a Gaussian with its centre displaced by an energy $\sigma^2_{\text{E}}/k_{\text{B}}T$ relative to the center of the DOS and located at $\langle\langle\varepsilon_{\infty}\rangle\rangle = -\sigma^2_{\text{E}}/k_{\text{B}}T$. These carriers require energy to participate in the transport in the so called “transport energy” [56, 57] level located at $-(5/9)\sigma^2_{\text{E}}/k_{\text{B}}T$. This give rise to the following temperature dependence (Equation 1.11):

$$\mu(T) = \mu_0 \exp \left[- \left(\frac{2\sigma_{\text{E}}}{3k_{\text{B}}T} \right)^2 \right] \quad (1.11)$$

Application of electric field will tilt the DOS. This leads to lowering of activation energy for charge transport, hence an increase in mobility. The predicted field and temperature dependence at intermediate field regime was found to be,

$$\mu(T, F) = \mu_0 \exp \left[- \left(\frac{2\sigma_{\text{E}}}{3k_{\text{B}}T} \right)^2 \right] \times \exp[C_0(\sigma_{\text{E}}^2 - \Sigma^2)\sqrt{F}] \quad (1.12)$$

C_0 is a numerical constant. At very high fields the mobility value tends to saturate.

It was demonstrated by Pai [58] that at high electric field F , the mobility of photoinjected holes in poly(N-vinylcarbazole) (PVK), can be described by a Poole-Frenkel like behaviour (Equation 1.13) [59],

$$\mu_h(F) = \mu_0 \exp\left(-\frac{\Delta}{k_{\text{B}}T}\right) \exp(\gamma\sqrt{F}) \quad (1.13)$$

where μ_0 is the temperature independent zero-field mobility, Δ is the activation energy, k_{B} is the Boltzmann’s constant and T is the temperature. The first term on the RHS essentially is an Arrhenius-type behavior. Gill in 1972 [60] proposed

an empirical law for the temperature dependence of the coefficient γ ,

$$\gamma = B \left(\frac{1}{k_B T} - \frac{1}{k_B T_0} \right) \quad (1.14)$$

For PVK, it was found that $B \approx 2.7 \times 10^{-5} \text{ eV}(\text{V/m})^{-1/2}$ and $T_0 \approx 520\text{-}660 \text{ K}$. Gill selected this functional form to account for the fact that $\ln \mu(F, T)$ Vs $(1/T)$ plots intersect at a finite temperature T_0 . Above equation suggests that at $T > T_0$ the field dependence of mobility becomes negative.

The GDM model could satisfactorily reproduce these earlier results. The implications of Equation 1.12 are: (i) A non-Arrhenius type behavior with $\ln 1/T^2$ which seems more realistic considering the fact that Arrhenius-type behavior notoriously overestimates μ_0 values (obtained in the limit $T \rightarrow \infty$ in an Arrhenius plot) $\approx 10 \text{ cm}^2/\text{Vs}$. Equation 1.12 however gives rise to an estimate of $10^{-2}\text{-}10^{-4} \text{ cm}^2/\text{Vs}$. (ii) $\ln \mu \propto \sqrt{F}$, in accordance to the Poole-Frenkel law, albeit for different reasons. The slope of the curve $S = \left(\frac{\partial \ln \mu}{\partial \sqrt{F}} \right) \propto -\frac{1}{T^2}$. Below a certain value of σ_E (or above a certain temperature T), the slope changes sign. Provided the width of the DOS is temperature independent, the characteristic temperature is equivalent to the Gill temperature.

The disorder concept relies on the assumption that the charge carrier transport takes place in a completely empty DOS. However, if the bottom states are already filled then that will change the ODOS. Intuitively, the activation energy of the charge carriers to reach the transport energy level will decrease as a result of a raised quasi-Fermi level due to high carrier density. This case is realized in a field effect transistor where the lower states are filled due to gate bias induced accumulation of charges in the channel region. The strong dependence of carrier mobility on the charge carrier density is the origin of the large difference (almost

3 orders of magnitude) between carrier mobilities reported for FETs and PLEDs [61, 62]. It was demonstrated that hole mobility is constant for carrier densities $< 10^{16} \text{ cm}^{-3}$ and increases with a power law for densities $> 10^{16} \text{ cm}^{-3}$. However there is a counteracting effect induced by extra charges which will cause potential fluctuations and contribute to the energetic disorder parameter. The energetic disorder parameter can be reduced by appropriate processing conditions [63, 64].

The high carrier concentration is therefore an important issue that dictates the charge carrier mobility. It also triggers the second order recombination mechanism in the polymer layer which proceeds at a rate determined by $dn/dt = -\beta n^2$, where n is the concentration of both positive and negative carriers and β is the bulk recombination coefficient. According to Langevin theory [65, 66, 67] for diffusion-controlled recombination mechanism, β has the following form:

$$\beta_L = \frac{e(\mu_e + \mu_h)}{\epsilon_0 \epsilon_r} \quad (1.15)$$

It is to be noted that with increasing mobility the recombination rate also increases. The validity of Langevin theory relies on the assumption that mean free path of the charge carriers are smaller than the coulomb radius $r_c (= e^2/4\pi\epsilon_0\epsilon_r kT)$ over which the attractive coulomb potential of electron-hole pair extends and charge carrier recombination takes place. This theory applies well in case of organic semiconductors where carrier mobilities are less than $1 \text{ cm}^2/\text{Vs}$ and r_c is relatively large [68]. For large charge carrier generation with intense photoexcitation, a situation may also arise when the total photogenerated charge becomes equal to or exceeds the capacitive charge that can be stored in the electrodes. Under this situation the current becomes space charge limited. The occurrence of space-charge limited phenomenon and the onset of bimolecular recombination are interrelated. In the

following section we shall briefly discuss about the signatures and implications of space charge limited behaviour in the TOF current transients.

1.3.3 Space-charge limited TOF current transients

Depending upon the light intensity used in TOF technique, the resultant current transients can be classified into three main categories: (i) $Q_0 \ll CV_0$, where Q_0 is the total photogenerated charge, CV_0 is the capacitor charge stored in the electrode and C is the geometrical capacitance of the sample ($C = A\epsilon\epsilon_0/d$, A is the contact area, d is the sample thickness), (ii) $Q_0 = CV_0$ and (iii) $Q_0 \gg CV_0$, this particular case is called the space charge limited current regime and the transient trace develops a characteristics 'cusp', identified by an initial spike followed by an increasing part which reaches a maximum and then a long decaying tail (Figure 3.13). The maximum point represents the time (t_{cusp}) at which the first transported carriers reach the opposite electrode. This characteristic time is lesser than the conventional non-SCL TOF transient time t_{tr} given by Equation 1.7 ($t_{\text{cusp}} \leq 0.789 \times t_{\text{tr}}$), due to the fact that the region of space charge accumulation (the so called 'charge carrier reservoir') has penetrated into the bulk of the film [69, 70]. The presence of space charge perturbs the external field (for a sandwich configuration ITO/polymer/Au, the +ve bias is applied to ITO, through which the device is illuminated) and almost screens the effect of it inside the reservoir. Only a charge that is approximately equal to CV_0 can drift through the sample and the current becomes space charge limited ($J_{\text{SCL}} = 9/8\epsilon\epsilon_0\mu V_0^2/d^3$) whereas the excess charge remains in the reservoir and recombines away. It has been shown by Juska et. al. that when $\alpha d \gg 1$ and the recombination is "Langevin type bimolecular charge carrier recombination", then the extracted charge (obtained by

integrating the current transient $Q = \int_0^\infty j(t) dt$ saturates to CV_0 in the SCLC TOF regime [71]. In low intensities of illumination when $Q_0 \ll CV_0$, the extracted charge varies linearly with intensity. Hence the saturation behaviour observed in the extracted charge carrier profile as a function of illumination intensity is a direct consequence of Langevin type bimolecular recombination. The bimolecular recombination is the most dominant recombination mechanism that is followed in organic semiconductors. It has been demonstrated for BHJ-solar cell device made from regio-regular P3HT-PCBM blend ($d \sim 0.7 \mu\text{m}$) [72] and for regio-random P3HT polymer samples, the bimolecular recombination coefficient was estimated to be $\beta \sim 4 \times 10^{-12} \text{ cm}^3/\text{s}$ [73].

Recently in a study on spirobifluorene sandwiched between two electrodes along with an additional charge generation layer, occurrence of a ‘cusp’ has been observed at higher temperature [74, 75]. Origin of which can not be attributed to intensity dependent space charge effect. It was argued that the charge carriers generated randomly in a Gaussian DOS tends to relax to the energy state ε_∞ and tries to occupy transport sites distributed around the equilibrium energy ε_∞ in a Gaussian shape. This distribution of occupied sites is called “occupied density of states” (ODOS). This relaxation causes a displacement current. If the relaxation time is shorter than the transit time, the current profile settles to a ‘plateau’, otherwise it becomes dispersive [76]. In presence of a charge generation layer, the charges can be injected near the ε_∞ into the DOS and the current will immediately settle to a ‘plateau’. With increasing temperature, the ODOS shifts towards the center of the DOS and the injection takes place near the tail states of ODOS. These carriers have to move towards the center of the ODOS, as a result of which the current increases and a ‘cusp’ emerges at higher temperatures.

In TOF technique, the film thickness is required to be high ($\sim \mu\text{m}$). As the

thickness is lowered the current trace becomes dispersive. The thickness dependent transport features therefore makes 'mobility' an ill-defined quantity. The concept of a single unique mobility value does not seem to be sufficient. Different transport channels characterized by distinct mobility values contributes to the photocurrent. Hence, mobility values follows a wide spectrum and can be characterized by a 'spatial distribution function' as proposed by Tessler et.al. [55, 77].

1.3.4 Distribution of mobility in thin films

The observation of dispersive nature of current transient in thin samples (typically below 1000 nm) was attributed to the inhomogeneous distribution of carrier properties across the thin film. The thin film can be considered to have many parallel pathways, each having a distinct time independent mobility value. A thin film of polymer sample (~ 300 nm), sandwiched between two contacts (one of them is essentially a blocking contact), when illuminated by a square shaped light pulse (as opposed to a δ -function shaped short duration laser pulse, used in TOF) technique, displays a slowly rising photocurrent transient which eventually saturates to a 'plateau' (Figure 1.7). The varying slope of the rising part was explained as a consequence of spatial distribution of mobility values. The single mobility value would have resulted in a constant slope for the rising part and the second derivative with respect to time would have resulted in a spike at a point where the photocurrent levels off. This characteristic time is inversely proportional to the mobility and can give rise to an unique mobility value. Conversely each parallel pathway, having a distinct mobility value, reaches steady state at different point of time and once it reaches the steady state it stops contributing to the rise in current. This give rise to the monotonically decreasing slope in the rising part of the photocurrent.

To summarize, the low mobility factor ($\sim 10^{-5}$ cm²/Vs) prevailing in organic macromolecular systems dictates the device performance to a great extent. Besides the lack of a well defined mobility in conjugated polymer based devices, the supramolecular packing has huge effect on the carrier transport property. Mobility is highly anisotropic due to the chain packing in the bulk of the polymer active layer. Another challenge in this field is the realization of ambipolar operation because two difficult problems must be solved simultaneously: i) the density of both n and p-type traps should be minimized at organic/dielectric interfaces and ii) an effective injection of both n- and p-type carriers from contacts into the organic semiconductor must be realized. The number of organic materials in which the ambipolar operation has been demonstrated is also limited. Conjugated polymers demonstrate only p-type operation, presumably because of a high density of n-type traps in these devices. In the following section a brief overview of the device aspect has been elucidated.

1.4 Optoelectronic device perspective

In addition to the huge importance of organic polymers in their novel photophysical properties, these materials are interesting for potential technological applications. Despite several limitations, polymer based electronic devices have shown tremendous promise due to its easily tractable chemical and physical properties. Three kinds of devices that has shown huge promise within the premise of plastic based technology has been discussed below. Characterization of devices also enable the extraction of mobility values.

1.4.1 Polymer field effect transistor (PFET)

Field-effect transistor works as a switch depending upon the conductivity of the channel region which can be modulated using gate bias. The architecture of a conventional OFET differs from that of a metal-insulator-semiconductor FET (MIS-FET) structure. In top contact geometry the source and drain electrodes are deposited onto the polymer layer, whereas in the bottom contact geometry polymer is coated onto the pre-coated source and drain electrode. There are two major differences in terms of operation of these devices. (i) OFET is operated in the accumulation mode due to the absence of the inversion layer and (ii) OFETs can be ambipolar unlike inorganic unipolar device. One of the major issue with OFETs is the low field-effect mobility. The highest mobilities are of the order of $1 \text{ cm}^2/\text{Vs}$. Field effect mobilities can be estimated from the slope of transfer characteristics curves. It is to be noted that the mobility obtained from an FET is not a bulk material property and it essentially gives the operational value. μ_{FET} depends on the morphology and property of the organic-dielectric layer.

1.4.2 Organic light emitting diode (OLED)

A notable difference between organic and inorganic LEDs is that, in case of organic LEDs charge carriers are directly injected into the polymer from the metal electrodes, while in inorganic case charge carriers arises from the dopants. In an OLED, the active polymer layer (typically 100 nm thick) is sandwiched between two injecting electrodes, one being a transparent electrode (indium tin oxide, ITO) and the other is a reflective low work function metal cathode (Ca, Al, Ag). The light emission from the device is followed as a result of carrier injection, transport of charge carriers and recombination of the injected electrons and holes. Since all

organic polymers are intrinsically p-type meaning, the hole mobility is higher than the electron mobility, the recombination usually takes place near the cathode. Exciton formation near the cathode gives rise to quenching of exciton by nonradiative recombination. As a consequence, the lifetimes and efficiencies of a single layered OLED is always limited. The theoretical limit to the quantum efficiency of an LED is 25% based on the singlet to triplet ratio. However doping with heavy metal ions like platinum has been useful to push the limit to 63% [78].

In OLEDs with ohmic electrodes the current density-voltage (J-V) characteristics often follow the space-charge behaviour. When the contacts inject charge carriers at a rate which exceeds the transport rate, charge carrier accumulation takes place. This gives rise to the modification of the field inside the device and reduces the electric field near the injecting contact to zero. This condition is met when the excess charges are of the order of the capacitor charge stored in the electrodes. Space-charge limited current is given by Equation 1.16

$$J = \frac{9}{8} \mu \epsilon_0 \epsilon_r \frac{V^2}{L^3} \quad (1.16)$$

This is the famous Mott-Gurney law showing nonlinear JV relation where, L is the device thickness. The measurement of JV -characteristics allows one to find out carrier mobility. But one has to take care that the square root dependence of current on the voltage is not accidental. In order to ensure that the thickness scaling should also be verified. The SCL-formalism has been successfully utilized for conjugated polymers to extract mobility [79, 80].

Another possibility to obtain the mobility from SCL-current is by applying a transient voltage pulse instead of the steady-state conditions (dark injection DI-SCLC) [81]. The measured transient displays a 'cusp', signature of the occurrence of

space-charge, followed by a constant 'plateau' region (corresponding to the constant portion of the voltage pulse). The charge carriers are extracted using the negative part of the pulse [82] (Figure 3.13).

1.4.3 Photodetectors and solar cell

The first solar cell based on inorganic p-n junction was discovered in 1953 by Bell lab scientists Gerald Pearson, Calvin Fuller and Daryl Chapin. The invention of the flexible version of solar cell made from organic molecules is considered to be one of the major leap forward towards renewable energy source. The combination of semiconducting electronic property and mechanical aspects similar to conventional plastics provides a viable alternative for new generation solar cells which has gained a huge attention to meet the global energy demand. The ease of fabrication has made this field technologically viable since the cost of production is very low and the energy payback time in case of organic solar cells is ~ 4 –5 months as compared to inorganic solar cells (where it takes 4–10 years to win back the watts). The low cost processing makes this area technologically attractive where a prototype device of 10% PCE is believed to be the holy-grail.

Significant photoresponse of the semiconducting polymers has been utilized in fabricating high-sensitive photodiodes and high efficiency solar cells. The basic differences between photodetectors and solar cells are (i) in case of photodetectors, charge generation takes place under reverse bias condition, whereas in case of solar cells photoinduced voltage is developed under open circuit condition, (ii) in current voltage characteristics the photodetectors show a minimum current at zero voltage, in solar cell the minimum gets shifted along the voltage axis depending on the photovoltage developed.

621,312 44
P08

JNCASR
5923
LIBRARY

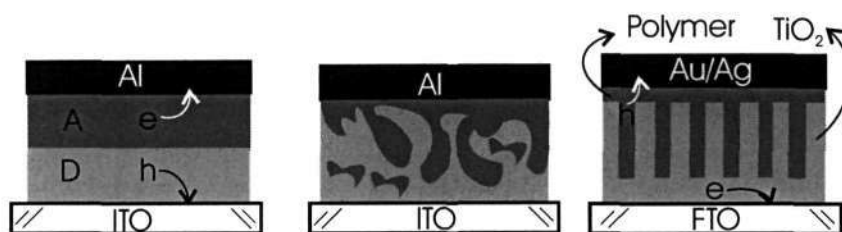


Figure 1.8: Polymer solar cell heterojunctions. The bilayer junction limits the device thickness to ensure that all the excitons reach the heterojunction. Bulk-heterojunction however relaxes this constraint and every generated excitons finds a heterojunction within the diffusion length. An ordered heterojunction is an ideal case where D-A regions are separated by 10 nm (exciton diffusion length).

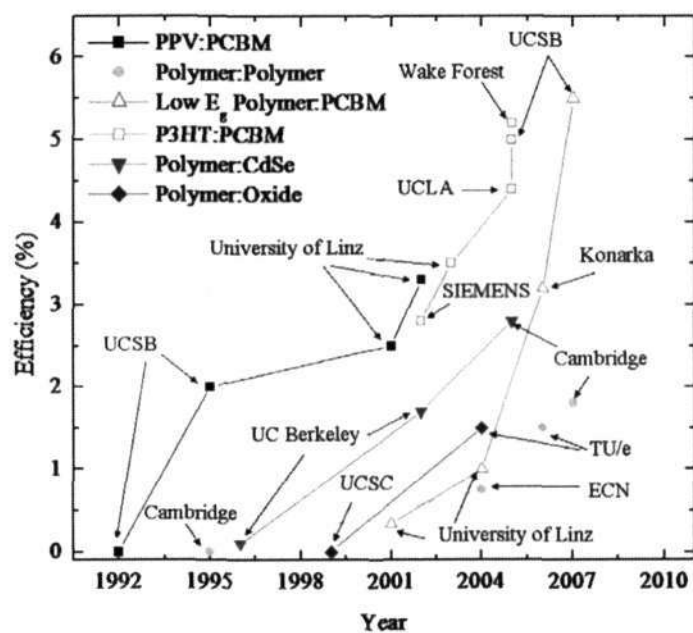


Figure 1.9: Efficiencies of various BHJ devices over time. D-A composites of PPV:PCBM [83, 84, 85], polymer:polymer [86, 87, 88, 89], polymer:CdSe, polymer:oxide [90, 91, 92], low bandgap polymer:PCBM [93, 94] and P3HT:PCBM [95, 96, 97, 98, 99, 100] has been shown. University of California, Santa Barbara (UCSB); University of California, Santa Cruz (UCSC); University of California, Berkeley (UC Berkeley); University of California, Los Angeles (UCLA); Technische Universiteit Eindhoven (TU/e). The figure and the caption and references has been adapted from [101].

Typical device architecture consists of a sandwich configuration between two asymmetrical electrodes with different work functions which enables the dissociation of excitons. But in most of the cases work function difference is not sufficient for charge generation. The device performance was, to some extent improved by introducing a Schottky barrier between the polymer and the metal electrode. However this approach was also proved to be not so efficient. An alternative approach to overcome the limitation has been adopted successfully by introducing heterojunction either in form of a bilayer or intermixed (also called bulk heterojunction) form.

1.4.4 Device architecture and current status

In order to break up an exciton, it is mandatory to incorporate a D-A heterojunction in the device. There are mainly three major device architectures which is followed to introduce the heterojunction: (i) planar heterojunction (ii) bulk heterojunction (iii) ordered heterojunction (Figure 1.8).

In planar heterojunction the device efficiency is limited by the exciton diffusion length. Since the exciton has to find an interface within its diffusion length, the device thickness is very small and the heterojunction is located near the contacts. This makes the light absorption smaller.

The bulk heterojunction approach is the most widely used device architecture. Here the D and A type polymers are intermixed together to form an intimately entangled network of D and A phase (the phase separated domains are formed within few nm distance) so that a bulk photogeneration of exciton can always find an interface within the diffusion length. Using this architecture the solar cell power conversion efficiency has reached 5% and is comparable to the amorphous silicon

efficiency. In BHJ solar cells, active layer bulk morphology plays an important role in the transport process and is controlled by the factors such as solvent properties, distribution of D-A networks [102], drying and annealing conditions [99]. The surface morphology and the structure of the blend-films has recently been studied by controlling the vertical phase segregation of P3HT and PCBM [103]. Different strategies in the improvement of the solar cell include designing low band gap systems to cover the infrared region of the solar spectrum [104], and engineering the active layers for balanced electron/hole transport. Nano-scale patterning [105] and assembling D-A structures have resulted in efficient exciton dissociation [106]. Recently a low band gap polymer, poly[2,6-(4,4-bis-(2-ethylhexyl)-4H-cyclopenta[b;3,4-b']dithiophene)-alt-4,7-(2,1,3-benzothiadiazole)](PCPDTBT) made of alternating electron-rich and electron-deficient units has drawn much attention [107]. Ultrafast electron transfer has been demonstrated between PCPDTBT and PCBM [108] and photovoltaic device has been realized with high power conversion efficiency [109, 110]. Heeger has reported the effect of alkanedithiol treatment on the performance enhancement [111]. This polymer has also found its application in a solution processed tandem solar cell with power conversion efficiency $\sim 6\%$ [112].

Ordered heterojunction is formed by infiltrating polymers into the nanostructured oxide layers. Titania (TiO_2) templates can be made having a mesoporous structure with pore sizes matching the exciton diffusion length can be fabricated by several techniques [113, 114, 115, 116]. The thickness of the nanostructured titania film used to be in the range 300–500 nm that ensures high light absorption. Straight pores are desirable in order to ensure direct pathways for charge carriers. The polymer-infiltrated TiO_x layer is covered with a thin overlayer of polymer in order to avoid any contact between TiO_x and hole collecting electrode (Au). In

these devices where TiO_x is used as an electron transporter and is spin coated onto ITO or fluorine doped SnO_2 (FTO) electrode, a top Au or Ag electrode acts as an anode and bottom ITO acts as a cathode. Since holes get transported through the low mobility polymer, thicker film may give rise to space-charge effect and recombination.

TiO_2 acts as an electron-transporter and hole-blocker due to its extremely low-lying HOMO (4.2 eV). In few device designs it acts as an additional electron transport layer between polymer and FTO. Titanium dioxide is deposited as a smooth TiO_x solgel or rough titanium dioxide nanoparticles (~ 10 nm suspended in water). In either case, the material is spin-cast at ~ 1000 rpm to produce a uniform film 50-100 nm thick, then sintered at 450°C for 30-60 minutes to convert the material to a crystalline anatase phase. The spin coated film from the sol-gel mixture when heated to a lower temperature ($\sim 80^\circ\text{C}$) for 45 mins give rise to a crosslinked amorphous film. Further annealing at 450°C give rise to crystallization.

The high temperature for sintering makes this process unfeasible to use TiO_x as an electron collecting electrode inserted between polymer and the cathode. Recently it has been demonstrated by Heeger et. al. that it can be used as an optical spacer [117] and as a protective interlayer when inserted between polymer and metal cathode [118]. It improves the light absorption efficiency and thereby improve the power conversion efficiency. The transparent TiO_x layer can be used as an electron collecting electrode in tandem solar cells [119] as well. In Figure 1.9 the current status of the organic based PV has been shown.

1.5 Thesis outline

The field of organic/polymer solar cell has undergone tremendous improvement in last decade with the power conversion efficiency reaching 5% limit in single layer devices which is comparable to the amorphous silicon based technology. Understanding the basic underlying charge generation mechanism and transport is a crucial step for achieving higher efficiency in the long run. The contemporary research is focused on intelligent device engineering, understanding basic photophysics and synthesizing lower band gap polymers to capture the infrared photon flux from the sun. The basic device architecture of the solar cell involves blends of polymers and resultant polymer-polymer interfaces which play a crucial role in deciding the device performance. A thorough understanding of the effects of various polymer-polymer interfaces as well as the cathode-polymer interfaces on the performance parameters, is required in the current scenario. The present study addresses few of those aspects.

Novel variable-band gap poly[2-methoxy-5-(2-ethylhexyloxy)-1,4-phenylene vinylene] (MEHPPV) polymers were synthesized to study the energy and charge transfer processes in a ternary blend system. The approach was to make an optimized blend structure where the blue light is captured by a high band gap polymer and is transferred to an efficient interface for charge-transfer reaction to take place. A ternary blend photovoltaic device was fabricated where both type 1 and type 2 interfaces are present. Charge transfer efficiency and energy transfer efficiency of these interfaces and their roles in final photo-generation yield were studied. In the blend the different interfaces were identified and quantified using scanning photocurrent contrast microscopy.

An identifiable direct signature of the interfacial efficiencies manifests them-

selves in current-voltage performance of the device. The performance parameters of MEHPPV based solar cells were addressed based on the bulk and contact limited effects. Bulk material properties affect the device output in two major ways: a strong field dependence of exciton dissociation rate and unbalanced charge carrier mobilities of electrons and holes. In both the cases mobility of the charge carriers play a major role. In order to study the cathode-polymer interface effects on the device, highly efficient P3HT:PCBM blend based solar cells were used as a platform where bulk-limiting effects are minimal. We utilized various forms of cathode layers such as aluminium, calcium, oxidized form of calcium and low melting point alloy to manipulate the cathode-polymer interface and monitor the current-voltage characteristics.

Although the power conversion efficiency (PCE) is solely dictated by the bulk and the contacts, the role of device geometry can not be overlooked. PCE estimations were found to be dependent on the device active area. Scaling of efficiency with different active area was addressed by varying the electrode area and the spot size. The observed photocurrent contribution from the regions outside the assumed dimension of the device can be attributed to the several factors like light scattering in the ITO/polymer interface due to surface roughness and in the glass substrate due the finite thickness. Additional factors like lateral diffusion of photogenerated charge carriers were also identified as a source of the 'extra' current.

The structure of the thesis is as follows: The basic theoretical understandings which forms the background of this thesis is discussed in chapter 2. The materials and their properties, device fabrication and the experimental techniques used in this study has been discussed in chapter 3. Studying charge transfer and energy transfer processes in the polymer blend systems and their application in designing efficient solar cell was the motivation of this thesis work. A novel approach of fab-

ricating a ternary blend device and identifying the roles of different interfaces has been elucidated in chapter 4. Effect of cathode-polymer interface on the device performance has been described in chapter 5. Finally the power conversion efficiency scaling depending upon the device active area has been presented in chapter 6. Apart from qualitative and quantitative studies possible applications and optimum configurations have been postulated in all the above mentioned chapters.

CHAPTER 2

ORGANIC/POLYMER SOLAR CELLS

2.1 Introduction

In order to improve the power conversion efficiency a complete understanding of the photophysical processes are required. Although the operation of an organic solar cell is fundamentally different from that of a silicon based device, the device models for organic solar cells are primarily developed based on the 'drift-diffusion' equations and 'Poisson's equation' which applies well for conventional inorganic devices. The excitonic nature of the primary photogenerated species necessitates the modification of standard 'drift-diffusion' equation to accurately model the organic solar cell device performance. Charge carrier generation due to complete separation of electrons and holes from the neutral exciton dissociation proceeds through an intermediate bound polaron-pair state. The rate equation therefore has to incorporate this phenomenon as well as the recombination factors which are dominant loss mechanisms in these low-mobility solids. In the following sections we shall discuss the physical processes in a BHJ solar cell under illumination and the interesting outcomes of theoretical modeling using standard drift-diffusion equation.

2.2 Device operation and electrical characterization

The simple and most prototypical device structure of organic solar cell device comprises of an active polymer blend layer sandwiched between two electrodes, of

which one is high work-function material (transparent conducting oxide such as ITO) acting as anode and the other is a low work function metal (Calcium, Aluminium) acting as cathode with good light reflection property. Additional layer of poly(3,4-ethylenedioxythiophene)/poly(styrene sulfonate) (PEDOT/PSS) is typically introduced for better ohmic contact with the polymer. The two terminal diode is characterized by sweeping the bias across its terminals and measuring the current. A schematic representation of resultant JV -response is shown in the Figure 2.1.

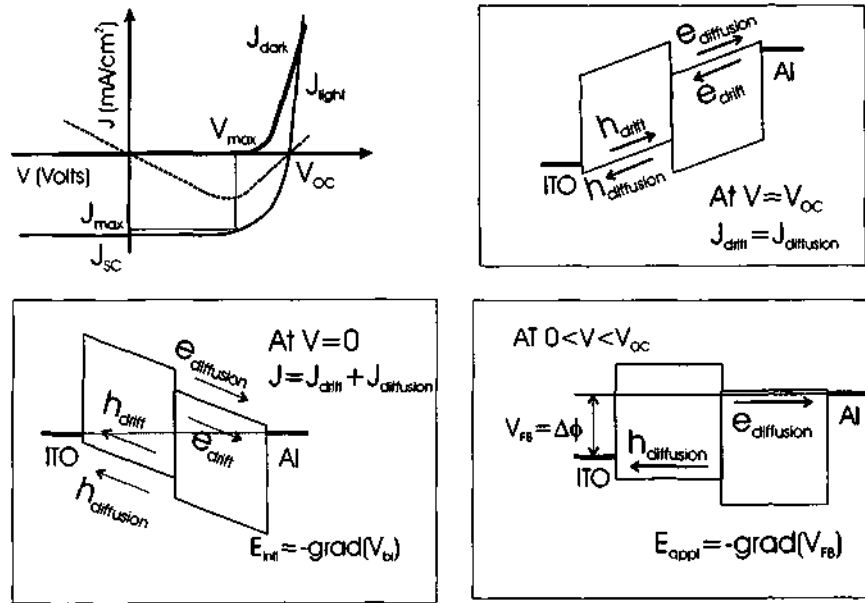


Figure 2.1: The operation of solar cell under external bias. The band diagram is representative of a thin bilayer device

Under dark conditions, the JV -characteristics essentially indicate a diode signature with high rectification property in the reverse bias mode. In the high forward bias conditions (ITO '+ve', Al '-ve') the diode is operating in 'injection' mode and the current in the device is due to the 'drift' of injected charge carriers and can be modeled using standard analysis like Mott-Gurney law ($J \propto V^2/d^3$). Under

illumination, charge carriers are photoinjected in the device and it gives rise to a 'diffusion' current flowing in the opposite direction of the 'drift' current. At a certain positive bias designated as 'open circuit voltage' (V_{OC}), the diffusion current cancels out the drift current giving rise to minimum current through the device. Under zero external voltage diffusion current reaches its maximum and there too exist a drift component of current which arises due to the 'built-in field' present in the device. This field originates from the work function difference of the two electrodes. The drift current is in the same direction to that of the diffusion current and both the components adds up to give rise to 'short-circuit current' (J_{SC}) flowing through the external circuit. However the maximum usable power from the device ($J_{max} \times V_{max}$) is just a fraction of the product $V_{OC} \times J_{SC}$, and this fraction designated as 'Fill Factor' (FF) depends on the shape of the JV -characteristics in the fourth quadrant (Figure 2.1). Finally the power conversion efficiency is calculated using the expression, $\eta_P = FF \times V_{OC} \times J_{SC} / P_{inc}$, where P_{inc} is the incident power density (in mW/cm^2).

2.3 Physical processes in BJH-OSC under zero external field

The photoconversion process goes through the following hierarchy of events: (i) photon absorption (ii) exciton generation, (iii) exciton diffusion towards the interface (iv) exciton dissociation at the interface (v) charge carrier transport and (vi) carrier collection at the electrodes. Each of these events has an associated quantum efficiency number which dictates the final incident photon to collected charge carrier ratio (η_{IPCE}). The 'incident photon to current conversion efficiency (IPCE)'

or 'external quantum efficiency' (EQE) is given by,

$$\eta_{\text{IPCE}} = \eta_{\text{A}}\eta_{\text{ED}}\eta_{\text{CT}}\eta_{\text{CC}} \quad (2.1)$$

where η_{A} is the absorption efficiency of photons within the active material of the solar cell, η_{ED} is the exciton diffusion efficiency, η_{CT} is the charge transfer efficiency and η_{CC} is the charge collection efficiency. We shall discuss the factors that limit these efficiency numbers in more detail.

Conjugated polymers have high absorption coefficient ($\alpha \sim 10^5 \text{ cm}^{-1}$). As a result only a few nanometer thick film can absorb all the light at their peak wavelength of absorption. In order to absorb $\sim 70\%$ of AM1.5 solar photon flux the band gap should be as low as 1.1 eV. Conjugated polymers on the other hand, having a band-gap of 1.9–3 eV can only harvest 30% of the solar photon flux. Lower active-layer thickness further limits the efficiency and only 60% of the incident photons are absorbed at the peak absorption wavelength [120]. Taking the reflection losses into account, the absorption efficiency is given by,

$$\eta_{\text{A}} = (1 - R)(1 - e^{-\alpha d}) \quad (2.2)$$

where d is the thickness of the polymer layer. Absorption of photons gives rise to generation of singlet excitons with binding energy $\gg k_{\text{B}}T$. In order to get dissociated, these excitons have to diffuse to sites, such as donor-acceptor interfaces, where the process is favoured.

The exciton diffusion length L_{D} in conjugated polymer reported in case of various conjugated polymers is in the range 5-20 nm [121]. Because $L_{\text{D}} \ll d$ ($\sim 100 \text{ nm}$) the efficiency of a bilayer device is limited by the number of photons that can be absorbed within the exciton diffusion length from the D/A interface. To

circumvent this problem the bulk heterojunction architecture was adopted where an exciton always finds a dissociation site within its diffusion length. Such an interpenetrating D-A network allows photon absorption improvement simply by increasing the active layer thickness. However, enhancement in photon absorption efficiency in thicker samples is achieved by compromising transport performance parameters. The optimum thickness for photovoltaic cells has been found to be 100–150 nm.

The excitons which reach the heterojunction tends to dissociate and the discussion in Section 1.2.1 is relevant in the present case of bulk-heterojunction devices. Here we shall discuss the transport of dissociated charge carriers. After the charge transfer process, the free electron in the acceptor chain and hole in the donor chain has to get transported towards the electrodes through the percolating pathways where carrier mobility plays an important role. In pristine PCBM, the electron mobility ($\mu_e = 2.0 \times 10^{-3} \text{ cm}^2/\text{Vs}$) [122] was found to be 4000 times higher than the hole mobility in pure MDMO-PPV ($\mu_h = 5.0 \times 10^{-7} \text{ cm}^2/\text{Vs}$) [123]. An important question that arises is whether these mobilities get modified when the materials are blended together. In the blend system, the individual mobilities of electrons and holes, as measured in the pristine polymers, do not retain their character and the notion of an effective mobility seems reasonable. In PPV:PCBM blend [124], an enhancement in hole mobility was found in field-effect transistor measurement. Field effect mobility is always supposed to be higher as compared to the LED or solar cell devices, as it was observed even in case pristine MDMO-PPV [125]. The observed enhancement in the hole mobility is due to the dependence of charge carrier mobility on charge carrier density, which is orders of magnitude higher in transistors than in solar cells (Section 1.3.2). In general, the field-effect mobility can not be compared to the TOF mobility in solar cell devices. Although

from TOF measurements an enhancement of hole mobility was observed depending on the light intensity [126, 127]. Recently Blom et. al. have shown that the hole mobility in MDMOPPV-PCBM (in 1:4 wt ratio) blend is enhanced by more than two orders of magnitude as compared to the pristine polymer case [128]. The single carrier space charge limited current (SCLC) measurements were done on the devices with different PCBM concentration [129] and a gradual enhancement in mobility of electrons with increasing PCBM weight fraction was observed. Surprisingly, the hole mobility was also observed to increase and follow the similar trend. This counterintuitive result is not well understood, and was explained based on the fact that the packing and the film morphology upon addition of PCBM gets favourable for hole transport.

In addition to the morphology of bulk materials and the compositional variation in the blend, electrode modification plays an important role in determining the device efficiency [130, 131]. In classical metal-insulator-metal (MIM) model, open circuit voltage (V_{OC}) is governed by the work function difference of the anode and the cathode. This approximation holds good for the case where the Fermi levels of the metal contacts are within the band gap of the semiconductor and sufficiently far away from the HOMO and LUMO levels. However when the metals form ohmic contacts with the polymer meaning, when the HOMO level of donor matches the work function of anode and LUMO level of acceptor matches the work function of cathode, the situation is different. Charge transfer from metal to the semiconductor takes place in order to align the Fermi levels at the positive and negative electrodes respectively. As a result, the electrode work function becomes pinned to the LUMO/HOMO level of the semiconductor [131]. Consequently V_{OC} becomes dependent on the energy difference between the LUMO of the acceptor and HOMO of the donor. Indeed in BHJ solar cell a linear correlation of the V_{OC}

with the reduction potential of the acceptor has been reported [132]. In contrast only a very weak variation of the V_{OC} (160 meV) has been observed when varying the work function of the negative electrode from 5.1 eV (Au) to 2.9 eV (Ca). Even when the work function of the metal goes below the LUMO level, the Fermi-level of the cathode remains pinned to the LUMO level (3.7 eV for PCBM). This explains why only a little change in V_{OC} is observed when the top metal is changed from Al (4.2 eV) to Ca.

2.4 Theoretical modeling: drift-diffusion equation

Basic understanding of the device operation and the detailed theoretical modeling of the device are the useful tools to explore the performance limiting factors in organic solar cells. Theoretical modeling mostly incorporates the drift-diffusion equation and Poisson's equation to find out the local concentrations of electrons, holes and excitons in these devices and these equations have been used successfully in inorganic ones. However, when applied to organic devices, these same set of equations also satisfactorily reproduce the device characteristics. Since, diffusivity (D) can not be measured directly, one major assumption in the calculation is that the Einstein's relation, relating carrier mobility (μ) to D , also hold good in these disordered systems. Hence D can directly be determined from μ . This assumption is valid only when the carrier transport is classical Gaussian type (i.e. TOF transient displays a rectangular shape). This type of transport is characterized by,

$$\frac{\sigma}{\langle l \rangle} = \frac{\langle (\Delta x^2) \rangle^{1/2}}{\langle x \rangle} = \frac{k_B T}{qF} (2Dt)^{-1/2} \quad (2.3)$$

Equation 2.3 implies the validity of Einstein's law ($qD = \mu k_B T$), where $\mu = (1/F)d\langle x \rangle/dt$ and $D = \frac{1}{2}d\langle (x - \langle x \rangle)^2 \rangle/dt$. In case of time dependent dispersive

transport which is mostly observed in these disordered systems, the carrier motion is described in terms of a power-law variation of waiting-time distribution for carrier hops among localized sites. Under this condition Equation 2.3 no longer holds good.

It has been demonstrated by Richert et. al. [133] that with increasing disorder ($\sigma_E/k_B T$) and field, significant deviation from the Einstein's law can be observed. Transport in a Gaussian DOS give rise to the relaxation of charge carriers at an equilibrium energy ϵ_∞ . The time required to reach this equilibrium is called the relaxation time (t_{rel}) which is a temperature dependent parameter. It has been argued that in the "long time" limit ($t \gg t_{rel}$), the transport begin obeying Gaussian transport and the Einstein's law will hold good in this regime.

Deviation from Einstein's law has also been observed depending upon the carrier concentration. Transport in a Gaussian DOS does not take into account the effect of high charge carrier density. It assumes the transport in a 'diluted' system meaning, the adjacent sites of a charge carrier, available for hopping is vacant. In a non-diluted system (with carrier density $\sim 10^{20} \text{ cm}^{-3}$), the D/μ ratio has been demonstrated to be higher than $k_B T/q$. Tessler et.al. has incorporated the effect of high carrier density where the semiconductor can be considered as degenerate and carrier distribution obey Fermi-Dirac statistics [134, 135, 136]. In solar cell devices where typical incident photon flux $\sim 10^{14} \text{ cm}^{-2}\text{s}^{-1}$ (under AM1.5), the assumption of the validity of Einstein's relation seems to be reasonable. In the following section a detail description of the solar cell device modeling schemes have been discussed.

A numerical model to describe the current voltage characteristic was developed by Barker et. al. [137] for a bilayer device and by Koster et. al. [138] for bulk heterojunction solar cells. Both the models are based on standard set of Poisson equation, current continuity equations and current equations including both drift and diffusion term. The total current density is the sum of drift and the diffusion

component of the current and is given by

$$\begin{aligned} J_n &= -qn\mu_n \frac{\partial \psi}{\partial x} + qD_n \frac{\partial n}{\partial x} \\ J_p &= -qp\mu_p \frac{\partial \psi}{\partial x} - qD_p \frac{\partial p}{\partial x} \end{aligned} \quad (2.4)$$

where $D_{n,p}$ are the carrier diffusion coefficients, which is assumed to obey Einstein relation; $D/\mu = k_B T/q$, ψ is the potential which is related to the electron density $n(x)$ and hole density $p(x)$ by the Poisson's equation,

$$\frac{\partial^2 \psi}{\partial x^2} = \frac{q}{\epsilon} [n(x) - p(x)] \quad (2.5)$$

The current continuity equations are,

$$\begin{aligned} \frac{\partial n}{\partial t} &= \frac{1}{q} \frac{\partial J_n(x)}{\partial x} + U(x) \\ \frac{\partial p}{\partial t} &= -\frac{1}{q} \frac{\partial J_p(x)}{\partial x} + U(x) \end{aligned} \quad (2.6)$$

where $U(x)$ is the net generation rate, i.e., difference between generation of free carriers (G) and recombination of free carriers (R). To obtain a unique solution for the system of equations, the boundary conditions are required to specify the carrier densities and the potential at both the contacts.

The photogeneration of charge carriers goes through the intermediate polaron pair formation which has been discussed in detail in Section 1.2.1. Assuming G is the generation rate of bound polaron pairs, the population or the number X of bound polaron pairs per unit volume changes according to the following rate equation,

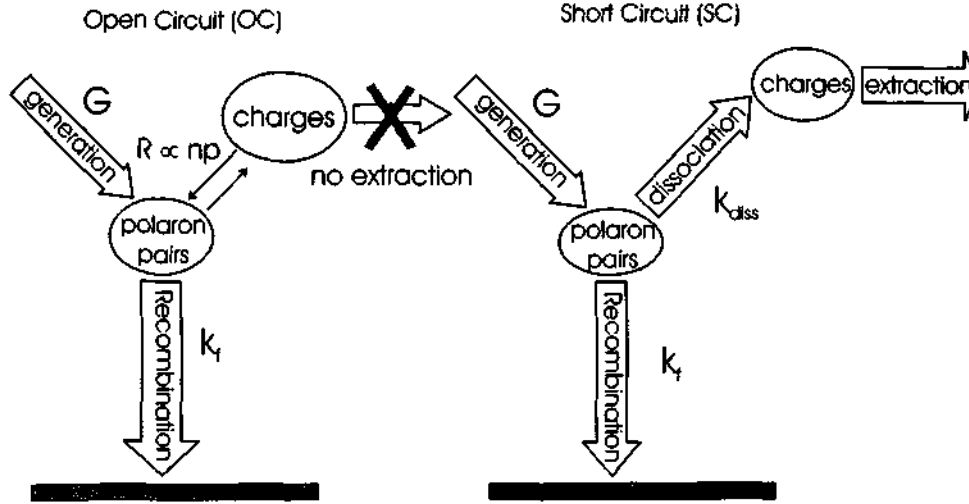


Figure 2.2: The relevant process under open circuit (OC) and short circuit (SC) conditions. If device operation is primarily determined by bimolecular recombination processes at the D–A interface, it is difficult to understand why the short circuit current scales linearly with intensity. At open circuit no carriers are extracted from the device, thus all generated polaron pairs must recombine, giving a population of pairs $X = G\tau_{\text{rec}}$. The third and fourth term of on RHS of equation 2.7 must balance $k_{\text{diss}}(E, T)X = k_{\text{diss}}G\tau_{\text{rec}} = \gamma np$. Assuming $n \propto p$, this gives rise to a free carrier density n at the interface which scales as $G^{0.5}$. Since $G \propto \text{Intensity } (I)$, the dependence is $I^{0.5}$ (consistent with bimolecular recombination dominating the carrier density at the interface). Under short circuit condition carriers can be extracted from the device and the population of free carriers is greatly reduced, so is the bimolecular recombination to form polaron pairs. The yield of free carriers is therefore determined simply by the competition between dissociation and recombination of polaron pairs. Since both the processes are monomolecular, the photocurrent scales linearly with incident intensity. Adapted from reference [139].

$$\frac{dX}{dt} = G - k_f X - k_{\text{diss}} X + R \quad (2.7)$$

where, $k_f = 1/\tau_{\text{rec}}$ is the decay rate to the ground state, k_{diss} is the dissociation rate constant given by Equation 1.3, $R = \beta np$ is the bimolecular recombination rate and β is the Langevin bimolecular recombination coefficient (Equation 1.15). Under steady state,

$$G - k_f X = k_{\text{diss}} X - R \quad (2.8)$$

which is the net number density of generated free carriers. Therefore, the continuity equation for electrons will read

$$\frac{dn}{dt} = \frac{1}{q} \frac{\partial}{\partial x} J_n + k_{\text{diss}} X - R \quad (2.9)$$

using Equation 1.3, $k_{\text{diss}} = [P/(1-P)]k_f$, therefore, Equation 2.8 becomes

$$k_{\text{diss}} X = PG + PR \quad (2.10)$$

and finally the steady-state continuity equation becomes

$$\frac{1}{q} \frac{\partial}{\partial x} J_n = PG - (1 - P)R \quad (2.11)$$

In Equation 2.11, the factor $(1 - P)$ appears essentially because, the recombination of electron and hole in a blend system does not directly give rise to the loss of charge carrier. Instead a bound polaron-pair is formed which can act as a precursor for free carrier generation effectively lowering the recombination constant to $(1 - P)R$. Finally the net generation rate is given by,

$$U = PG - (1 - P)\beta np \quad (2.12)$$

The simulation results reveal the following interesting inferences: (i) Under short circuit condition only 7.0% of free carriers are lost due to bimolecular recombination and the subsequent decay to ground state. These low loss of charge carriers is in agreement with the experimental observation that the short circuit current

varies linearly with intensity (Figure 2.2). The low loss of charge carriers is a consequence of high field strength which facilitates charge carrier extraction and hence reduces the population under short-circuit condition. Due to low population of charge carriers bimolecular recombination strength is weak. Near the contacts the bimolecular recombination rate R is especially low since only one carrier is dominant (a consequence of ohmic contacts). As a result, the net generation rate $U = G - R$ is highest at the contacts. Generally in most of the blend systems, like P3HT:PCBM, the hole mobility is one order of magnitude lower than the electron mobility. Hence, the bulk of the device is dominated by the holes. Near the cathode (about 5 nm away) there still exist considerable hole density, but here electron density also strongly increases. Therefore the rate of bimolecular recombination also increases causing a 'dip' in the net generation rate near the cathode. (ii) Under open circuit condition 97.8% of carriers are lost due to recombination. Since under open-circuit condition, the field in the device is low and there is almost no extraction of charge carriers thus, the bimolecular recombination rate dominates. Only near the contacts, where only one kind of charge carrier density dominates, the net generation is high.

Under steady state condition, the unbalanced electron and hole transport can give rise to interesting phenomenon which limits device performances. Unbalanced transport, leading to accumulation of the slower charge carrier near one of the contacts, manifests a typical square root dependence of photocurrent on the external bias. In the following section this aspect has been elucidated.

2.5 Steady-state space charge effect

The external photocurrent saturates and shows a field independence under higher reverse bias. This behaviour indicates that all the photogenerated free charge carriers are extracted from the device. This happens when the drift-length of the charge carriers ($L_{e,h}^{\text{drift}}$) becomes equal or longer than the sample thickness (d). Under such condition the saturated photocurrent can be approximated as $J_{\text{ph}}^{\text{sat}} = qGd$, assuming no recombination is taking place. However if $L_e^{\text{drift}} < d$ or $L_h^{\text{drift}} < d$ or both are smaller than d then space charge will form and the recombination of charge carriers become significant. The drift length of charge carriers is given by, $L_{e(h)}^{\text{drift}} = \mu_{e(h)}\tau_{e(h)}F$. In case of unbalanced transport where $L_e \neq L_h$ carrier accumulation takes place near one of the electrode. The difference in the drift length can originate from the difference in mobility. It has been shown that in case of MDMO-PPV:PCBM blend where $\mu_h \ll \mu_e$, hole accumulation takes place near anode. As a consequence the electric field in the hole accumulation region (of thickness d_1) increases which facilitates the hole extraction. Similarly the field near cathode will decrease, diminishing the extraction of electrons. Near the hole accumulation region, the field increases and can become equal to the external applied field. In that case the current becomes 'space charge limited' [140] and is given by,

$$J_{\text{ph}} = qG[(\mu\tau)_{\text{slow carrier}}]^{0.5}V^{0.5} \quad (2.13)$$

It is evident that in the hole accumulation region (d_1), there is no counter negative charge carrier to balance the hole-density. However hole-density can not build up indefinitely and there is a fundamental limit to it. As pointed out by Goodman and Rose, the limit is reached when photocurrent generated in this region

$J_{ph} = qGd_1$, is equal to space charge limited current [141],

$$J_{SCL} = \frac{9}{8} \epsilon_0 \epsilon_r \mu_{\text{slow carrier}} \frac{V_1^2}{d_1^3} \quad (2.14)$$

where $\epsilon_0 \epsilon_r$ is the dielectric permittivity. By equating qGd_1 (RHS of Equation 2.13) with Equation 2.14 it follows that the length of the space charge accumulation region d_1 is given by,

$$d_1 = \left(\frac{9}{8} \epsilon_0 \epsilon_r \frac{\mu_{\text{slow carrier}}}{qG} \right)^{1/4} V^{1/2} \quad (2.15)$$

Since $V_1 = V$ under SCL-condition, the maximum electrostatically allowed photocurrent that can be extracted from the device is given by,

$$J_{ph} \leq J_{ph}^{max} = q \left(\frac{9\epsilon_0 \epsilon_r \mu_{\text{slow carrier}}}{8q} \right) G^{3/4} V^{1/2} \quad (2.16)$$

Therefore, for existence of SCLC, (i) The amount of photogenerated charge carriers should be large, meaning large G and a long carrier lifetime $\tau_{e(h)}$ after dissociation of bound e-h pair. (ii) Charge transport has to be strongly unbalanced, meaning the drift length ratio b ($= L_e^{drift}/L_h^{drift}$) should be much greater or less than one ($b \ll 1$ or $b \gg 1$). There can exist one more case where the mobility difference is not so large and $b > 1$ or $b < 1$. This is called ' $\mu\tau$ -limited case'. In this case also, the photocurrent can exhibit a square root behaviour on the voltage. However the distinguishing feature arises from the dependence on G . In ' $\mu\tau$ -limited case' the photocurrent exhibits linear dependence on G (or the intensity of illumination), whereas in 'SCL' case the $J_{ph} \propto G^{3/4}$. Another way to check the presence of a SCLC is to consider the voltage V_{sat} at which J_{ph} switches from square root dependence to saturation regime. In SCL case $V_{sat} \propto G^{0.5}$.

Tessler et. al. performed a detailed numerical analysis over a wider intensity range [142]. It was found that depending on the incident intensity, the space charge effect can take place even for equal electron and hole mobilities. It was further shown for semiconductors where the recombination is Langevin type, the onset of space charge limit and of recombination limit are very similar and practically inseparable. Under low level light intensities the linear relationship between photocurrent and the light intensity is followed and the Langevin recombination is insignificant at low carrier concentrations. As the light intensity is increased, for a fixed applied bias, carrier concentration goes up and it triggers two inter-related mechanisms—space charge limit and consequent recombination (constant carrier accumulation can give rise to charging phenomenon whereas recombination comes as an exit channel for the charge carriers). The photocurrent quantum efficiency (QE = electrons out per photons in) was plotted as a function of intensity over several decades in a semi-log scale (0.01 to 1000 mW/cm²). The point where QE starts to decline from the saturation value was termed as the onset of SCL. Assuming a uniform illumination of the active layer and a low excitation power, such that recombination is negligible, the photocurrent is linearly dependent on intensity [143]

$$J_{ph} = A \cdot P \quad (2.17)$$

where, A is a field dependent constant that relates to generation efficiency and P is the excitation intensity. Taking bimolecular recombination into account, it was shown that the QE can be cast into a simple analytical form,

$$QE \cong 1 - \frac{\left(-1 + \sqrt{1 + \frac{AP}{J_{SCL}} \frac{9}{8}}\right)^2}{\frac{AP}{J_{SCL}} \frac{9}{8}} \quad (2.18)$$

where J_{SCL} is given by Equation 2.14. As P is increased, the QE starts to drop and at certain intensity (P_{R}) it becomes minimum when charge generation current value (AP_{R}) becomes close to slow carrier SCL current (J_{SCL}).

$$A \cdot P = J_{\text{SCL}} \quad (2.19)$$

Using this expression one can deduce the minimum mobility value (for slow carrier) that is required for operating under AM1.5 conditions to achieve a constant current at different voltages. *“The minimum mobility value that is required for a bias close to the open circuit voltage will ensure almost ideal Fill-Factor.”* Using device thickness $d = 100$ nm, $P = 100$ mW/cm² (concentrated at a wavelength 550 nm), $A = 0.5$, $V = V_{\text{bi}} - V_{\text{appl}} = 0.05$ (i.e. near the open circuit voltage regime),

$$\mu_{\text{min}} = \left[0.5 \cdot \frac{0.1}{h\nu} q \right] d^3 / \left[\frac{9}{8} \epsilon \epsilon_0 V^2 \right] \quad (2.20)$$

The mobility value was found to be 10^{-2} cm²V⁻¹s⁻¹. The minimum value scales linearly with intensity. Thus beyond a certain intensity the FF decreases as a function of intensity.

The bimolecular recombination constant as given by Equation 1.15 is valid for pristine material. However in case polymer blends the formula has to be modified according to Braun’s proposal [32],

$$\beta = \frac{q}{\epsilon} \langle \mu_e + \mu_h \rangle \quad (2.21)$$

where ‘ $\langle \rangle$ ’ denotes the spatial average. The idea to use a spatial average value was to compensate for the eventual mobility differences between electrons and holes in the components of the blend. It was further modified by Koster et. al. [144] by

pointing out the fact that the recombination constant will be mainly governed by the slowest charge carrier mobility since, the fast carrier has to 'wait' for the the slow carrier at the interface to recombine.

$$\beta = \frac{q}{\varepsilon} \min(\mu_e, \mu_h) \quad (2.22)$$

In order to discriminate between spatially averaged Langevin and slowest only Langevin a large difference (at least by a factor of 10^3) between electron and hole mobility is required and the difference is reflected in the observed fill-factor. FF is highly sensitive to the recombination strength. The JV -characteristics were numerically computed using set of equations (2.4–2.11). Using $\mu_h = 1 \times 10^{-6} \text{ cm}^2/\text{Vs}$ and $\mu_e = 2 \times 10^{-3} \text{ cm}^2/\text{Vs}$, a spatially averaged Langevin approximation gave rise to a FF of 48 %, while a slowest only Langevin resulted in a FF of 60 %, which is more close to experimentally observed FF of 61 %. The FF in absence of any recombination is ~ 84 %.

2.6 Summary

In summary, the device characteristics is primarily decided by the mobility of charge carriers. In the blend systems where the electron and hole mobility differs by almost two orders of magnitude, space charge effect has been observed to take place. The space charge effect is interrelated with the onset of bimolecular recombination. The higher mobility is desirable for better free carrier generation rate but at the same time this increases the recombination strength as well. Hence there is a trade off between carrier extraction and recombination. It has been shown by Mandoc et. al [145]. that the optimum mobility for best device efficiency is in the range of 10^{-2} - $10 \text{ cm}^2/\text{Vs}$, with higher mobility values having a negative effect on the V_{OC} .

CHAPTER 3

MATERIALS, FABRICATION AND MEASUREMENTS

3.1 Introduction

Polymer solar cell is essentially fabricated in a sandwich type geometry, where the active polymer layer is confined within a high work-function and a low-work function electrodes. The choice of active polymer layer is essentially a blend of two kinds of polymers, one is donor type with high ionization potential and the other one is acceptor type with high electron affinity. A repository of donor and acceptor type polymers and small organic molecules has been compiled over the last couple of decades in this area of research. Among the donor type polymers, P3HT, MEH-PPV, MDMO-PPV are of major importance and the soluble derivative of fullerene (PCBM) is the most widely used acceptor material. The transparent indium tin oxide coated glass substrates in conjunction with a thin layer of PEDOT-PSS coated on top is used as anode and calcium metal coating (with an Aluminium top protective layer) usually serves the purpose of the cathode. A detailed description of the materials selection and the fabrication procedure is discussed in the following sections.

3.2 Materials

In this section the details of several materials used for the study in this thesis is presented and the molecular structures, chemical properties and the synthesis procedures are included.

3.2.1 Poly(3-hexylthiophene)(P3HT)

P3HT belongs to the group of alkyl-substituted thiophene compounds and is usually referred to as poly(3-alkylthiophene) (P3AT). Polythiophene is a leading candidate for optoelectronic applications with sufficient thermal stability ($T_g > 150$ °C). In order to achieve good solubility and processibility, the first synthesis of P3AT was reported a few decades ago [146]. Following this invention there was a considerable progress in synthesis of P3ATs.

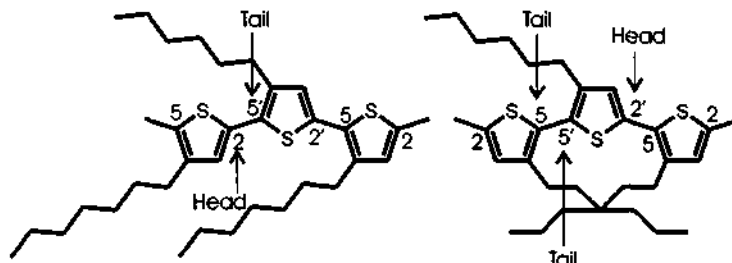


Figure 3.1: Schematic structure of P3HT with head-to-tail coupling and tail-to-tail and head-to-tail coupling

Typically there exist three well known methods for synthesis of P3ATs, namely (i) electrochemical polymerization, (ii) oxidative polymerization of 3-alkylthiophene by oxidants like ferric chloride (FeCl_3) and (iii) polymerization by dehalogenation of 2,5-dihalo-3-alkylthiophene [147]. Depending on the relative position of the alkyl group attached in the two consecutive chains, the polymer chains form head-to-head (HH) or head-to-tail (HT) or tail-to-tail (TT) orientation as shown in the

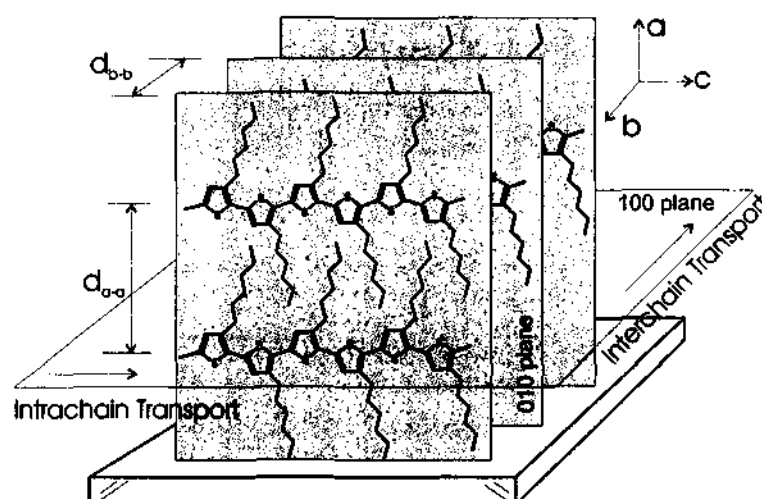


Figure 3.2: Schematic diagram for alignment of P3HT chains on a substrate

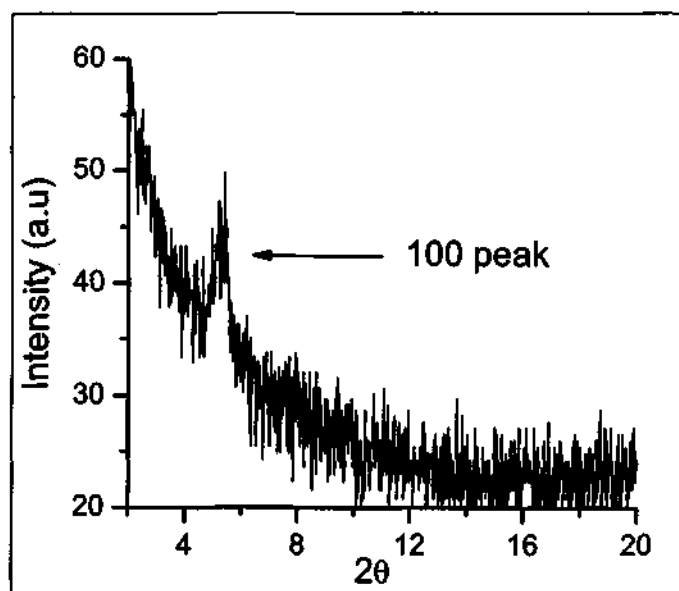


Figure 3.3: Grazing angle X-ray diffraction of oriented P3HT chains. Supramolecular two dimensional structure of P3HT was obtained by spin coating P3HT solution in chloroform (0.7 to 30 mg/mL) on a functionalized substrate. Functionalizing the quartz substrate with hydrophobizing agent like Aminopropyltriethoxysilane (APS) and Hexamethyldisilane (HMDS) was done by leaving the substrates in vacuum for an hour in a 10 mM APS solution prepared in spectroscopic grade toluene. Self-assembly was followed by blow-drying and rinsing and baking at 110 °C for 30 mins in nitrogen environment [148].

Figure 3.1. For HH orientation, the coupling between two consecutive monomer rings occurs through 2- and 2'-positions and similarly HT and TT are through 2, 5' and 5, 5' positions respectively. The appearance of the triad leads to four possible isomerisms namely, HT-HT, TT-HT, HT-HH and TT-HH. The combination of HT-HT can access a low energy planar conformation, leading to high conjugated polymers. On the other hand, appearance of unfavourable HH coupling causes a sterically driven twist of thiophene rings that result in a loss of conjugation, higher band gap with consequent destruction of high conductivity and other undesirable properties. HH and TT interactions give rise to a twisted backbone, in which thiophene rings are not coplanar. This results in a reduction of the intra-molecular π -conjugation along the chain and also a slight increase in the separation between π -conjugated chains when stacked in the solid state, leading to reduced intermolecular π -stacking. According to the degree of orientation, P3HT is divided into two categories. One is the 'regiorandom', where the HH and HT are randomly distributed and the other is referred as 'regioregular' which contains either HH or HT. Most of the polymers are commercially available. In particular, P3HT was obtained from Sigma-Aldrich, USA. The organo zinc reagents formed by reacting Ricke Zinc with 2,5 dihalothiophenes is typically used to synthesize P3HT of this category [149]. These P3HTs offer more than 98.5 % regioregularity.

Solid state crystallographic studies [150, 151] and images obtained by scanning tunneling microscopy (STM) [152] indicate that alkyl-substituted oligothiophenes and polythiophenes have a tendency to aggregate or self-assemble in a stacked interlocking comb-like structure as shown in Figure 3.2. The preferred orientations of the polymer chain along (100) plane due to the lamella layer structure and (010) plane due to $\pi - \pi$ interchain stacking were reported on the basis of X-ray diffraction (XRD) study of P3HT structure [153]. Recent exploration on the orientation

effect of P3HT using synchrotron grazing incidence XRD was also evident from the scattering angles (2θ) 5.3° for (100), 10.7° for (200), 15.9° for (300) and 22.5° for (010) planes respectively [154]. Three dimensional structural order can be represented by axes a, b and c along the lamella layer structure, $\pi-\pi$ interchain stacking and polythiophene chain with repetition distance of 16.81 \AA respectively (Figure 3.2). However the structural orientation of P3HT is very sensitive to degree of regioregularity and the deposition techniques used. A strong regioregularity effect on the ordering has recently been studied [154]. The effect of self-organization on solar cells has been attributed to the enhanced absorption and better charge carrier mobility. Solar cell performance is also dependent on the molecular weight of P3HT. A molecular weight greater than 20,000 was found to yield best results [155].

3.2.2 Poly[2-methoxy-5-(2-ethylhexyloxy)-1,4-phenylene vinylene]

MEHPPV is a widely used polymer in electroluminescence devices. This polymer is a soluble derivative of poly(para-phenylene vinylene)(PPV). It has two side groups attached to phenyl ring at ortho (methoxy) and meta (ethylhexyloxy) positions. Chemical structure of MEHPPV is shown in Figure 3.4. This polymer is expected to be amorphous in nature due to flexible backbone and coiled aggregates formed by long alkoxy sidegroup of chain in the solid state. Determination of the lowest energy structures in this polymer gives the relative values of ground state spacing between the chains and a fairly good idea of the side groups. Because of their planar backbones and long alkoxy side groups, their low-energy configurations in a film have the planes of the backbones parallel to each other.

MEHPPV used for our studies was synthesized at Prof. S. Ramakrishnan's

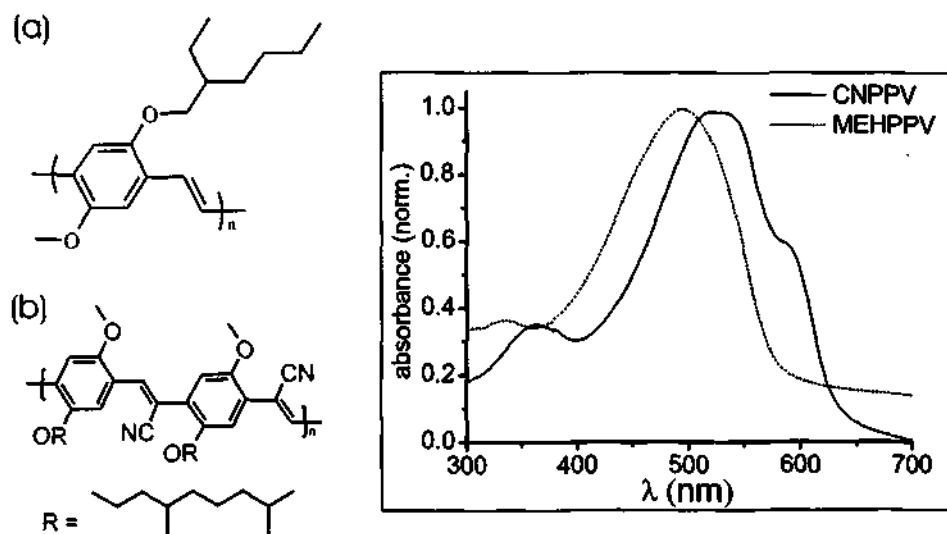


Figure 3.4: (on the left) (a) The chemical structure of fully conjugated poly[2-methoxy-5-(2-ethylhexyloxy)-1,4-phenylene vinylene] (MEHPPV) and (b) cyano-PPV (CNPPV); (on the right) The normalized absorption spectra of MEHPPV and CNPPV. The similar absorption characteristics essentially indicates equal band gap in these two polymers.

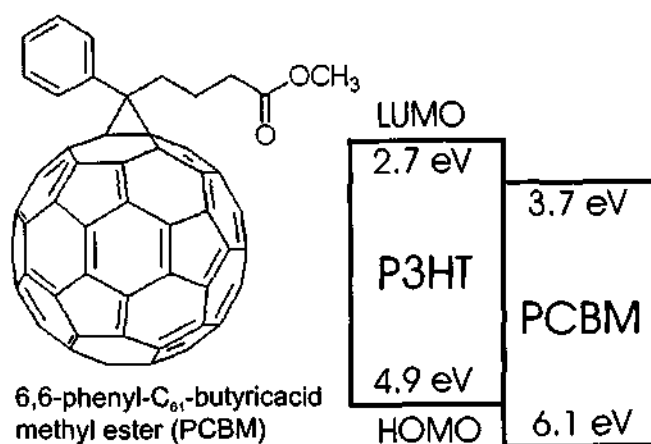


Figure 3.5: Chemical structure of PCBM and the relative positions of the HOMO, LUMO levels of P3HT and PCBM.

laboratory using a novel methodology which provides a control of conjugation and thereby the color of emission [156, 157] in this polymer. This approach relies on the random placement of thermally labile and inert groups on the precursor backbone followed by selective elimination of the labile group. The control of emission color was achieved by varying the mole-fraction of the thermally labile group in the precursor. The labile groups that have been utilized were acetate, xanthate and dithiocarbamate (DTC), while the inert one was a methoxy group. Photovoltaic device was made using 100 % conjugated (high conjugated, HC) and 10 % conjugated (Low conjugated, LC) DTC precursor along with an acceptor polymer cyano-PPV (CNPPV). The weight average molecular weight (M_w) and the polydispersity index (PDI) of the HC precursor were 145500 and 1.95 respectively. Similarly for LC, $M_w = 146400$, PDI = 1.83 and for CNPPV, $M_w = 28400$ and PDI = 4.5 was measured.

3.2.3 [6,6]-phenyl- C_{61} -butyric acid methyl ester

PCBM is the soluble derivative of buckminsterfullerene. Functionalized fullerene has found extensive use mainly in two areas, one is plastic solar cell and the other is optical limiting glasses [158]. The high electronegativity of C_{60} makes this material a wonderful acceptor material for solar cell. The high PL quenching efficiency was observed when C_{60} was added to polythiophene [159] derivative and a PPV derivative [83]. Photophysical and electron spin resonance studies revealed that indeed electron transfer occurred from the excited state of conjugated polymer to C_{60} and, more importantly, the forward electron transfer was in the high femtosecond regime but the back electron transfer was only in the millisecond range. Hence, the charge separated state live long enough to get collected in the electrodes. Indeed

a photodiode was constructed and characterized [160], however, the efficiency was very low. This was attributed to the very low compatibility of C_{60} with MEH-PPV. The problem was solved by functionalizing C_{60} [161, 162].

A poly(3,4-ethylenedioxythiophene)/poly(styrene sulfonate) (PEDOT/PSS) buffer layer was used between ITO and polymer layer in all the solar cell devices. PEDOT/PSS, a commercially available conducting polymer, is a water soluble dispersion of colloidal particles containing PEDOT and PSS-Sodium. PEDOT was found to be an insoluble polymer, yet exhibited some very interesting properties. In addition to very high conductivity PEDOT was found to be almost transparent in its oxidized state. The solubility problem was solved by using a water soluble polyelectrolyte polystyrene sulfonic acid as charge balancing dopant during polymerization to yield PEDOT/PSS [163, 164] (Figure 3.6). The stabilization against coagulation arises from the coulombic repulsion between particles, which results from the surface charge provided by the extra sulfonic acid groups in PSS. The complex is dispersed in water and can be used to make thin films. The conduc-

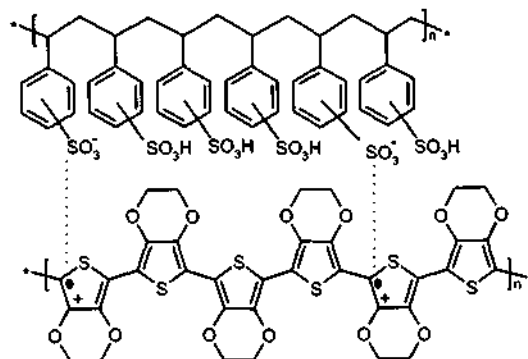


Figure 3.6: Chemical structure of PEDOT/PSS blend (BAYTRON P)

tivity of PEDOT film can be modified by doping and proper annealing conditions [165]. For solar cells PEDOT/PSS is used on top of indium tin oxide (ITO) coated glass substrates. ITO/PEDOT:PSS composite works as a better hole collecting

electrode than the ITO itself. The PEDOT coating improves the work function of ITO and makes it more ohmic. This has been confirmed by electroabsorption spectroscopy [166]. ITO treatment is also an important step for better device performance [167].

3.3 Device fabrication method

P3HT:PCBM blend based devices: Polymer solar cells in sandwich configuration were fabricated using standard protocol, as follows: (i) cleaning of ITO coated glass substrates, (ii) coating of PEDOT-PSS layer on top of it and subsequent annealing (iii) preparation of P3HT-PCBM blend in chlorobenzene (iv) spin coating of P3HT-PCBM blend on PEDOT-PSS coated ITO substrates and subsequent annealing on hot plate for 10-15 mins and finally (iv) controlled and uniform deposition of cathode material. ITO coated glass plates (25 mm × 25 mm) were precleaned with soap-water, ethanolamine, iso-propyl alcohol and acetone (1:1) mixture and finally rinsed thoroughly with distilled water. The substrates were further cleaned using RCA protocol, where the substrates were dipped into a mixture of ammonium hydroxide, hydrogen peroxide and distilled water (1:1:5) and heated at 80 °C for 15 minutes. Finally the substrates were cleaned in distilled water. PEDOT:PSS (Baytron P) was filtered through 40 μm filter and subsequently spin coated onto the cleaned ITO substrates at a spin speed of 1500 rpm to give ~ 80 nm thick film. The substrates were annealed on a hot stage for 30 minutes at 120 °C in ambient environment. P3HT and PCBM mixture (in 1:1 weight ratio) was dissolved in chlorobenzene (20 mg/mL concentration) and the solution was stirred for more than 24 hours inside a nitrogen filled glove box (< 1 ppm O₂ and < 1 ppm H₂O) to obtain a homogeneous mixture. The solution was filtered through 0.22 μm filter

and subsequently spin coated on top of PEDOT:PSS coated ITO substrates (at a spin speed of 1500 rpm for 1 min) inside glove box environment. The polymer coated substrates were annealed on a hot plate (at 80 °C for 10-15 mins). Finally the top metal coating (200 nm Calcium capped with 200 nm Aluminium coating) was done through shadow mask inside a thermal evaporator at a base pressure of 10^{-6} mbar.

MEHPPV:CNPPV blend based devices: Photovoltaic devices based on MEHPPV was prepared from the DTC precursors. Photovoltaic device structures were fabricated with three different blends: (i) low conjugated MEHPPV (LC):CNPPV (in 1:1 weight ratio), (ii) high conjugated MEHPPV (HC):CNPPV (in 1:1 weight ratio) and (iii) ternary blends of HC:LC:CNPPV with varying weight fractions of LC (0, 11, 20, 33, and 66%), while retaining an HC:CNPPV ratio 1:1. For all three devices, the polymer precursor (DTC) and CNPPV mixture was dissolved in chloroform (concentration 10 mg/mL) and spin-coated onto PEDOT/PSS-coated ITO substrates inside a glove-box at 1500 rpm. The thickness of the PEDOT/PSS + polymer layer was measured by using a NT100 optical profiler and was found to be 140 nm. The thickness of the polymer film was found, by measuring the product αd to be ~ 80 nm ($\alpha \sim 10^5$ cm $^{-1}$). After spin-coating with polymer solution, the ITO substrates were annealed on a hotplate at 180 °C for half an hour inside a glove-box. Thermal annealing serves the dual purpose of converting the precursor to polymer and helping the formation of good networks and packing inside the active polymer layer, giving good percolating pathways to their respective electrodes for the charge carriers. Finally, the top aluminum electrode was evaporated under high vacuum condition (base pressure 10^{-6} mbar; 1 bar = 100 kPa).

Patterning active polymer layer by photoacid generator based photolithographic method: Thin film samples were prepared by spin-coating filtered (0.22 μ m filters)

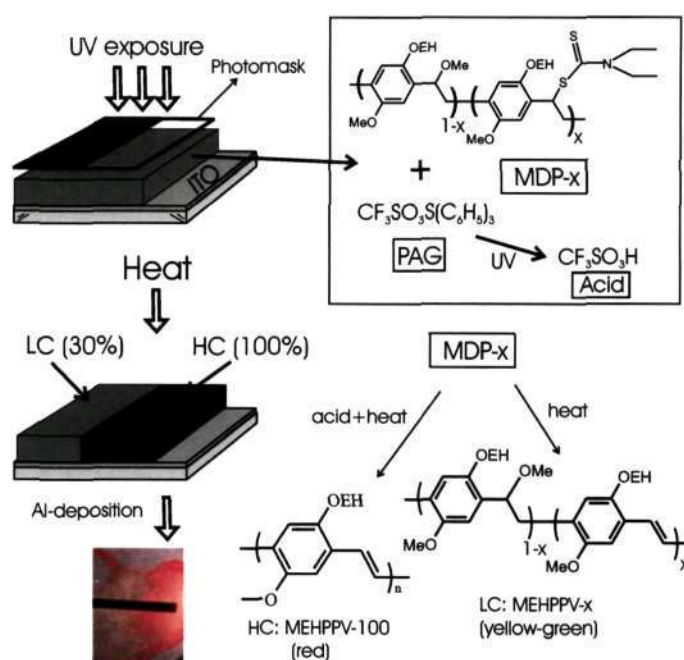


Figure 3.7: Methoxy-diethyl dithiocarbamate (DTC)-precursor polymer (x represents mol% of DTC group containing segment) was mixed with photoacid generator (Triphenylsulfonium triflate) (20:1 weight ratio of MDP-x:PAG) and coated onto ITO substrates. Polymer film was illuminated with UV exposure through a photomask. Under UV exposure PAG generates acid in the exposed regions. Subsequent annealing converts the precursor to completely conjugated form [168]

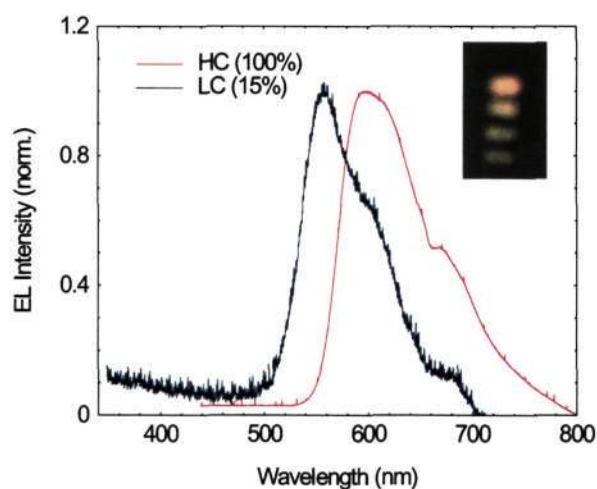


Figure 3.8: Electroluminescence spectra of ITO/polymer/Al devices; inset shows the glowing HC polymer lines (each glowing pixel has an area of $\sim 1.5 \text{ mm}^2$).

polymer solutions (typically 10 mg/mL in THF) onto required substrates. Polymer solution was prepared by co-dissolving 5 wt% of a photoacid generator (PAG), triphenylsulfonium triflate (Aldrich Chemical Co) in the polymer precursor solution (methoxy-diethyl dithiocarbamate) solution for patterning (Figure 3.7). Prior to polymer coating, ITO-coated substrates were cleaned by sonicating in chloroform, then isopropanol and dried in an oven; before spin-coating they were flushed with N₂ gas. A 125 W Hg-vapour lamp was used for UV irradiation of the samples. An Instec Hot stage, model HCS-400, was used for elimination under nitrogen atmosphere at 180 °C for half an hour (Figure 3.7). Onto the patterned polymer film Aluminium electrode was evaporated under high vacuum condition in order to make devices. The electroluminescence spectra was recorded using monochromator attached with a CCD camera (Figure 3.8). The PEDOT/PSS underlayer was avoided in these kinds of devices due to its acidic nature.

3.4 Measurements

All the devices were kept inside a vacuum chamber (~ 1 mbar) with glass window and electrical feed-through. Measurements were repeated sufficient number of times to ensure the reproducibility of the results within the experimental limitations.

3.4.1 Absorption coefficient and photoluminescence (PL) measurement

Absorption spectrum (absorption coefficient (α) as a function of wavelength (λ)), carries primary information about the energy levels of the polymer and provides

an estimation of band gap and sub-band gap levels. Here $\alpha(\lambda)$ of several donor-acceptor polymers were measured using Hitachi U-3400 spectrophotometer and Perkin Elmer spectrophotometer. The absorption coefficient is usually determined from Beer-Lambert's law i.e $P = P_0 \exp(-\alpha d)$, where d is the thickness of the film, P_0 and P are the incident beam intensity and transmitted beam intensity respectively. The relationship between $\alpha(\lambda)$ and the thickness of the film can be written as

$$\alpha(\lambda)d = 2.303 \log(P/P_0) \quad (3.1)$$

One can estimate $\alpha(\lambda)$ when the polymer thickness (from the surface profilometry measurements), P_0 and P are known. Estimation of α near the band-edge is particularly important. Band-edge is determined from the intercept of the tangent at λ corresponding to the derivative $|d\alpha/d\lambda|_{max}$ near the long wavelength region. Band edge position gives an estimate of the band gap of the polymers.

3.4.2 Solar cell JV-characteristics measurements

The solar cell JV-characteristics was measured using one sourcemeter (Keithley 2400) along with a high impedance electrometer (Keithley 6512). All the instruments were interfaced in parallel with the computer by means of General Purpose Interface Bus (GPIB). The data acquisition was done using computer-controlled LabVIEW (version 6.1) programming. The schematic diagram of the set up is shown in the Figure 3.9. The scan was done with sufficient interval between two successive points (typically 1 sec delay). An extremely fast scan (few milisec) also resulted in similar response, indicating the fast response of the device. No hysteresis was observed during a reverse scan. For solar cell IV measurements four-probe

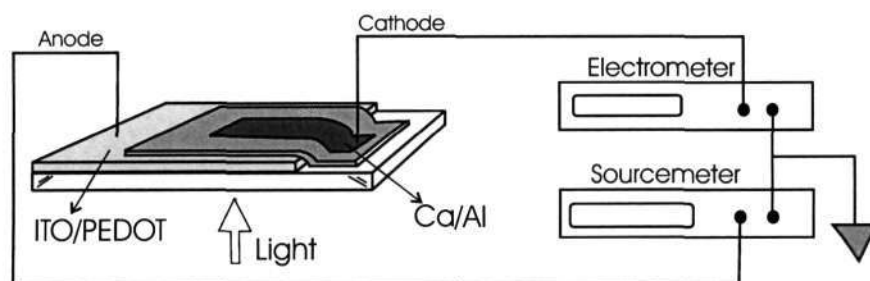


Figure 3.9: Schematic diagram solar cell IV measurement

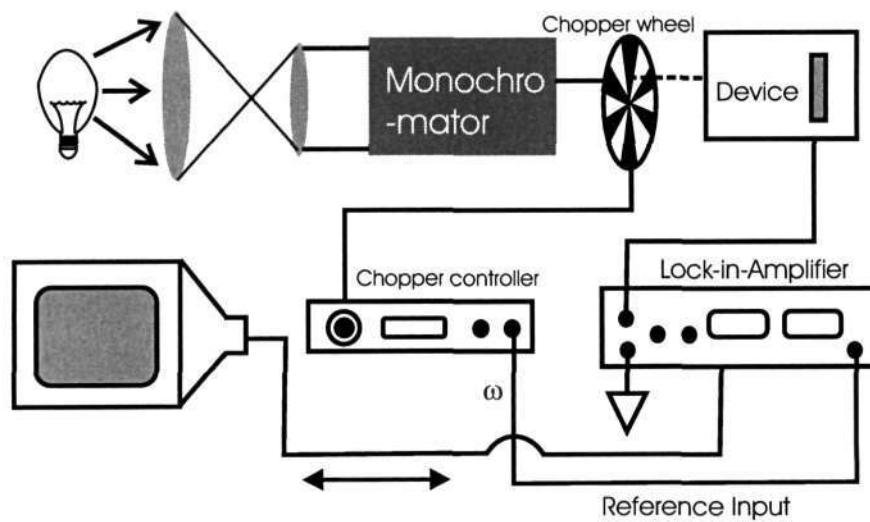


Figure 3.10: Schematic diagram for the incident photon to current conversion efficiency measurement

electrical contact is preferable. The current magnitude observed in the electrometer is always slightly higher than that observed in the sourcemeter.

3.4.3 Intensity modulated photocurrent spectroscopy (IMPS)

Intensity modulated photocurrent spectrum is a powerful tool to measure the photoresponse, field distribution, location of photoinduced charge generation etc. [169]. For solar cells the IMPS measurements yield an important parameter, known as 'Incident Photon to Current conversion Efficiency' (IPCE), sometimes termed as 'External Quantum Efficiency' (EQE). EQE is given by Equation 3.2

$$\text{IPCE}[\%] = \frac{124 \times S(\text{mA/W})}{\lambda(\text{nm})} \quad (3.2)$$

where 'S' is the responsivity of the photodiode which is obtained by normalizing the photocurrent with the power spectrum of the light source. The measurement performed in frequency domain employed a lock-in-amplifier (SR830) which has the advantage of high signal to noise ratio. IMPS involves chopping of illuminated light and measuring current which is synchronized with the chopper frequency. The integration time constant of the lock-in amplifier and so the speed of data acquisition were varied according to the chopping frequency. Tungsten lamp coupled with the monochromator was used to get a wide spectral window for this measurement. The schematic diagram of the experimental set-up is shown in Figure 3.10. IPCE measurement can also be performed by measuring DC current value using electrometer. DC technique however introduces errors due to external stray light, local heating effect and hysteresis of the sample.

For IMPS measurement the calibration of the monochromator is required. Monochromators are not perfect and produce an apparent spectral broadening of the purely

monochromatic wavelength. The δ -function type line-profile gets broaden and the resultant spectrum recorded by a detector is called the instrumental line profile. Any white light source can be considered to be the sum of an infinity of single monochromatic lines at different wavelengths. The resultant spectrum recorded through the monochromator ($F(\lambda)$) from a white light source is thus the convolution of the real spectrum of the source ($B(\lambda)$) and the instrumental line profile (L_P).

$$F = B \times L_P \quad (3.3)$$

The shape of the instrumental line profile is a function of various parameters: the width of the entrance slit, the width of the exit slit, diffraction phenomenon, grating etc. In order to normalize the photocurrent spectrum obtained from the solar cell device, a Si photodetector with known responsivity [$R(\lambda) = S(\lambda)/I(\lambda)A$ (in V/W or A/W); S is the signal output (in V or A), I is the incident energy (in W/cm²), and A is the sensitive area] curve, is placed in front of the monochromator. The device quantum efficiency is thus obtained by normalizing the photocurrent spectrum with the power spectrum of the source recorded by the detector.

3.4.4 Wide-field photocurrent microscopy

In order to carry out photocurrent contrast microscopy on conjugated polymer based thin film devices, a wide field optical microscope was assembled around a NIKON TE-2000 inverted microscope as shown in Figure 3.11. Scanner head (NIS-70) was procured from Nanonics along with scanning software (Nanoview 2.2v) was utilized. This scanner head (dimension 7 cm \times 7 cm \times 0.5 cm, with a circular optical opening) has scanning range 70 μ m in all the three directions with minimum step size of subnanometer. The interface box records data corresponding

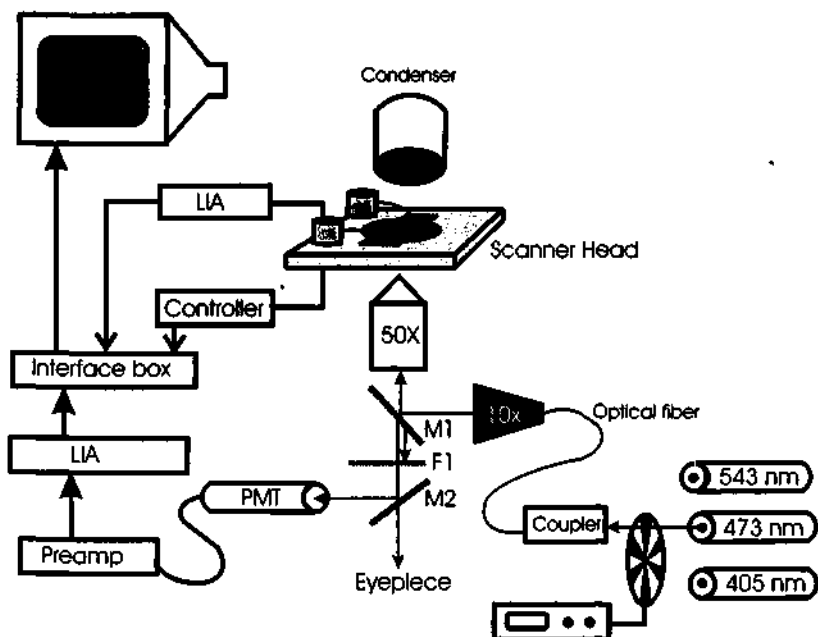


Figure 3.11: Schematic diagram for the wide-field photocurrent microscopy. M1 is the dichroic mirror which reflects excitation wavelength and transmits higher wavelengths. F1 is the PL filter which specifically allows the fluorescence emission.

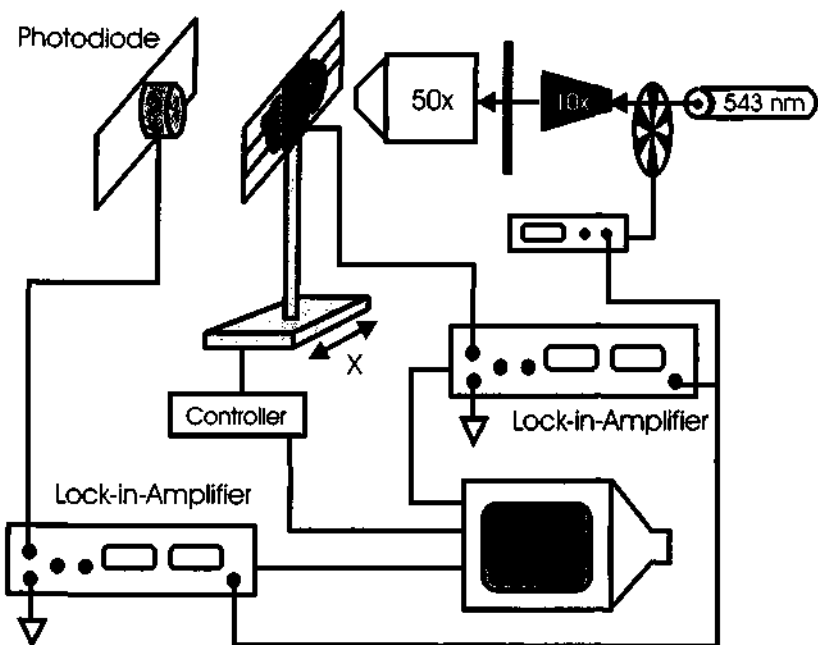


Figure 3.12: Schematic diagram for the one dimensional line scan

to each x-y position simultaneously from 4-channels measuring photocurrent signal, transmission signal, PL signal and morphology. In most of the experiments carried out in our laboratory two channels were used where a simultaneous measurement of photocurrent and reflected excitation light using lock-in technique was done. The reflected light was collected using camera port where a high sensitivity photomultiplier tube (APD, Sensil) was mounted. The detector signal was measured by lock-in technique. A single mode optical fiber (core diameter = 4 μm) was used along with 10X beam expander to illuminate backside of high numerical aperture (NA) microobjective lens (magnification 60X, working distance 150 μm with coverslip correction ring). Mercury lamp port was used for guiding the light coming from optical fiber. Typical excitation wavelengths of 405 nm, 470 nm, 543 nm from three different lasers were used. Dichroic mirrors, coated with specific dielectric layers, and filters were procured from CHROMA for this using this setup in a wide range of scientific problems. The schematic of the set-up has been depicted in Figure 3.11.

3.4.5 Spatially resolved photocurrent scan in 1D

In these measurements, transmission and photocurrent profiles were recorded simultaneously using lock-in technique with a local chopped optical probe (spot diameter $\leq 1 \mu\text{m}$, optical power $\approx 1 \mu\text{W}$, $\lambda = 405 \text{ nm}, 473 \text{ nm}, 543 \text{ nm}, 633 \text{ nm}$). Transmission profiles were recorded using high sensitivity Si photodiode. The polymer device was mounted on a piezo-driver controlled linear translation stage (NEWPORT ESP100, range = 25 mm, minimum step-size = 100 nm). The schematic diagram of the set-up has been depicted in Figure 3.12

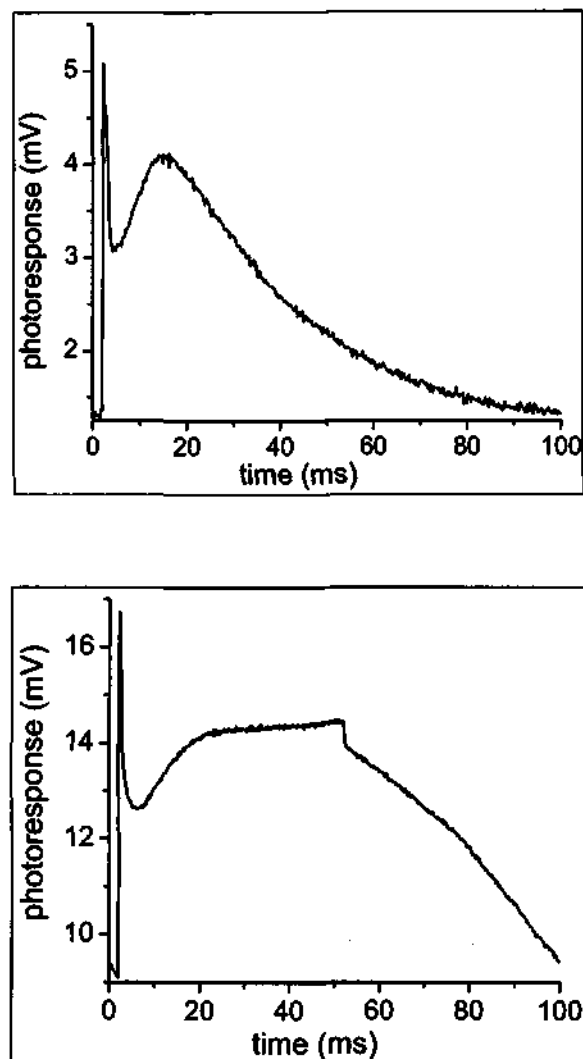


Figure 3.13: TOF signal of a MEHPPV sample sandwiched between amorphous selenium coated ITO and Au, illuminated by a blue LED pulsed at a frequency 10 Hz. Top figure: (a) LED was on for 1 msec. A constant voltage of 54 V was applied across the device (ITO was positively biased). The appearance of the 'cusp' is the signature of SCLC-transient. Bottom figure: (b) TOF signal with the LED (ontime = 50 msec) pulsed at 10 Hz. Voltage applied = 36 V, forward bias. 'Forward Bias' means, +ve bias to the illuminated electrode. A 'cusp' appears due to SCL-effect. The current saturates at the SCL-value due to bimolecular recombination. All the charges in the reservoir gets extracted after the light is switched off. A negative voltage pulse would have been useful to extract charge carriers. However, here charge carriers gets extracted under a constant applied bias. The decaying tail displays a point of inflection which can be identified as carrier extraction time.

3.4.6 Transient photocurrent measurements

Transient measurements provide useful information about the carrier mobility and RC time constant of the device. It is a deterministic tool to evaluate the detector response time and bandwidth. Time-of-flight measurements on thick MEHPPV samples fabricated on an amorphous

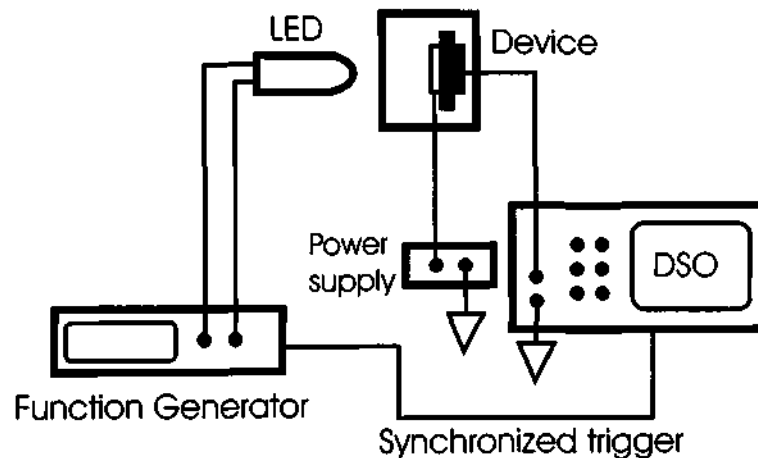


Figure 3.14: Schematic diagram for measuring transient response of photodiode using HP5420 digital storage oscilloscope (DSO) with 1GHz sampling rate and 500 MHz bandwidth.

selenium coated ITO glass substrates was carried out. Amorphous selenium served the purpose of a charge generating layer. A Nd-YAG pulsed laser of pulse-duration 10 ns and repetition rate 80 μ s was used to generate a sheet of charge carriers. In few experiments chopped CW laser excitation (at a particular frequency) was used. The photoexcitation input signal from a chopped light source gave rise to a square shaped photoexcitation as opposed to a δ -function type excitation from the pulsed laser. A LED, also used as an excitation source was pulsed using a function generator. The on-time of the LED was varied by varying the duty-cycle of the trigger pulse driving the LED. All the current traces were measured using a HP5420 oscilloscope which was triggered using synchronized output of the function

generator. Data was collected in real time using sequential single shot mode and was averaged over 10 segments. The coupling (both in AC and DC mode) resistance was 1 M Ω .

3.4.7 Grazing incidence X-ray diffraction (GIXRD) measurement

The ordering and self-assembly of pristine P3HT film oriented on hexamethyldisilane (HMDS)-treated glass substrates was verified using grazing incidence X-ray diffraction (GIXRD) technique. In GIXRD measurement (in plane), a peak at $2\theta \approx 5^\circ$ (θ is the angle of incidence), representing the (100) plane, was observed (Figure 3.3). The GIXRD measurement was conducted in CCMR, Cornell University, USA.

CHAPTER 4

EFFICIENT POLYMER SOLAR CELL BASED ON ENERGY TRANSFER IN GRADED-BANDGAP POLYMERS

4.1 Introduction

Polymer-polymer blend based solar cell has certain advantages over the polymer-fullerene based solar cells. In fullerene based bulk-heterojunction (BHJ) solar cell, only one component is photoactive because of the low absorption of C_{60} in the visible range. The charge transport properties for the two different charges are also unbalanced. Holes undergo a combined diffusion process along the polymer chain, with additional hopping between the chains (mobility for holes, measured by time-of-flight and current-voltage measurements, is $\sim 10^{-7}$ - 10^{-5} $\text{cm}^2\text{V}^{-1}\text{s}^{-1}$ in poly(phenylenevinylene) (PPV)-based devices [170]), and electrons are transported by an exclusive hopping transport process between the small molecules (mobility of electrons is ~ 0.5 $\text{cm}^2\text{V}^{-1}\text{s}^{-1}$ in the single-crystal state of C_{60} [171]). The use of conjugated polymers as both donor and acceptor (DA) components offers a conceptual solution to this problem. Mixing two polymers typically leads to phase separation and creation of microstructured DA junctions. Additionally, with the use of DA polymers of different band gaps, the device can be made sensitive over

a wide spectral range. In this chapter results of BHJ-photovoltaics (PV) based on PPV derivatives are discussed.

A value of power conversion efficiency (η_p) 1% and IPCE (incident-photon-to-current conversion efficiency) of 6% at low light intensities have been reported for a BHJ-PV system fabricated from two different conjugated polymers: poly[2-methoxy-5-(2-ethylhexyloxy)-1,4-phenylene vinylene] (MEHPPV) as the donor, in composite with cyanoPPV (CNPPV) as the acceptor [172]. Recently, much higher IPCEs of 23 [88], 25 [173], and 30% [174] have been measured in PPV-based binary-blend devices with white-light efficiencies of 0.75 [88] and 1.7% [174]. In the present study, the approach was to achieve an optimum morphology for the solar cell where three different polymers would phase segregate naturally and form vertically graded structure with donor type high band-gap polymer at the bottom and acceptor polymer at the top (maximum concentration of the donor polymer at the anode and a small concentration at the cathode end and having more amount of acceptor polymer at the cathode end). This approach has several advantages like better work-function matching of the Aluminum/Calcium electrode with the electron-acceptor (cyano-PPV in this case) LUMO and the proximity of electron-transporting layer with the cathode. This approach also eliminates the presence of any abrupt p-n junction; rather the junction is quite smeared out. The interface between D-A, obtained in this manner is free from any additional barrier [175, 176]. This approach has already been tested from organic field-effect transistor perspective where the polymer-dielectric interface plays crucial role in device performance [177, 178].

Devices were fabricated from three different blends which has been described in detail in Section 3.3. In the ternary blend device vertical phase segregation was not observed instead, the concentration of low-conjugated (LC) MEHPPV was

optimized in the blend.

4.2 Variable band gap donor systems

Band gap of PPV derivatives can be modified by suitably placing conjugation breaks within the polymer chain. The mole fraction of the non-conjugated segment can be controlled which in turn modulates the band gap of the polymer. Blends of MEHPPV with different degrees of conjugation offer the interesting possibility of accessing a wider spectral window. Such segmented MEHPPVs (Figure 4.1) have been synthesized by selective elimination of side groups of a suitable precursor containing two types of eliminable groups, namely, diethyl dithiocarbamate (DTC) and methoxy groups [156]. Selective elimination of DTC groups leaves the methoxy groups unaffected and hence leads to the generation of truncated MEHPPV oligomeric units, of varying conjugation lengths, within each polymer chain. This approach provides a unique ability to control the extent of conjugation length from 100 to 10 %, consequently modulating the band gap to cover a significant portion of the UV-vis spectral window. Blends of two kinds of segmented MEHPPVs, 10 % conjugated (low-conjugated (LC), absorbing the UV-blue part of the spectrum) and 100 % conjugated (high-conjugated (HC), absorbing the green part of the spectrum), can broaden the spectral sensitivity of the photodiode. Considerable energy transfer from the LC polymer to the HC polymer was demonstrated previously by fluorescence studies on these systems [179]. Nondissipative exciton-transfer processes from the segments of low carrier mobility to those of higher mobility followed by their dissociation provide efficient pathways for charge extraction. Thus, light can be harvested and the energy can be channeled to the interface where the charge transfer can take place analogous to the photosynthesis process.

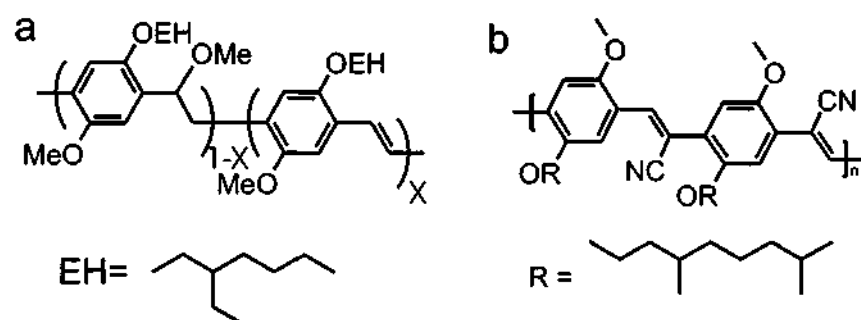


Figure 4.1: Chemical structure of a) segmented MEHPPV containing conjugated segments of varying lengths interrupted by the nonconjugated segments and b) acceptor polymer CNPPV

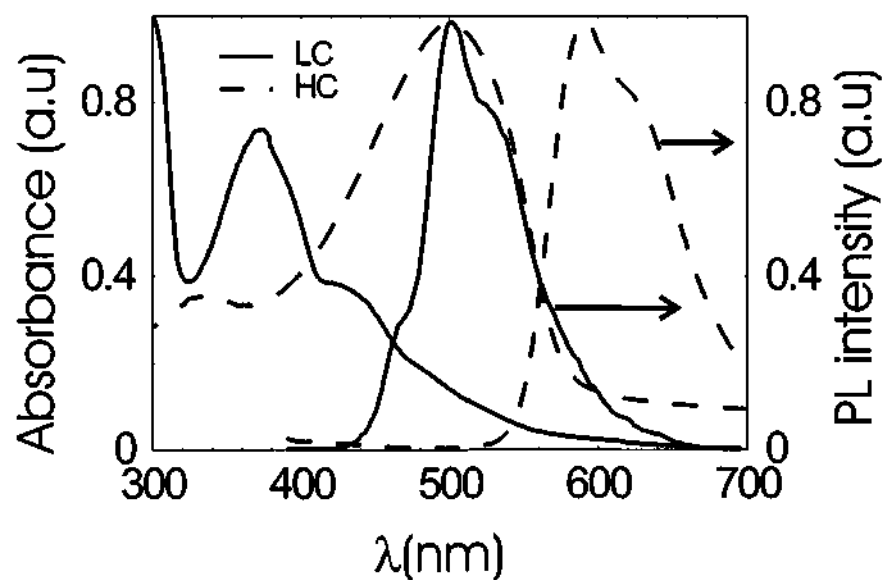


Figure 4.2: Absorption and photoluminescence (PL) spectra of the low conjugated (10 %) and high conjugated (100 %) polymers.

Energy transfer in dye-polymer [180] and polymer-polymer [181] systems have been demonstrated as a viable route to obtain improved performance for laser and PV applications. Voltage-controlled color tuning has recently been achieved in organic light-emitting diodes based on efficient energy transfer from poly(9,9-dioctylfluorene) (PFO) to MEHPPV [26, 182]. We have utilized the broad spectral absorption of segmented MEHPPV copolymer blends to study some of these concepts. BHJ-PV devices using ternary polymer blends consisting of two polymers with different bandgaps (blend of HC-MEHPPV and LC-MEHPPV) as the donor (Figure 4.1a) and CNPPV (Figure 4.1b) as an acceptor reveal improved IPCE.

4.2.1 Absorption and PL spectra of the blend

A spectral overlap between the LC-MEHPPV (high-band gap polymer) emission and the HC-MEHPPV (low-band gap polymer) absorption, which is a primary prerequisite for the energy-transfer process, was clearly observed, as shown in Figure 4.2. The broadening of the absorption spectrum of the blend film consisting of two kinds of polymer (LC and HC) was also observed, as shown in Figure 4.3. The absorption spectrum was tuned by varying the relative concentrations of the LC and HC components, where the characteristic peaks of the individual polymer constituents varied depending on the concentration. The absorption spectrum of HC-LC blends was approximately the weighed sum of the HC and LC spectra, suggesting that the ground-state interaction between the chromophores in the mixture is minimal and the lowest $\pi - \pi^*$ transitions of individual chromophores are roughly intact upon blending. The efficient exciton transfer was evident in the fluorescence spectra of the blends (Figure 4.4), in which an increase of photoluminescence (PL) from HC-MEHPPV at the expense of a complete annulling of PL

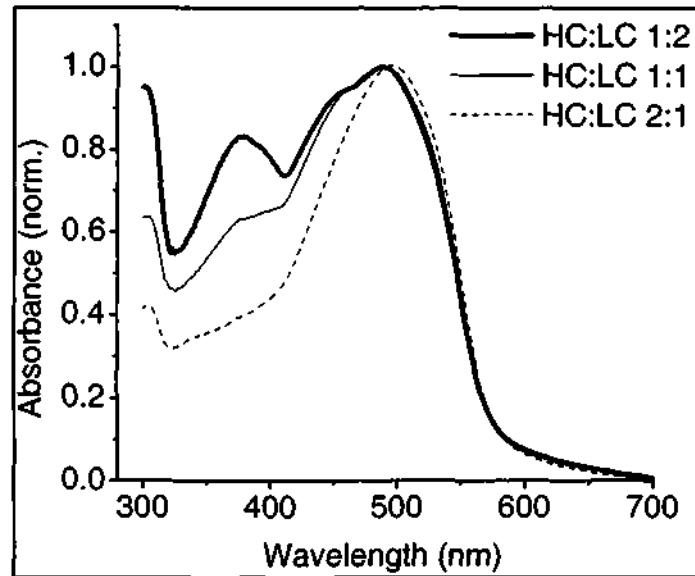


Figure 4.3: Normalized absorption spectrum of polymer blend films

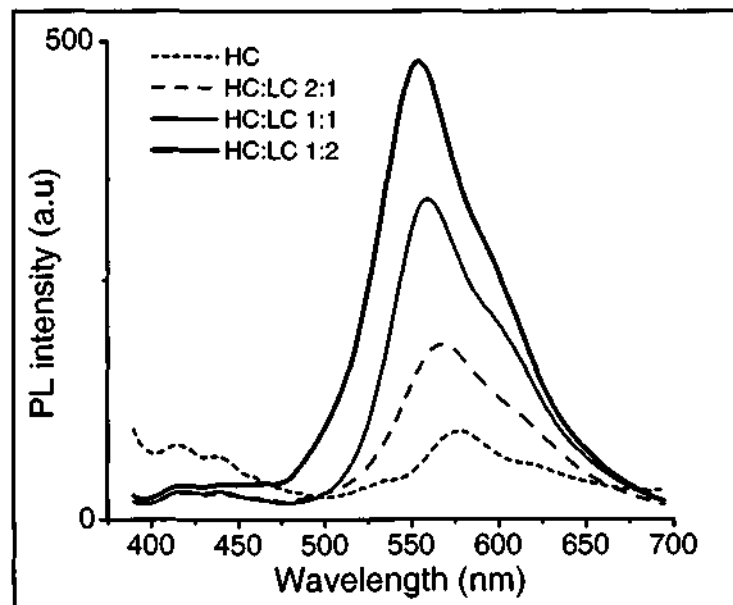


Figure 4.4: Photoluminescence spectra of the polymer blend films in different weight ratio using 370 nm excitation. In the blend the PL resembles the feature of HC polymer and the PL of LC phase gets completely quenched.

from LC-MEHPPV was observed. The quantum yield of the pristine LC phase in solution form is much higher ($\sim 85\%$) than that of the pristine HC in solution form ($\sim 15\%$) [156]. A similar trend was observed in solid-state polymer films. In the blend of the two polymers the PL of the LC phase was completely quenched and the PL of the HC phase was enhanced. The shape of the PL spectrum of the blend was similar to that of HC-MEHPPV with the expected vibronic fine structures. This behavior suggests that an efficient energy transfer takes place from the LC phase to the HC phase following a Förster-type mechanism, implying the formation of domains of nanometer dimensions (3-10 nm, the characteristic length scale for Förster energy transfer). The effect of phase segregation on the energy-transfer efficiency in segmented MEHPPVs has recently been studied [179].

Upon introducing an acceptor polymer, CNPPV, to form a D-A composite blend, the PL of pristine HC-MEHPPV and LC-MEHPPV was quenched by more than two orders of magnitude. However, the quenching efficiency in LCMEHPPV:CNPPV system was larger than in HC-MEHPPV:CNPPV system (Figure 4.5) in solution. The PL-quenching efficiency can be lower in case of films depending upon the phase segregation. The active layer films obtained from these components were uniform in thickness, with a RMS surface roughness of ~ 1 nm, as indicated by atomic force microscopy (AFM) topography profiles.

4.3 Intensity modulated photocurrent spectra

The photovoltaic properties of these D-A composite films were investigated. The results are summarized based on the studies of devices with three different active-layer compositions: (i) HC-MEHPPV and CNPPV blend device, (HC/CNPPV, 1:1 weight ratio); (ii) LC-MEHPPV and CNPPV blend device (LC/CNPPV, 1:1

weight ratio); and (iii) HC-MEHPPV, LC-MEHPPV, and CNPPV based ternary-blend devices containing varying weight fractions of LC-MEHPPV (0, 11, 20, 33, and 66 %), while retaining an HC-MEHPPV/CNPPV ratio of 1:1. Several devices (5–10) of each composition were tested to verify the reproducibility of the results. The spectral variation of the IPCEs of typical devices is displayed in Figure 4.6 for short-circuit mode of operation. The lowest IPCE was observed in the LC:CNPPV device, whereas the ternary-blend device exhibited the highest IPCE. The photocurrent and the IPCE of the LC:CNPPV device, in the 450 to 650 nm range, is due to CNPPV absorption alone. The IPCE spectrum of the LC:CNPPV device showed a small peak at 370 nm, which may be attributed to the absorption of LC-MEHPPV and CNPPV. The poor photocurrent and low efficiency ($\sim 3\%$ at 530 nm) are mainly due to poor hole-mobility along the LC chain. The charge-transfer (CT) states with electrons in the acceptor chain and holes in the donor chain are bound by weak coulomb interactions between them; therefore, the bichromophore recombination (either radiative or nonradiative) may possibly limit the IPCE of LC:CNPPV device. Contrastingly, the IPCE of the HC:CNPPV device was quite high ($\sim 10\%$ at 530 nm). It should be noted that the absorption coefficients, $\alpha(\lambda)$, of HC-MEHPPV and CNPPV (Figure 4.2) are quite similar and hence the contribution from different processes cannot be distinguished. IPCE(λ) across the entire spectral region arises from constituent HC-MEHPPV and CNPPV responses, distinct from the efficient processes occurring at their interfaces. In the ternary-blend devices the weight fraction of the LC phase was varied while retaining a constant 1:1 ratio of HC-MEHPPV and CNPPV. The IPCE of the device exhibited a maximum value when the weight fraction of the LC phase was $\sim 20\%$ (Figure 4.6(b)), at which the actual ratio of the three components was 2:1:2 (HC-MEHPPV:LCMEHPPV:CNPPV). At this optimized composition,

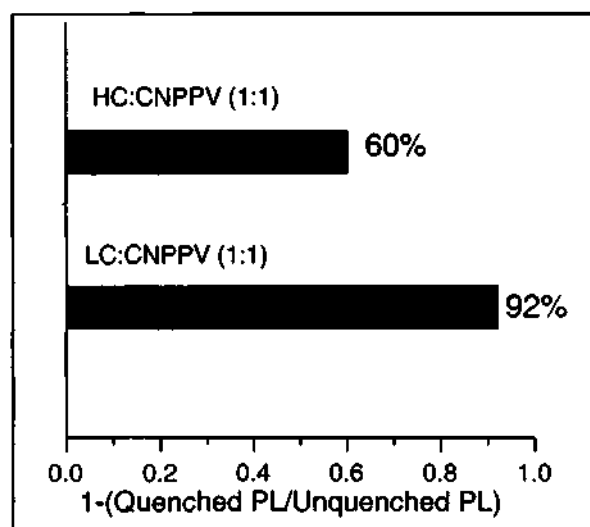


Figure 4.5: Upon blending with CNPPV the PL of LC polymer gets quenched by 92%

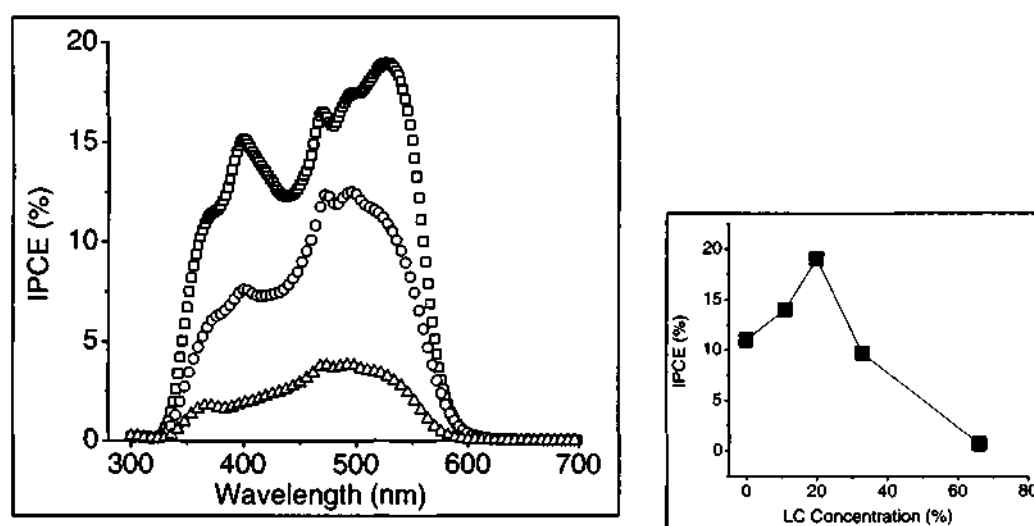


Figure 4.6: The short circuit action spectra of the binary and ternary blend devices. The variation of photocurrent (IPCE at 530 nm) with different LC ratios is shown in the adjacent figure. It was observed that the overall photoconversion efficiency is at maximum for a particular concentration of LC ($\sim 20\%$). The low IPCE ($\sim 3\%$) of LC:CNPPV blend (in spite of high PL quenching efficiency of 92%) indicates most of the charge-separated polaron pairs recombine geminately.

an enhanced IPCE ($\sim 19\%$) was achieved. This optimal composition of the LC phase reflects the balance of effective charge carrier separation and the mobility of the charge carriers, bearing in mind the poor hole mobility in the LC phase. The enhanced efficiency does not merely appear to arise from the linear combination of the IPCE of the homopolymer-CNPPV junctions. It is to be noted that three sets of interfaces are present in case of ternary-blend device, of which the HC/LC interface is favorable for energy transfer and the HC/CNPPV interface is favorable for efficient charge transfer along with the low-yielding LC/CNPPV interface. A simple physical picture can explain the observed improvement of the quantum efficiency in the blue spectral region. The excitons created at the LC phase are transferred to the HC phase followed by charge transfer at HC/CNPPV interface, which is a more efficient interface for CT, as depicted schematically in Figure 4.7. A similar mechanism was proposed by Inganäs [181] in bilayer devices containing blends of PPV and polythiophene derivatives with C_{60} as the electron-accepting layer.

A simplistic quantitative estimate of the quantum efficiency can be obtained by considering the $\alpha(\lambda)$ and the mobility-lifetime product ($\mu\tau$) of the constituent polymers. External quantum efficiency or IPCE can be expressed in terms of photon absorption efficiency (η_A), exciton-diffusion efficiency (η_{ED}), charge-transfer efficiency (η_{CT}), and the charge-collection efficiency (η_{CC}) and is given by Equation 3.2. The built-in field (V_{bi}), provided by the band offset between the aluminum electrode and the polymer ($\sim 10^5$ V/cm), facilitates the charge-carrier extraction process and limits the charge-carrier recombination. The average distance over which holes travel before recombination is $\mu\tau_r V_{bi}$ (where μ is the hole-carrier mobility and τ_r is the recombination lifetime of the holes). Hence, the exciton dissociation efficiency (η_D) (the fraction of electron-hole pairs that contribute successfully

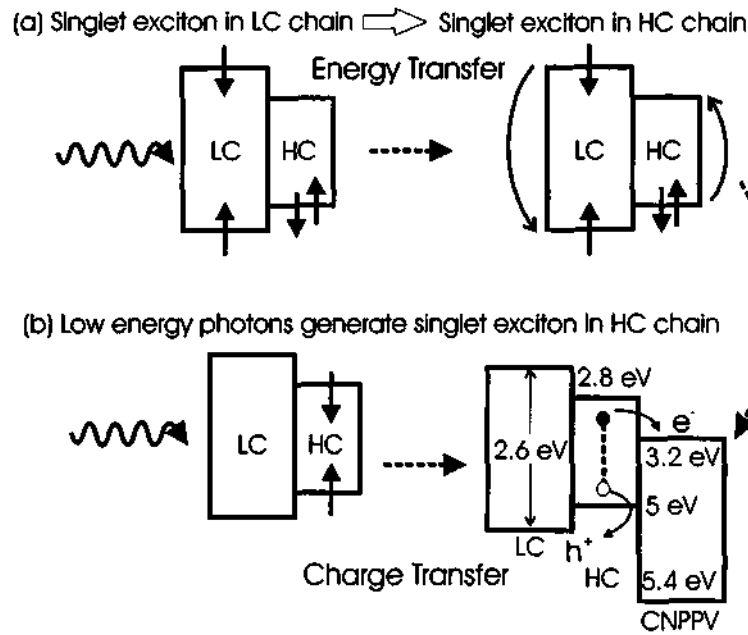


Figure 4.7: The absorption of high-energy light photons creates excitons on the LC chain and HC chain. The exciton on the LC chain can subsequently be transferred to the HC chain and be dissociated at the HC/CNPPV interface; the excitons on the HC chain can also lead to the same charge-transfer process.

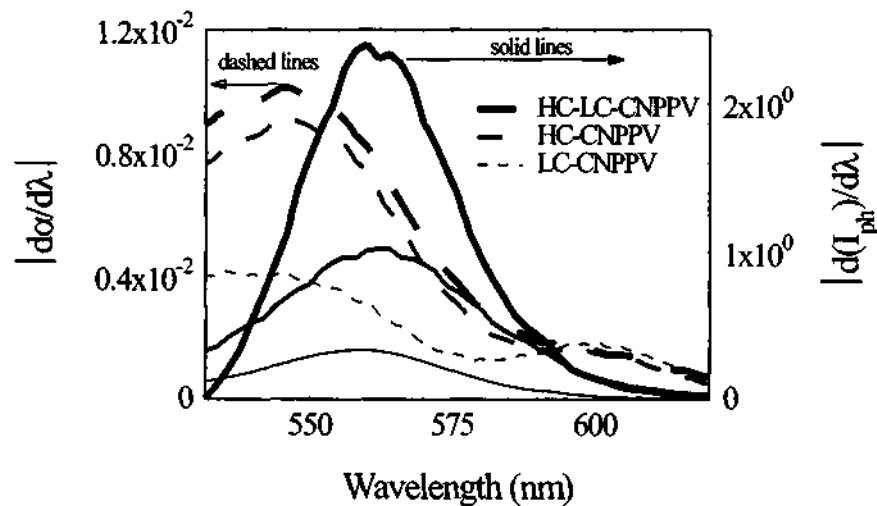


Figure 4.8: The derivative of the absorption coefficient (α) and photocurrent (I_{ph}). The derivative of the I_{ph} for the ternary blend photodiode has the lowest line width, indicating the steepest rise in the current near the band edge.

to the current) can be expressed as (Equation 4.1)

$$\eta_D = \eta_{ED}\eta_{CT}\eta_{CC} = \eta_{\max}[1 - \exp(-\mu\tau_r V_{bi}/d)] \quad (4.1)$$

where η_{\max} is the maximum dissociation efficiency, and d is the thickness of the active-polymer layer. Incorporating these effects in the η_{IPCE} and neglecting the reflection losses at the air/substrate interface we get (Equation 4.2) [183]

$$\eta_{IPCE}(\lambda) \approx \eta_{\max}\{1 - \exp[-\mu\tau_r V_{bi}/d]\} \times (1 - e^{-\alpha(\lambda)d}) \quad (4.2)$$

At 530 nm, the small value of η_A of LC:CNPPV is due to the low αd value, but at 400 nm the limiting factor is the mobility of holes along the LC polymer chain. The mobility of holes in LC polymer is much lower (1D mobility of the positive charges along the polymer chain ($\mu_h \ll 0.005 \text{ cm}^2\text{V}^{-1} \text{ s}^{-1}$) than in the HC polymer ($\mu_h \approx 0.42 \text{ cm}^2\text{V}^{-1} \text{ s}^{-1}$) [184], so the mobility-lifetime product for the LC phase is small ($\mu\tau_f \sim 5 \times 10^{-13} \text{ cm}^2\text{V}^{-1} \text{ s}^{-1}$; τ_f is the lifetime of the fast transport and is approximately 100 ps in the case of PPV [185]), which explains the low quantum efficiency. In the case of the HC:CNPPV device, Equation 4.2 gives an estimate of $\eta_{IPCE} \sim 6\%$ at 530 nm (using $\alpha d \approx 0.15$ at 530 nm, $\mu\tau_f \sim 4 \times 10^{-11} \text{ cm}^2\text{V}^{-1}\text{s}^{-1}$ and $\eta_{\max} \sim 1$), which is comparable to the experimentally observed value ($\sim 10\%$).

In the ternary-blend devices, the enhancement in the blue region is due to energy transfer from shorter oligomeric segments to the longer oligomeric segments [186]. In the LC phase (which contains only 10 % conjugated segments), the fractional population of shorter oligomers is higher [187]. Selective excitation of the shorter oligomers is followed by significant transfer of energy to the neighboring longer oligomers, either in the same chain or to a neighboring HC chain. In the ternary blend, the LC phase always transfers energy to the more highly conjugated

chromophores, which in turn gives rise to an additional enhancement of η_{\max} in the blue part of the spectrum.

The increase in IPCE in the blue region (~ 400 nm), is attributed to energy transfer from chromophores in the LC domain to those in the HC domains and subsequent charge transfer across the HC/CNPPV interface. The feature suggests that the efficiency of energy transfer from LC to HC depends on λ . As λ increases a relatively smaller number of longer-conjugation-length excited chromophores are created in the LC domains, and these find it difficult to transfer the energy to chromophores in the HC domains because of the expected lower proximity. Hence, only directly excited chromophores in the HC domains contribute to the IPCE as the wavelength increases. This causes a slight decrease before the second increase because of increasing direct absorption by the HC domain. There is a small feature at 470 nm, which is consistently present in all the three kinds of devices (LC:CNPPV, HC:CNPPV, and HC:LC:CNPPV). This feature does not arise from the active medium but is an artifact which appears when there is an underlying layer of PEDOT:PSS present. Response from the (low-efficiency) devices in absence of the PEDOT:PSS buffer layer did not indicate this feature. Energy funneling to the HC sites from a broad range of absorbing chromophores in MEHPPV is a well-established hypothesis [188]. In addition, the presence of the HC phase provides better transport pathways for holes.

The transport factor appears to be enhanced in the ternary blend systems compared to the binary systems. This is indicated by studying the spectral profile near the band-edge region. The band edge of the polymers, as determined from the intercept of the tangent at λ corresponding to the derivative $|d\alpha/d\lambda|_{\max}$, was found to be ~ 590 nm for all the three devices. The essential features observed (Figure 4.8) are: (i) the steepest increase in photocurrent (I_{ph}) in the case of the

ternary blend ($|dI_{ph}/d\lambda|$ is at a maximum near the band edge); and (ii) the ratio of $|dI_{ph}/d\lambda|$ for HC:CNPPV and ternary-blend devices is three orders of magnitude higher than their $|d\alpha/d\lambda|$ ratio. The significant rise in current near the onset of absorption can be attributed to the enhanced effective mobility in the ternary blend because of better interconnecting pathways to the electrodes. The LC phase is typically inactive near the band edge of the polymer. Hence, it acts as an inert host matrix for the HC:CNPPV composite near the red part of the spectrum. Dilution of the conjugated polymer by the inert host matrix appears to facilitate the charge transport by increasing the HC/CNPPV interface and possibly providing greater interconnecting networks. Furthermore, inclusion of an inert matrix modulates the overall dielectric constant ϵ_r of the system [189]. The dielectric constant controls the Coulomb radius ($r_c = e^2/4\pi\epsilon_0\epsilon_r k_B T$, where ϵ_0 is the permittivity of a vacuum, k_B is the Boltzmann constant, and T is temperature), over which the attractive coulomb potential of the electronhole pairs extends and charge carrier recombination takes place.

4.4 Wide-field photocurrent imaging of ternary blend device

Scanning photocurrent microscopy images of the ternary blend system in conjunction with transmission profiles confirms the envisaged physical processes. The measurements carried out at different wavelengths corresponding to HC and LC absorption regions are quite informative in discerning the characteristic contributions from the different processes. The variations in the I_{ph} in the scan zone are sizable and cannot be solely attributed to topographical undulations. The image

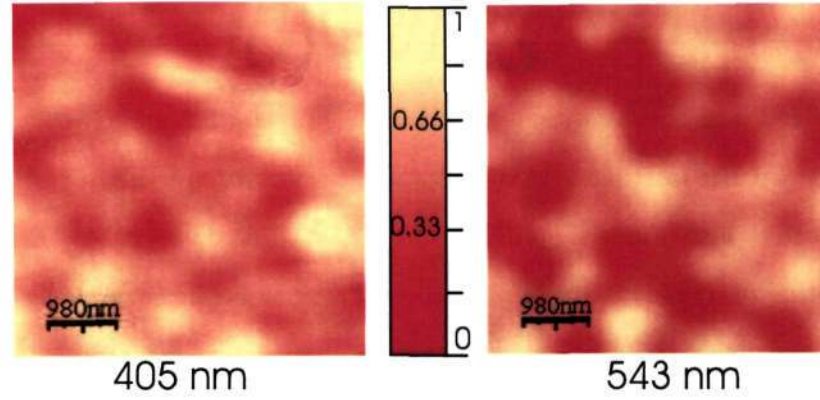


Figure 4.9: Current-contrast images of the ternary-blend device obtained by photocurrent microscopy with two different excitations (543 nm He-Ne laser with an excitation power of ~ 60 nW, and 405 nm diode laser with an excitation power of ~ 40 nW). The photocurrent images were normalized with respect to the highest magnitude and the lowest photocurrent was set as the offset value. The total scanned area was $25 \mu\text{m}^2$ and the normalized scale bar is shown for relative I_{ph} magnitudes.

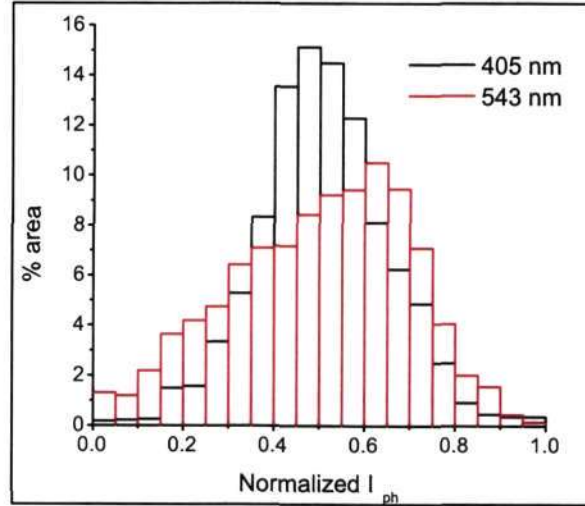


Figure 4.10: Histograms showing the area fraction of the image contributing to the different I_{ph} regions

obtained from the excitation at 543 nm ($\alpha(\lambda)_{\max}$ for HC and CNPPV) is shown in Figure 4.9. The fractional areas ($\times 100\%$) at constant intervals of normalized I_{ph} are plotted as histograms (Figure 4.10). The histogram data (at 543 nm) reveals $\sim 35\%$ of the total area are high I_{ph} regions. These high-efficiency regions primarily indicate HC/CNPPV interfaces. The intermediate efficiency can be attributed to regions of HC-MEHPPV or CNPPV-rich domains and the non-responsive regions correspond to the LC polymer forming an inert matrix. The images obtained from 405 nm excitation are significantly different, with most of the area ($\sim 55\%$) covered by average photocurrent regions as a result of the HC:LC/LC:CNPPV rich domains. At this wavelength, high photocurrent regions form approximately 24 % of the total area, and primarily indicate LC rich domains with HC:CNPPV domains in their close proximity, facilitating energy transfer from LC to HC followed by charge transfer at the HC/CNPPV interface. This analysis suggests that the efficient charge-transfer regions constitute only 24 to 35 % of the total scanned area ($25 \mu\text{m}^2$) that contributes to the high photocurrent.

4.5 JV-characteristics

Comparison of the solar-cell characteristics of the devices validates the spectroscopic observations and inferences. Current density (J)voltage (V) response (Figure 4.11) of three devices under illumination indicate large values of short-circuit current density (J_{SC}) for the ternary HC:LC:CNPPV (2:1:2) devices and low values for the LC:CNPPV device. The dark JV characteristics of the ternary-blend device showed ohmic behavior at low electric field (from 0 to 1 V), albeit the injection current is very low in this regime. At high electric field, the JV characteristics do not follow the simple space-charge law. The open-circuit voltage (V_{OC}) was quite

high (1.1 V) in all cases. The fill factor ($FF = 12\%$) and J_{SC} ($\sim 80 \mu A/cm^2$) in the ternary-blend device were limited by the high series resistance, which was reflected in the low forward current at comparatively high field. While the observed photocurrent was sufficiently high, the overall power-conversion efficiency ($\eta_P = 1\%$, under monochromatic illumination at 530 nm and with intensity of $\sim 1 \text{ mW}/\text{cm}^2$) of the device was limited by the low FF. The high series resistance can be attributed to the barrier formation at the electrode/polymer interface. The barrier can arise from the work function mismatch and presence of a thin aluminum oxide layer between the polymer and the cathode.

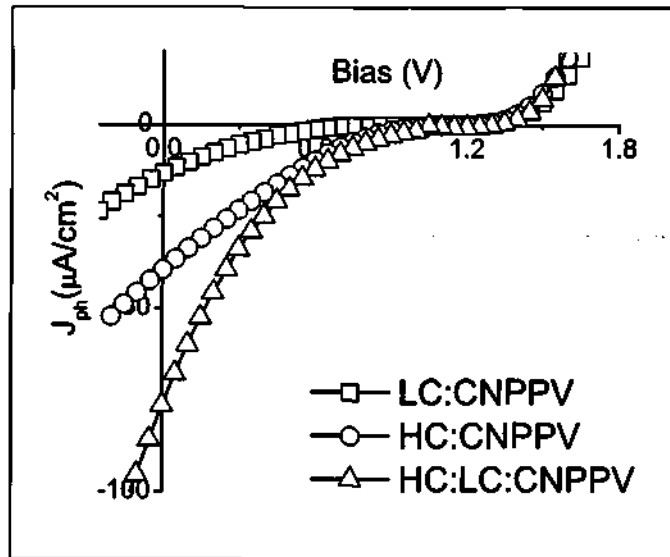


Figure 4.11: The JV characteristics of the devices, under monochromatic illumination at 532 nm with an intensity of $1 \text{ mW}/\text{cm}^2$. The ternary-blend device gives the best performance open-circuit voltage, $V_{OC} = 1.1 \text{ V}$, $J_{SC} = 80 \mu A/cm^2$, fill factor $FF=12\%$, $\eta_P = 1\%$, under monochromatic illumination, $\lambda \sim 530 \text{ nm}$ and incident power density, $P_{inc} = 1 \text{ mW}/\text{cm}^2$

4.6 Summary

Efficient ternary-polymer-blend DA solar cells, with the donor part consisting of the blend of high-conjugated (100%) and low-conjugated (10%) MEHPPV in a 2:1 weight ratio along with the CNPPV acceptor, have been demonstrated. It has been observed that the ternary-blend diodes are more efficient than the homopolymer-acceptor diodes. The surface photocurrent profiles point directly to the more active HC/CNPPV interface, compared to the LC/CNPPV interface, for charge-transfer processes. The LC polymer behaves as a host polymer and photosensitizer, which transfers energy to the fluorescent dye polymer (HC) by a Förster-type mechanism and thus improves the total photo-conversion of the ternary-blend device in the blue part of the spectrum, whereas in the red region the observed enhancement is mainly because of enhanced effective mobility. The overall spectral response of the photodiode improves and the excitons in the LC-chain finds a new transport pathway to give rise to free charge carriers. The ideal morphology for a photovoltaic device has been shown in Figure 4.12 where, HC-CNPPV (efficient interface for charge transfer process) and LC-HC (efficient interface for energy transfer) interface is maximized and LC-CNPPV (not so efficient interface for free charge carrier generation) is minimized. Isolating LC-polymer from CNPPV, may maximize the energy transfer process. Ideally LC should be encapsulated within HC. A partial encapsulation of LC inside HC was achieved by introducing controlled amount of non-solvent in the system (see Appendix for more details). However devices were not realized using that route.

To achieve the gradient in concentration the depth dependent curing procedure [168] was adopted. The patterning scheme has already been detailed in

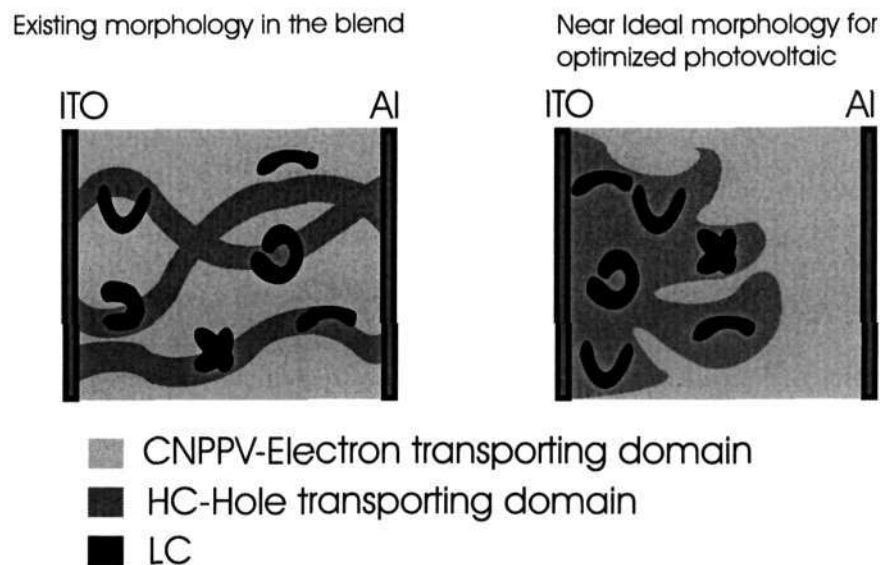


Figure 4.12: Postulated blend morphology. LC polymer should be encapsulated within HC to minimize LC-CNPPV interface and increase the HC-CNPPV interface. This will isolate energy transfer process from charge transfer process.

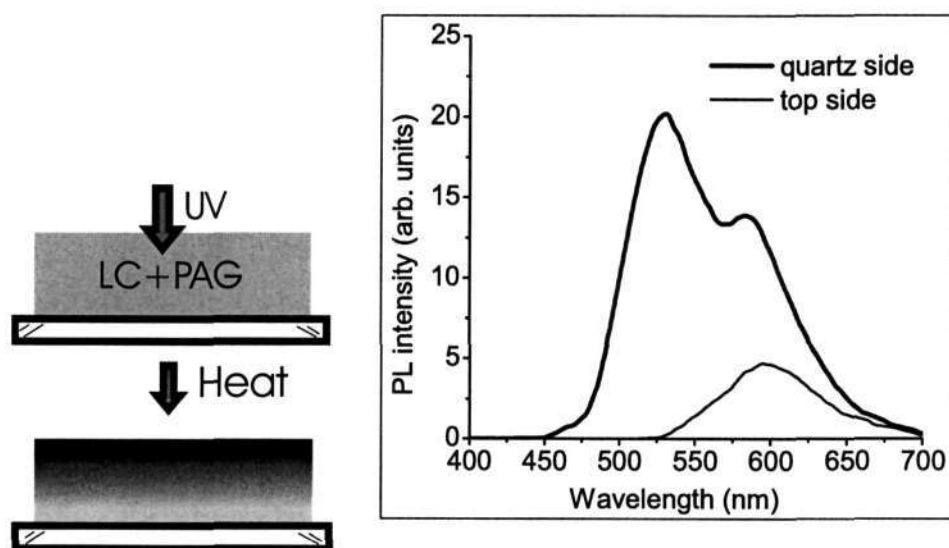


Figure 4.13: PL spectrum from both side of the film reveals that there is higher concentration of HC on the top and higher concentration of LC at the bottom. The film thickness was high ($\sim 15 \mu\text{m}$) and the curing was done by 370 nm light.

Section 3.3. The resulting concentration profile was probed by PL spectrum from both sides of the substrates (Figure 4.13) and shows the clear indication of HC polymer at the top and LC polymer at the bottom. The relative difference in PL intensity is due to the different fluorescence quantum yield. The film thickness was too high ($\sim 15 \mu\text{m}$) to be used as an active layer in solar cell. However, with lower wavelength UV radiation, the thickness can be minimized.

The vertical concentration gradient is difficult to achieve in these systems. Layer by layer deposition as has been adopted in many cases [190], was attempted. Bilayer structures with a bottom layer consisting of a blend of HC and LC polymers in a 2:1 weight ratio and top layer consisting of an HC:CNPPV blend in a 1:1 weight ratio were investigated to optimize the electrical transport from the vertical gradient perspective and minimize electrode barriers. However, this bilayer structure did not result in higher efficiency and is probably limited by the presence of defects at the bilayer junctions. In spite of the designing limitations, it has been successfully demonstrated that the presence of LC polymer can enhance photon harvesting. This method of blending three components for efficient light harvesting offers a promising route to developing polymer-based solar-cells [191].

CHAPTER 5

CORRELATING CONTACT EFFECTS TO THE REDUCED FILL-FACTOR

5.1 Introduction

A large part of contemporary research on polymer solar cells involves design and synthesis of novel polymeric systems. From the device performance perspective a crucial factor to realize the maximum impact of different strategies finally depends on better fill factor of the device which is more sensitive to bulk-material properties, blend morphology, degradation [192, 193] and the physio-chemical morphology of the polymer-cathode interface. Apart from bulk issues the electrode-active layer interface plays an important role. Realistic deposition conditions of cathode lead to a variety of physical (in form of void space) and chemical defect features which can be detrimental. We emphasize this aspect in our studies using high performance model D-A blend systems, by monitoring the dependence of the solar cell parameters.

Photogeneration of charge carrier is preceded by the dissociation of exciton at the D-A interface (with quantum efficiency η_{CT}). Once the exciton is dissociated the charge collection efficiency (η_{CC}) does not approach 100 % under short circuit condition [194] since, the polaron pair (with hole on the D-chain and electron on the A-chain) created after dissociation is still bound by mutual coulombic interaction

and this charge-transfer exciton has finite lifetime. The formation of free electron and hole pair is highly field and temperature dependent process which is reflected in the reverse bias photocurrent (J_{ph}) behaviour [32]. In ideal case, the probability of free carrier formation from the bound polaron pair should not depend on the field across the device. In P3HT:PCBM devices where a good FF ($< 50\%$) has been observed this near ideal behaviour is followed and the J_{ph} essentially saturates at high reverse bias indicating the fact that almost all the photogenerated free charge carriers are extracted from the device. However in most of these systems J_{ph} in the reverse bias shows mild field dependence. A strong field dependence of J_{ph} reduces the FF significantly. Since near V_{OC} , ($V_{sat} < V < V_{OC}$, V_{sat} is the saturation voltage at which J_{ph} switches from linear to saturation regime) the effective field in the device is low, a strong field dependent exciton dissociation rate changes the curvature of the JV -response and it tends to become concave. Besides the field-dependent exciton dissociation rate, unbalanced transport of charge carriers can also play a major role.

It has been discussed in Section 2.5 that the unbalanced carrier mobility give rise to carrier accumulation and consequent space charge effect. To recapitulate, let us briefly discuss the phenomenon here and its effect on the device FF. In case of perfect ohmic contacts (non-injecting in the reverse bias mode) the behaviour of the illuminated JV response depends on the drift length ($L_D = \mu\tau F$, where, μ is the mobility, τ is the lifetime of the charge carriers and F is the field across the device) of the electrons (e) and holes (h) and the ratio (b) of their drift lengths ($b = \mu_e\tau_e/\mu_h\tau_h$) [141]. For balanced transport ($b \sim 1$), J_{ph} varies linearly with V at lower voltage regime and at higher voltage it saturates to a value $J_{ph} = qG(F,T)d$, where, q is the charge, G is the generation rate, F is the electric field, T temperature and d active-polymer layer thickness [34]. At this point L_D becomes

equal or greater than d . However in case of unbalanced transport ($b < 1$ or $b > 1$), which is also known as ' $\mu\tau$ -limited' process, carrier accumulation takes place near both the contacts modifying the field and in absence of any recombination the thickness of the accumulation region (s) is governed by the smaller μ . In an extreme case ($b \ll 1$ or $b \gg 1$), the slower charge carrier will accumulate near one of the electrode to a greater extent leading to build up of an internal field. When the field in this region becomes equal to the external applied voltage (V), the current becomes 'space charge limited' (SCL). Under SCL condition $J_{ph} = qG[(\mu\tau)_{\text{slow carrier}}]^{0.5} V^{0.5}$. A fundamental electrostatic limit for the build-up of space charge is reached when J_{ph} becomes equal to $J_{SCL} (= 9/8\epsilon_0\epsilon_r\mu_{\text{slow carrier}})$. Using this condition, the electrostatically allowed maximum photocurrent density is given by Equation 2.16 [128, 140]. Both in SCL and $\mu\tau$ -limited case J_{ph} shows a square root dependence on V and at higher voltage J_{ph} saturates. However the J_{ph} varies linearly with G , hence with the intensity of illumination (P) in $\mu\tau$ -limited case and shows a three-quarter dependence on G (or P) in SCL case. The square root dependence on voltage limits the maximum possible FF to 42 % in SCL-case [140]. $J_{ph} \propto (V_0 - V)^{1/2} \Rightarrow J_{SC} \propto V_0^{1/2}$. In the maximum power point,

$$\left[\frac{\partial}{\partial V} (J_{ph} V) \right]_{V=V_{\max}} = 0 \quad (5.1)$$

Hence, $V_{\max} \propto \frac{2}{3}V_0$ and $J_{\max} \propto (\frac{1}{3}V_0)^{1/2}$. This dependence give rise to a FF of 40 %. SCL- J_{ph} as seen in Equation 2.16 does not depend on thickness d . For non-SCL devices the saturation photocurrent is approximated by qGd . Consequently increasing d will result in a higher J_{ph} due to enhanced absorption. With increasing d , a transition has been observed from non-SCL to SCL behaviour where the J_{ph} reached the (d independent) space-charge limit given by Equation 2.16 [195]. The

thickness d also determines the slope ($= \mu\tau/d^2$) of the JV -curve (in the range $V_{\text{sat}} < V < V_{\text{OC}}$) [196, 197]. A steeper slope moves V_{sat} closer to V_{OC} and hence increases the FF.

SCL behaviour has been demonstrated for a blend of PPV derivative and PCBM where μ_h in PPV phase ($\mu_h \sim 3.2 \times 10^{-5} \text{ cm}^2/\text{Vs}$) is two orders of magnitude lesser than the μ_e in the PCBM phase ($\mu_e \sim 4 \times 10^{-3} \text{ cm}^2/\text{Vs}$) [140]. For balanced transport and better FF, a DA pair with comparable $\mu\tau$ -product is always preferable. From this point of view, DA pairs, P3HT ($\mu_h \sim 10^{-4} \text{ cm}^2/\text{Vs}$)-PCBM ($\mu_e \sim 10^{-3} \text{ cm}^2/\text{Vs}$), and MEHPPV-CNPPV ($\mu_e = \mu_h \sim 10^{-5} \text{ cm}^2/\text{Vs}$) should show comparable

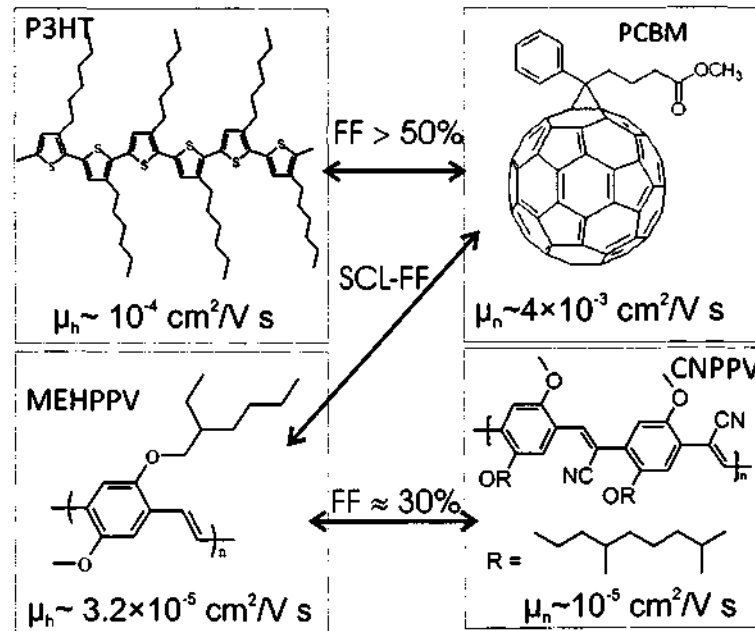


Figure 5.1: The scheme summarizes the observed fill-factor for commonly used donor-acceptor pairs. P3HT:PCBM and MEHPPV:CNPPV both has balanced mobility values although MEHPPV:CNPPV devices show a general trend of low ($\approx 30\%$) FF. In case of MEHPPV:PCBM, the mobility difference is high which give rise to space-charge limited (SCL) fill-factor.

efficiency. Experimentally in spite of a higher V_{OC} of $\sim 1.2 \text{ V}$, all active-

polymer solar cells based on MEHPPV-CNPPV blend have much lower FF ($\sim 30\%$) [173, 174, 198, 199, 200] resulting in a lower PCE as compared to P3HT-PCBM (FF $\sim 68\%$) [99] devices which can be attributed to the lower mobility and consequent field dependent exciton dissociation rate in PPV systems [200] (Figure 5.1). Solar cells based on small molecules are also capable of giving high FF (50%) [201]. However lowering of FF (25%) [202, 203] due to the “S-shaped” JV -response, has been observed in these systems as well. Thus the bulk can reduce the FF in two ways: (i) strong field-dependent exciton dissociation rate and (ii) unbalanced transport and consequent space charge effect. The characteristic ‘S-shaped’ JV curve is the signature of a counter-injecting diode which arises due to charge accumulation near one of the electrode. Charge carrier accumulation can be a contact-driven process and in this chapter the importance of contact-effects to the FF has been demonstrated in the two model systems of P3HT-PCBM and MEHPPV-CNPPV where transport is balanced and exciton dissociation is weakly dependent on the applied field.

5.2 Field dependence of photocurrent

The JV characteristics measured in the dark (J_D) and under illumination (J_L) with white light are shown in Figure 5.3 for P3HT-PCBM solar cell with Ca cathode. $J_L(V)$ gives rise to a FF of 62.6% under white light illumination of 80 mW/cm² leading to a moderate PCE of 1.5% (neglecting reflection losses). Similar efficiency was achieved under AM1.5 (100 mW/cm²) illumination. The photocurrent ($J_{ph} = J_L - J_D$) when plotted against the effective applied bias voltage ($V_0 - V$) (where $V_0 \sim 0.64$ V is the compensation voltage, defined by the voltage at which the $J_{ph} = 0$), linearly increases with voltage at low effective field ($V_0 - V \leq 0.1$) and for high

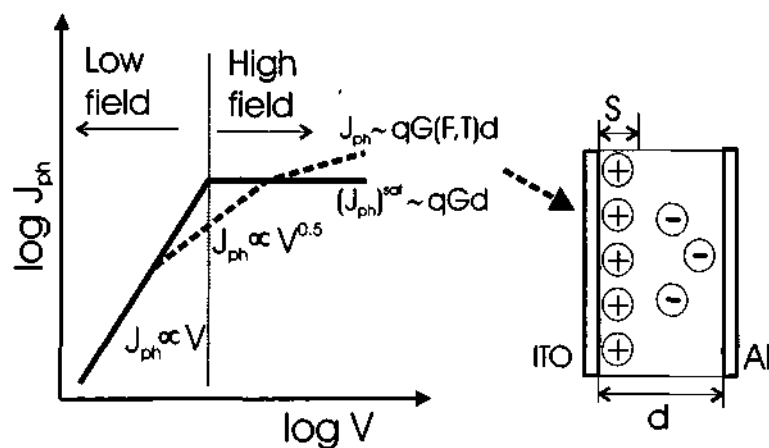


Figure 5.2: Schematics of photocurrent in the fourth quadrant plotted in log-log scale has been shown. The solid line is the ideal response. In presence of SCL-condition, the square root behaviour on voltage comes into play. At high reverse bias the J_{ph} always show a mild field dependent increase.

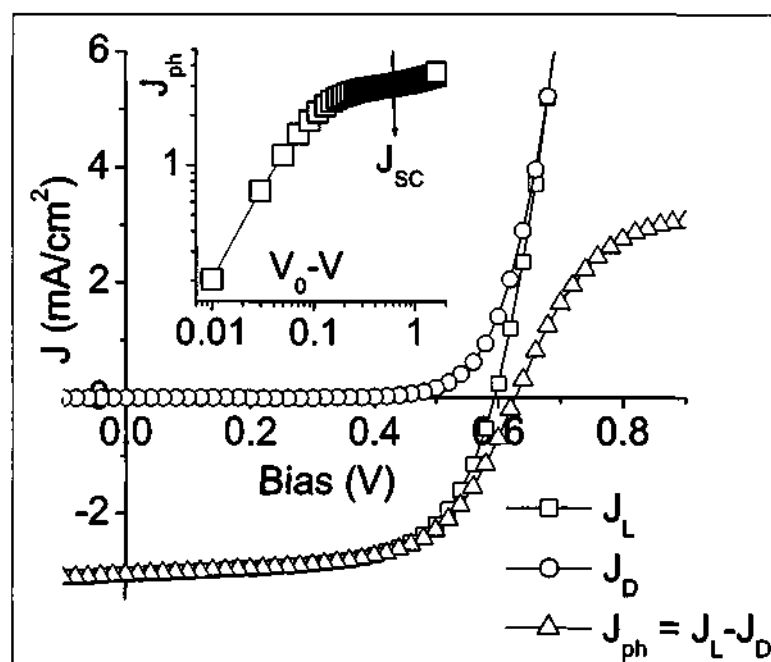


Figure 5.3: JV -characteristics of a P3HT-PCBM solar cell with active area 25 mm². The device shows $J_{sc} = 3.08$ mA/cm², $V_{oc} = 0.59$ V and FF = 62.6 % under white light illumination with $P_{inc} = 80$ mW/cm²

effective field ($V_0 - V > 0.1$), J_{ph} gradually saturates to the value, $qG(F, T)d$ and shows a weak field dependence (assuming no charge carrier recombination) [34]. These devices (with $d \sim 100$ nm) have no significant SCL contribution. The dissociation efficiency is quite high and weakly dependent on field since almost one sixth of the total photogenerated charge carriers (which give rise to saturation photocurrent in high effective field region), is already dissociated in the low effective field regime. The performance of PSC can be adjudged by the second derivative (d^2J/dV^2) or the extent of convexity which is positive in the region $V_{\text{sat}} < V < V_{\text{OC}}$, where $V_{\text{sat}} \sim 0.4$ V.

5.3 Cathode-polymer interface effect on FF

Replacing the Ca electrode with Al gives rise to a point of inflection near V_{OC} and subsequent concavity in the fourth quadrant ($d^2J/dV^2 < 0$ in the range $V_{\text{sat}} < V < V_{\text{OC}}$) of the JV -characteristics with similar magnitude of J_{SC} and V_{OC} as has been shown in Figure 5.4. Work function differences do not significantly alter V_{OC} which is in accordance with the idea that V_{OC} is controlled primarily by the energy levels of the DA materials. The morphology and the chemical integrity of the interface play crucial roles in the $J(V)$ mechanism. Slow evaporation rate or an inverted geometry has been speculated to be useful to get a better PCE with Al cathode [204, 205]. In the present case, Al electrode formed by slower deposition rate appeared to improve the FF with magnitude approaching the values corresponding to Ca electrode (which was less sensitive to the deposition rate) devices.

High rates of deposition led to increased concavity in the JV -characteristics. The inhomogeneity of interfaces is higher with a rapid evaporation rate of metal as evident in the AFM surface images. The RMS roughness of the slowly grown

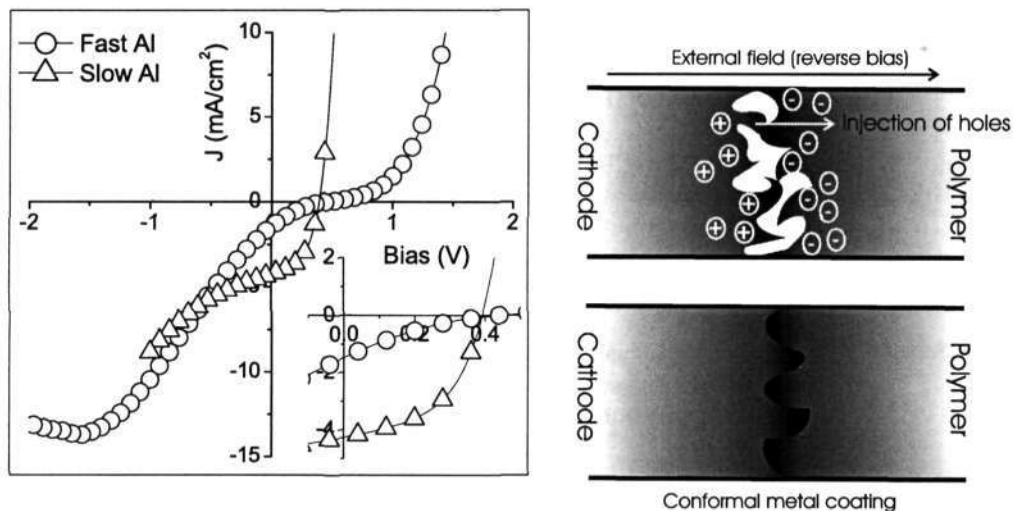


Figure 5.4: Illuminated JV -characteristics of a P3HT-PCBM solar cell with Al deposited at an extremely fast evaporation rate (200 nm/5 sec) and at slow evaporation rate (200 nm/100 sec). The fast evaporation process of Al gives rise to concavity in the fourth quadrant and consequently a low FF of 12.5 %, with $V_{OC} = 0.52$ V and $J_{SC} = 1.47$ mA/cm² ($P_{inc} = 20$ mW/cm²). The slow evaporation rate improves the FF to 45 %, with $V_{OC} = 0.4$ V and $J_{SC} = 4.3$ mA/cm² ($P_{inc} = 80$ mW/cm²). The schematic on the right represents the interface morphology (top: fast evaporation, bottom: slow evaporation).

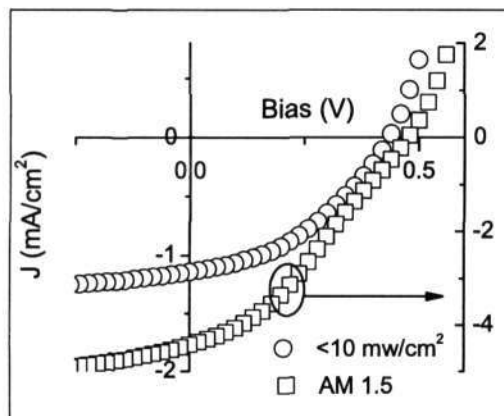


Figure 5.5: Illuminated JV -response of a P3HT-PCBM solar cell with chemically modified Ca cathode under different intensity of illumination. With standard AM1.5 illumination the FF is 28 %, while under low intensity illumination (< 10 mW/cm²) the kink in the fourth quadrant disappears and the FF becomes 36 %.

Al was ~ 1.37 nm, whereas that for the fast grown Al was ~ 1.13 nm. The image (Figure 5.6) shows the occurrence of local big domains and large voids space in case of fast evaporation. The close packing feature which is present in slowly grown Al is not seen in the fast grown Al. A simplistic analysis of bias dependent Schottky-type depletion width can explain the lowering of the J_{ph} in $0 < V < V_{\text{OC}}$ region. In maximum power point the device is operating under a bias of 220 mV (corresponding field $\sim 2.2 \times 10^4$ V/cm) which makes the current at this point (J_{max}) to be only 7 % of J_{SC} . This argument is not applicable for PSCs with a slower, more uniform coated Al layer. The difference can be reconciled to the metal-polymer reaction leading to different barrier levels and widths under different thermodynamic conditions [206]. Under high reverse bias the current tends to saturate (Figure 5.4). The generation rate for Al-cathode devices $G \approx 9.1 \times 10^{24} \text{ cm}^{-3}\text{s}^{-1}$ as obtained from the saturated photocurrent is much higher than the Ca-cathode devices ($G \approx 1.8 \times 10^{24} \text{ cm}^{-3}\text{s}^{-1}$) under same intensity of illumination. This indicates that the possibility of reverse injection of holes from the cathode in case of Al devices can not be overruled.

A non-uniform contact or incomplete coverage of the metal over the polymer surface can result in a scenario of charge accumulation leading to a barrier formation which can possibly explain the resulting $J(V)$ response. As it has been depicted schematically in Figure 5.4, the polymer film has a microscopically rough surface, so that the metal does not have uniform contact and there are a vast number of sites forming blind alleys, which act as electron traps. High electron density over a very sharp edge (\sim nm) gives rise to concentrated electric field which facilitates the injection of holes from the metal (under large reverse bias). This explains the high photocurrent observed in reverse bias regime in a fast-grown Al-cathode device. This phenomenon is quite similar to the photo-multiplication observed in n-type

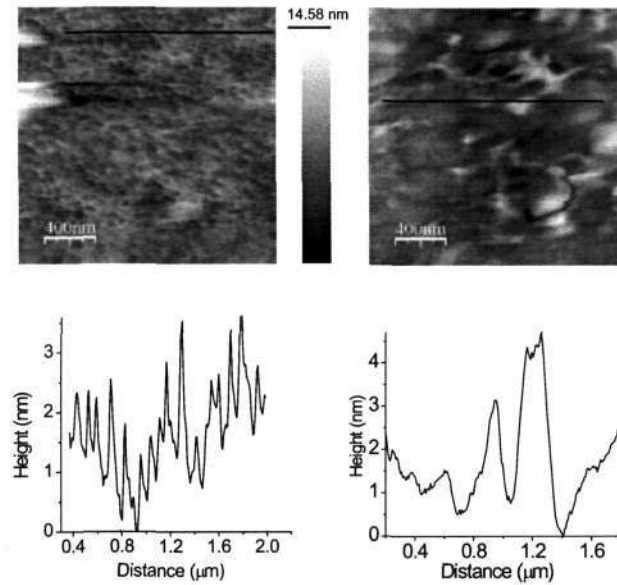


Figure 5.6: AFM image of a slowly grown Al film (on the left) surface on the polymer film (scan window size $2 \mu\text{m} \times 2 \mu\text{m}$). Image indicates the appearance of small grain-like islands which are closely packed. The AFM image of a fast grown Al film shows occurrence of local large domains with void spaces.

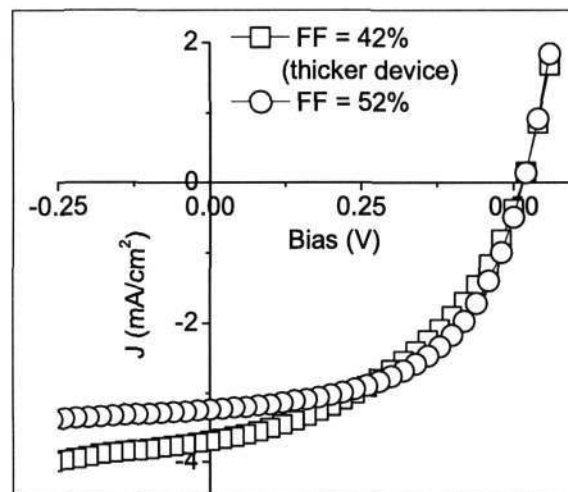


Figure 5.7: Illuminated JV-response of devices with different active layer thickness. Incident power density ($P_{\text{inc}} \sim 80 \text{ mW/cm}^2$). Higher thickness reduces the FF and the J_{SC} increases due to enhanced absorption.

perylene pigment [207, 208, 209]. A thin layer of aluminium oxide present in the cathode-polymer interface has also been shown to facilitate the injection of electrons from the cathode when significant amount of holes accumulated in the Al_2O_3 -polymer interface, in an OLED geometry [210]. This has significance with the present result where we speculate a reverse injection of holes from the cathode under high density of electron traps in the interface. A bias dependent quantum efficiency measurement can give valuable insight of this phenomenon. The reduction of FF can also arise due to the chemical degradation of the metal-polymer interface. These observations were confirmed on samples exposed over 2-weeks with Ca cathode which showed the signature of degradation due to exposure to ambient conditions where the appearance of a 'kink' (second point of inflection where d^2J/dV^2 changes its sign from negative to positive) in the fourth quadrant reduces the FF by half (Figure 5.5). The kink in the fourth quadrant, which is suppressed at low light intensity ($P < 10 \text{ mW/cm}^2$), is indicative of a defect induced recombination process. FF also depends on the active polymer layer thickness [211]. In case of thicker devices V_{sat} shifts towards the origin. Saturation photocurrent stems out from the fact that the slow carrier accumulation region has become equal to the device thickness d . Therefore for higher thickness the V_{sat} becomes closer to the origin and slope of the JV -characteristics in the range $V_{\text{sat}} < V < V_{\text{OC}}$ decreases. In Figure 5.7 the effect of increasing thickness has been depicted for two different thicknesses of the devices.

5.4 MEHPPV-CNPPV blend device

The situation is however different in case of PSCs based on MEHPPV-CNPPV blends [212]. The JV characteristics of a MEHPPV-CNPPV device indicate $\text{FF} \sim$

20 % for Al and 28 % for Ca electrodes. J_{SC} is one order of magnitude smaller in Al-devices due to the higher series resistance ($R_S A \sim 95 \text{ k}\Omega\text{-cm}^2$) as compared to Ca-devices ($R_S A \sim 0.4 \text{ k}\Omega\text{-cm}^2$). The dark JV -characteristics is almost symmetric in the entire voltage range (-2 V to +2 V). The high J_D in the reverse bias region can be attributed to the carrier injection through the CNPPV phase in reverse bias mode and not to the mechanical pinholes.

Occurrence of high reverse- J_D has been observed in devices with different area (ranging from 1 mm² to 25 mm²). The strong increase in J_D in the forward bias above 0.8 V is an indication of current through MEHPPV phase. This suggests MEHPPV phase also connects to both the electrodes and the blend is co-continuous. The reason for a low fill factor can be attributed to the poor rectification property from the high reverse injection current which competes with the diffusion current under illumination apart from the lower exciton dissociation rate arising from the low carrier mobility that prevails in these systems [200].

5.5 Interface manipulation with meltable cathode

The hypothesis was further confirmed based on the study with a low melting point (MP) cathode alloy of In-Sn-Pb-Bi ($\sim 58 \text{ }^\circ\text{C}$). This alloy forms an ohmic contact with the polymer and is a good electron collecting cathode. This thermally deformable cathode layer also provides a direct evidence of the importance of the cathode morphology on the FF. P3HT-PCBM solar cell characteristics with this cathode were carried out on a hot-stage in a microscope platform. This system using the low MP alloy can be used to gauge the effects caused by physical and the physio-chemical features at the interface. The physical effect appear in terms of the effective contact area between the metal alloy and the semiconductor while

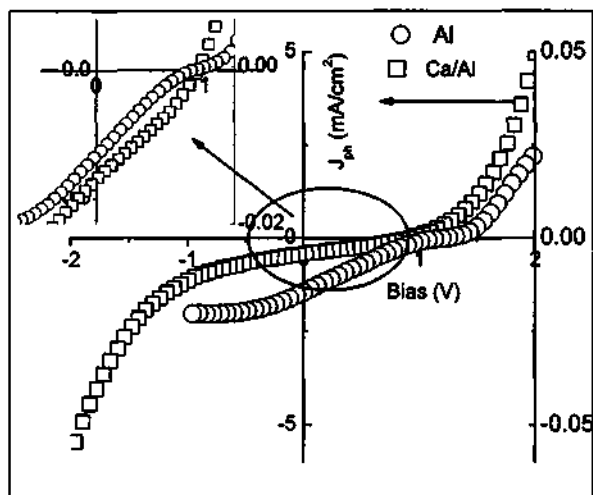


Figure 5.8: The JV characteristics of a MEHPPV-CNPPV device with Al and Ca/Al cathodes, under monochromatic light illumination of power density of 1 mW/cm². For Al cathode, $J_{SC} = 0.015$ mA/cm², $V_{OC} = 1.18$ V, and FF=20 %. For Ca device, $J_{SC}=0.43$ mA/cm², $V_{OC} = 0.76$ V, and FF=28 %.

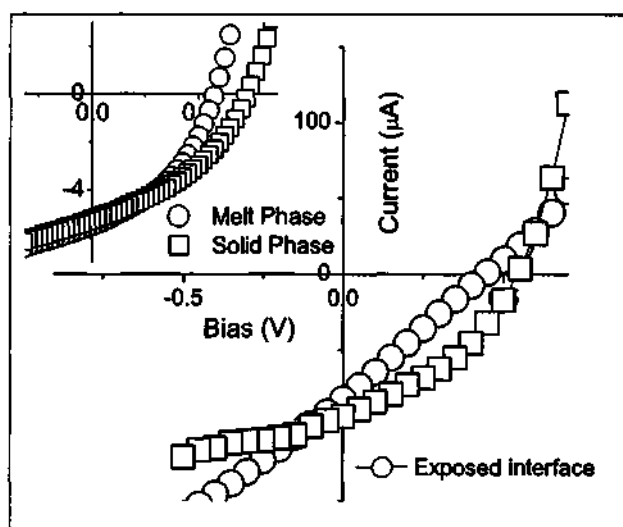


Figure 5.9: IV characteristics of a P3HT-PCBM blend solar cell. Active device area was 4 mm² with meltable alloy as the cathode showing the FF 37.66 % and 24.8 % when the interface is contaminated. FF in the melt phase is 41 % and 38 % in the solid phase.

the trapped oxygen and moisture upon freezing the sample acts as the source for an additional oxide-barrier layer. The similarity of the IV in the melt phase (at 60 °C) and solid phase (at 45 °C) of the cathode in the device shown in Figure 5.9 indicates similar contact area for the two phases with a high FF of 40%. However, during the solidification process if defects are introduced the IV drastically changes with a significant field dependent reverse bias $I(V)$ as shown in Figure 5.9 and a low FF of 24%. The effects related to the heating and cooling rate of the cathode and the consequent structures at the interface are currently being pursued in our laboratory.

5.6 Summary

In conclusion, it has been observed that the shape of the JV -characteristics in the power generating fourth quadrant strongly depends on the quality of polymer cathode interface and does not always reflect the bulk characteristics. A partial metal coverage or a chemically modified layer can reduce the fill factor drastically in an otherwise efficient solar cell device. The most commonly known bulk-limiting factors, such as space charge effect due to difference in mobility numbers and strong field dependence of dissociation efficiency seem to be secondary in these cases. Physio-chemical defects in the polymer metal interface gives rise to the charge carrier accumulation (due to inefficient collection) and the consequent space-charge like effect. For better FF, a conformal coating of metal which follows the polymer surface undulations is always preferable. These results show a clear distinction between generation-transport occurring in the bulk and carrier collection efficiency which is determined by cathode-polymer interface morphology. An identifiable direct signature of this effect manifests in the the profile of the JV -characteristics.

CHAPTER 6

EFFECT OF CATHODE DIMENSION AND GEOMETRY ON PERFORMANCE OF SOLAR CELL

6.1 Introduction

Organic solar cells are intensely being studied as a potential photovoltaic (PV) device due to the solution processing methods and the relative ease in fabrication. The combination of unique semiconducting electronic property and mechanical aspects similar to conventional plastics are attractive features in spite of the lower efficiencies prevailing in these systems. The increasing number of reports necessitates accurate estimation of power conversion efficiency (PCE) and appropriate comparison of devices with a uniform set of guidelines for the parameters, especially in regards to the dimensions of the PV element and the extrapolation procedures of the parameters to large area pixilated structures [213, 214].

In BHJ-PSC, efforts have largely been targeted to optimize the bulk morphology for efficient charge generation and subsequent transport. Efforts in optimizing the geometry and pixel dimensions and distribution has been quite negligible. Small active-area (typically $< 10 \text{ mm}^2$), defined by the overlap area of the bottom indium tin oxide (ITO) anode and top cathode have been reported to give rise to

high short-circuit current density (J_{SC}) values [215, 216]. We highlight the importance of the cathode-size and the extent of photoactive regions beyond the assumed dimensions in PSCs. This issue has been partly addressed in earlier report for organic PV devices [217, 218] however we present additional insights and observations which can potentially be utilized to design an effective grid pattern for a large area polymer photovoltaic structure.

6.2 P3HT:PCBM solar cell characteristics

For the present studies, P3HT-PCBM based PSCs were fabricated using standard protocol by spin coating the polymer solution onto the PEDOT-PSS coated glass-unpatterned ITO substrates. Devices of wide range of active-area ($0.04\text{--}1\text{ cm}^2$) were prepared by metal deposition onto the active polymer layer of P3HT:PCBM blend. Shadow mask arrangements were used to pattern accurate, predefined square electrodes on the active layer with asymmetry factors (cathode area /ITO area) ranging from 10^{-3} to 10^{-1} . These devices were tested under complete illumination using collimated white light source. PCE of $\sim 2\%$ was achieved for a prototypical device under AM1.5 illumination. A batch of devices for the present studies which represented a slightly lower PCE but which could be reliably reproduced was chosen. The J (current/cathode-area)- V (Figure 6.1) for these representative devices indicates J_{SC} in the range of 1.78 mA/cm^2 (PCE $\approx 0.6\%$)– 1.42 mA/cm^2 (PCE $\approx 0.48\%$). In all the batches of samples a general trend of reproducible high J_{SC} value for small area devices was observed. The decay of J_{SC} for different area devices in general follows a $1/x$ (\sim perimeter/area of the cathode) decay profile where x is the length of the sides of top square-shaped cathode (Figure 6.1). V_{OC} however remains unaffected and was observed to be independent of x over a wide range.

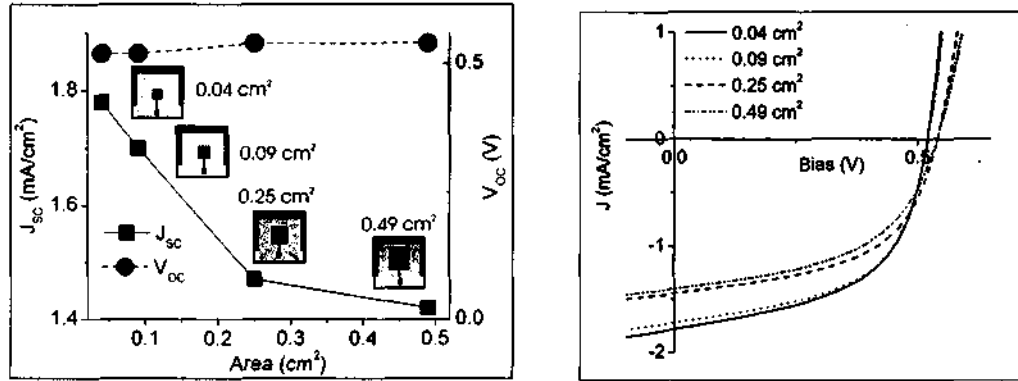


Figure 6.1: JV characteristics of the P3HT-PCBM solar cell with different active area under flooded illumination with white light of intensity 80 mW/cm^2 . Devices were fabricated on two different substrates with pixel size 4 mm^2 , 9 mm^2 (substrate 1) and 25 mm^2 , 49 mm^2 (substrate 2). The variation of J_{sc} and V_{oc} has been depicted (the left figure).

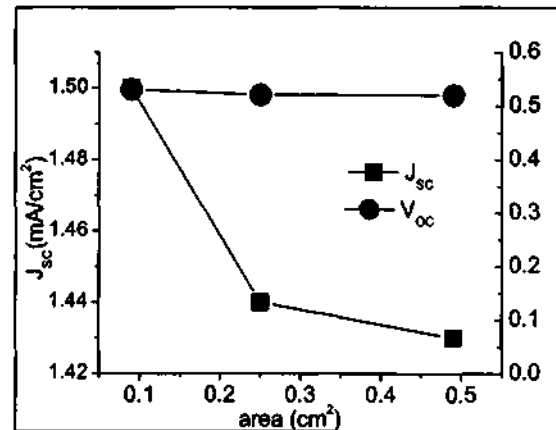


Figure 6.2: A second set of results fabricated from a different batch of samples (P3HT:PCBM) exhibiting the scaling of photocurrent dependence on the cathode-area. The J_{sc} magnitude varied from 1.50 mA/cm^2 (for 0.09 cm^2 device) to 1.43 mA/cm^2 (for 0.49 cm^2 device) under collimated, broad white light illumination of intensity $\sim 80 \text{ mW/cm}^2$. V_{oc} remains largely independent of the area.

Experiments were then carried out to estimate the significant, apparent contribution from the non-overlapping region. For this, the devices were characterized using restricted illumination by inserting a mask which precisely fitted the active region and covered the peripheral regions. The metal-cathode contour was used for mask alignment while maintaining negligible shadow effects. The measurements in all the cases indicated a substantial drop of I_{SC} (by $\sim 15\%$ for 0.25 cm^2 device) as compared to the flooded illumination which also illuminated the peripheral regions around the active region (Figure 6.3).

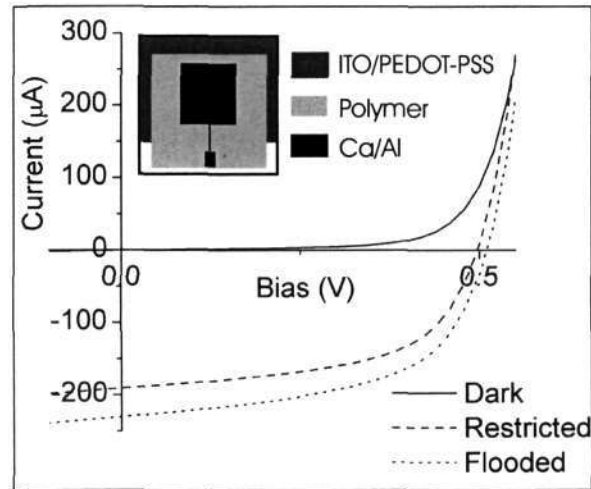


Figure 6.3: IV characteristic of 25 mm^2 device under flooded and restricted (restricted to the overlap region) illumination. The schematic in the inset shows the device layout.

Under restricted illumination the JV -characteristics for different area devices are identical and superpose on each other, revealing that resistive-losses are not a dominant factor in the present range of devices. The finite drop across the ITO surface (between the electrical contact point and the region of illumination) barely accounts for these significant changes. Since the ITO is not patterned, contributions from the PEDOT-PSS (resistivity $\sim 0.1\ \Omega\text{-cm}$) layer is not relevant here.

6.3 Optical effects

Possible sources of the contribution from the periphery are expected to arise from diffused component of light scattered due to the surface roughness of the ITO/polymer interface (Figure 6.4). This contribution can be quantitatively addressed in terms of the haze parameter for the transmitted light (H_T) (the ratio between diffused and total [diffused + specular] light). H_T has been shown to be dependent on the RMS surface roughness (Λ) of the substrate and incident wavelength with larger contribution from shorter-wavelengths. It is an appreciable factor at visible region when Λ exceeds 40–50 nm [219]. For ~ 530 nm (EQE maximum), the H_T has been shown to be only 15% and give rise to negligible enhancement in the short-circuit current density considering $\Lambda \sim 1$ nm for ITO/PEDOT and ~ 1.37 nm for Al/polymer interface. Beam-spreading within the glass substrate (thickness ~ 1.12 mm, refractive index ~ 1.45) is a sizable factor under non-uniform illumination conditions. The optical effects arising from the glass substrate was verified by using thinner substrates such as ITO coated cover-slip glass (thickness $\sim 160 \mu\text{m}$).

Devices fabricated on these thinner substrates exhibited similar performance levels. Measurements involving restricted illumination indicated small contributions from the periphery in this case. The light distribution in the polymer medium was simulated using Fourier optics numerical simulation tools and was also verified experimentally by studying the extent of the beam spread using a near-field collection setup around the edges upon irradiating the sample in the far-field. The Fourier simulation using the expression (Equation 6.1) below indicates a spread of the beam only to the extent of few microns. The light intensity spread contour is calculated with unit-less quantity, as discussed by Wilson [220].

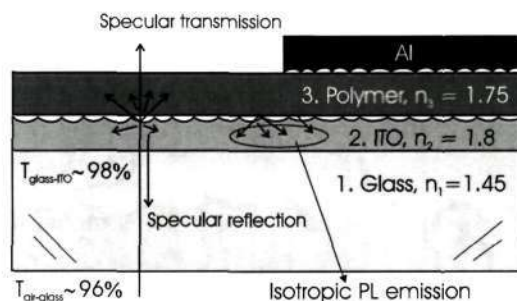


Figure 6.4: The possible optical effects that can give rise to enhancement in measured photocurrent are (i) scattering inside the thick ($1.12 \mu\text{m}$) glass substrate (ii) waveguiding of isotropically emitted PL emission from the active polymer layer (iii) scattering in the ITO-polymer interface due to surface roughness. Waveguiding inside the ITO slab is negligible due to extremely small thickness ($\sim 500 \text{ nm}$) and reflectivity $R_{\text{ITO-polymer}} \sim 10^{-4}$ since $n_2 \approx n_3$. Also, the ITO-polymer interface roughness parameter (Λ) $\sim 1 \text{ nm} \ll \lambda$ ($300 \text{ nm} - 700 \text{ nm}$). Hence the interfacial scattering of transmitted light for collimated near-normal incidence is also negligible. The scattering inside the glass (thickness $\sim 1.12 \mu\text{m}$) was minimized by using ITO-coated cover-slips ($160 \mu\text{m}$).

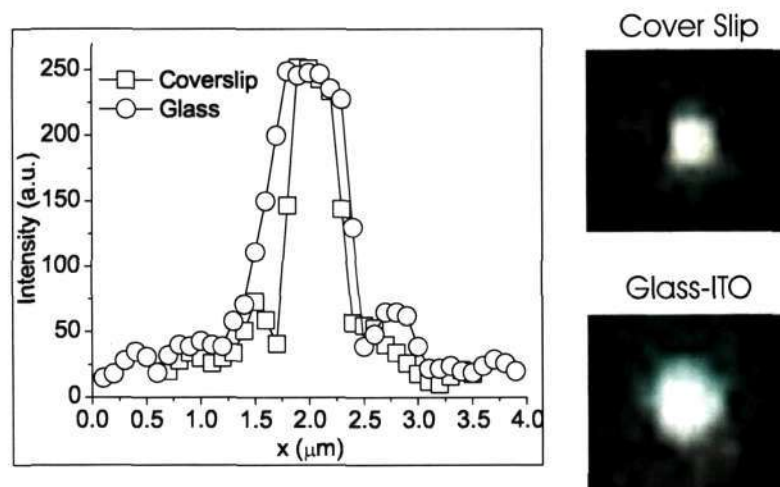


Figure 6.5: The beam profile was captured using a high-resolution CCD camera (640×480 pixels in $64 \mu\text{m} \times 48 \mu\text{m}$ area) fitted with a 50X (numerical aperture ~ 0.95 , working distance $\sim 10.1 \text{ mm}$) micro-objective lens. The laser spot ($\lambda \sim 543 \text{ nm}$, power $\sim 10 \text{ nW}$) was focused onto the sample using a 60X (working distance $150 \mu\text{m}$, numerical aperture ~ 0.55) micro-objective lens. In case of cover-slip the spot size is $0.5 \mu\text{m}$ and on the glass substrate it was $0.7 \mu\text{m}$. The broadening of the spot can be attributed to the finite thickness of the glass substrate (1.12 mm).

$$I(u, v) = A^2 \exp(-2k\beta(h + z)) \times \left| \int_0^1 J_0(\nu\rho) \times \exp(-0.5ju\rho^2) \exp(-0.5\beta(u + u_0)\rho^2) \rho d\rho \right|^2 \quad (6.1)$$

The spot is focussed at a distance h inside the polymer material by a 60X micro-objective lens with numerical aperture $\sin \alpha \approx 0.95$. β is the absorption parameter. u and v are the optical co-ordinates. Light intensity spread contour is plotted in Figure 6.6.

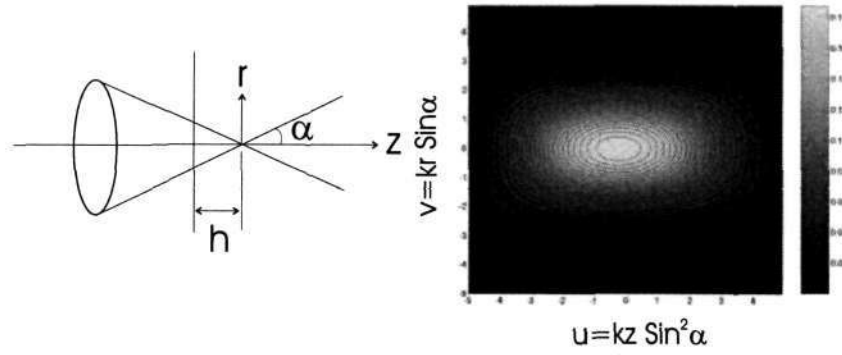


Figure 6.6: Optical beam simulation inside polymer matrix using Fourier optics formalism. Laser beam coming from 60X micro-objective lens (with cover-slip correction ring, working distance = $150 \mu\text{m}$, numerical aperture ($= \sin \alpha$) = 0.95 , $\lambda \approx 470 \text{ nm}$) focused on patterned ITO substrate.

Direct images of the scattered-light from the device using a high resolution camera also provided the intensity profiles. A small spot of light (spot size $\sim 200 \mu\text{m}$) was focused on the ITO through a 50X objective lens and the scattered intensity profile was captured from the other side with a CCD camera. For a localized incident-spot the scattering factors in the cover slips ($160 \mu\text{m}$) is 30% less than that in glass slides (1.15 mm). Consequently, the enhancement of J_{SC} from the additional peripheral illumination using a well collimated source is $\approx 5\%$

in case of cover slips as compared to 15% in case of glass substrates for similar area devices. These effects have been observed to be more pronounced in case of results from small-area illumination on a dye-sensitized solar cell on much thicker FTO coated (thickness ~ 4 nm) substrates [221]. Possibility of efficient guiding of isotropically reemitted light by the absorbing polymer species [222], coated on glass substrates is not significant in the present case because of the low emission from the acceptor quenched donor systems.

6.4 Spatially resolved photocurrent scan

Finite extent of the fringing electric field outside the coverage of Al-cathode was estimated to decay to magnitudes as low as ~ 10 - 100 V/cm within a span of 50 nm from the edge. The extent of photoactive region outside the active area was probed using spatially resolved I_{SC} measurements (Figure 6.7) with a low intensity (~ 120 nW) source incident locally using a 60 X microscope objective (~ 470 nm, spot size ~ 1 μ m) (Figure 6.5) and a stage translated at a step size of 0.5 μ m.

Measures were taken to minimize the diffusive spreading of light and minimize wave-guiding by fabricating the devices on thin ITO coated cover slip (160 μ m). The short-circuit-photocurrent (I_{ph}) decreases progressively as the light is scanned away from the overlap region of the electrodes [223]. The I_{ph} decay profiles (corrected with transmission profile) outside the Al electrode and ITO electrode reveals decay length of 16 μ m and 109 μ m respectively (Figure 6.8). It is to be noted that the I_{ph} from these measurements have their origin from the localized source of carrier generated by the narrow light source that distorts the built-in potential locally. In the steady state, a non-local lateral electric field can be set up that can self consistently induce a lateral flow of the separated carriers. This lateral

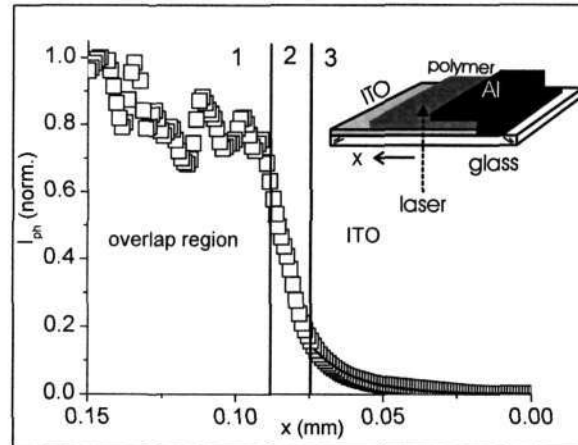


Figure 6.7: Spatially resolved short-circuit photocurrent (I_{ph}) profile of a BHJ solar cell made from P3HT-PCBM blend sandwiched between unpatterned ITO and a stripe of Al cathode. The transmission of the beam was monitored using a photodetector to determine the position of the beam. In region 1, the spot ($1 \mu\text{m}$ diameter) is completely inside the overlap region. Region 2 corresponds to the boundary region where edge effects dominate. In region 3, the spot is completely outside and the transmission is position independent. The exponential fit (solid line) to the data reveals the decay length of $16 \mu\text{m}$. Inset depicts the device structure and schematic of the measurement. The long arrow indicates the scanning direction.

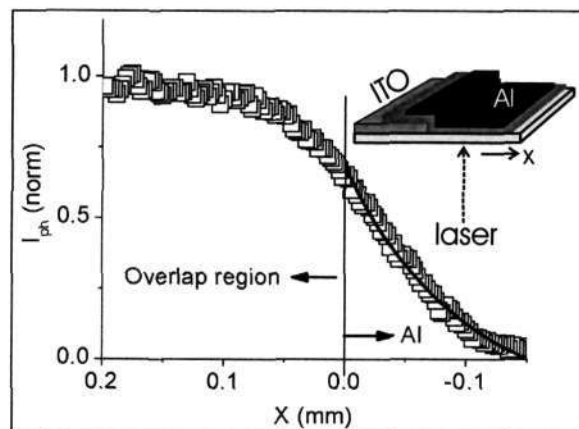


Figure 6.8: The spatially resolved photocurrent with the beam scanning the Al electrode track (outside the ITO boundary) also reveals an exponential type decay profile. The decay length $\sim 109 \mu\text{m}$.

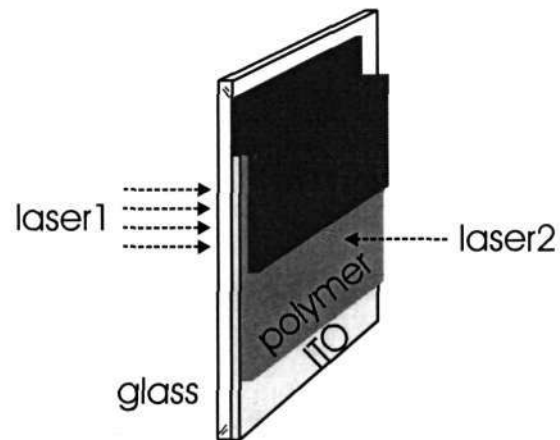


Figure 6.9: The photocurrent measurement using two beams with broad illumination restricted within the overlap region and a local point source illumination in the external region.

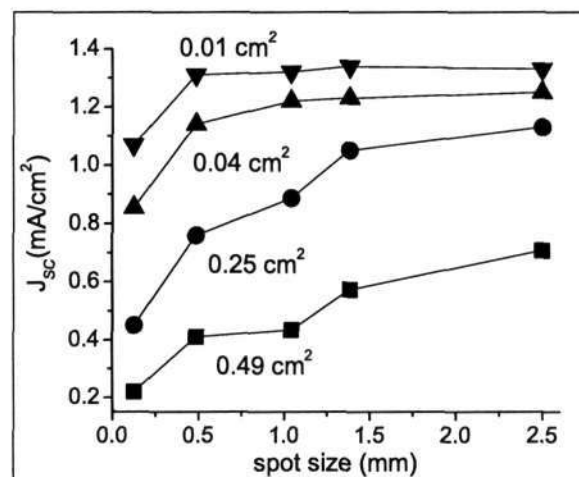


Figure 6.10: JV-response of different area devices were recorded with spot illumination from laser ($\lambda \approx 532$ nm) of different diameter centered in the overlap region. Spot diameters were: 125.61 μm , 487.59 μm , 1.04245 mm, 1.38661 mm, 2.50028 mm. The diameter of the spot was changed using a movable lens and a fixed beam expander (10X) assembly.

charge flow, which is ohmic in nature, produces a potential drop between the locus of illumination and the electrodes can be used to possibly explain the large decay lengths beyond the expected value for simple diffusion processes.

Measurements with two beams on the two regions (within the device-area and outside the device) are more appropriate to confirm the processes under broad uniform illumination. These were carried out with two light sources on a solar cell device fabricated on smooth thin ITO coated cover-slip substrate to minimize the beam dispersion. One source was directed from the ITO side onto the overlapping region in front of the Al while the second beam was incident from the opposite side, with the light focused on the region outside the Al region (Figure 6.9). A clear increase in the J_{SC} was observed when the second source was incident outside the overlapping region; however this increase was less than the sum of the values obtained from individual contributions with only one light source.

This expected non-additive feature can be understood from the differences in the charge carrier transport rate from the two carrier generation sources. The lateral diffusion process rates assisted by small field are expected to be lower than the transverse transport rates aided by the large built-in field. This feature is also evidenced in the chopper frequency dependence and transient profiles of J_{SC} from the carriers generated at the two locations. Short circuit photocurrent frequency response of P3HT:PCBM blend solar cell devices, fabricated on thin (thickness $\sim 160 \mu\text{m}$) ITO coated cover-slip, has been carried out on the overlap region as well as in the outside region. The photocurrent (RMS value) measurement using lockin-technique as a function of frequency ($\omega \sim 0$ to 3.4 kHz) reveals a progressively increasing trail in the outside regions ($\sim 60 \mu\text{m}$ away from the Al edge) and eventually exceeds the DC current value (2.32 nA under illumination with 543 nm laser spot, power ~ 215 nW). Inside the overlap region the current

value is almost constant over the concerned frequency range. The increasing profile can be attributed to the capacitive charging effect and slow rate of transport in the external regions. The beam size dependence was also observed to be markedly less sensitive for smaller area devices, beam concentrated in a small area of diameter $\sim 485 \mu\text{m}$ gave rise to the J_{SC} which differs only by $< 2\%$ as compared to a larger spot (0.025 cm^2) falling on the overlap region of a 0.01 cm^2 device (Figure 6.10).

Earlier reports on area-scaling basically dealt around the issues of the finite sheet-resistance of ITO anode which give rise to a finite loss in efficiency due to I^2R drop [224, 225]. A small elemental length dx of ITO stripe, having width b and thickness t has resistance dR , given by,

$$dR = \rho \frac{dx}{t \times b} = R_{\text{sheet}} \frac{dx}{b} \quad (6.2)$$

where $R_{\text{sheet}} (= \rho/t)$ has the unit Ω/\square . The electric power dissipated in this section is $dP = I^2 dR$. Under illumination, $I = J \times b \times x$. The total power loss P_{loss} is given by,

$$P_{\text{loss}} = \int_0^{L/2} J^2 b R_{\text{sheet}} x^2 dx = J^2 R_{\text{sheet}} b \frac{L^3}{24} \quad (6.3)$$

where L is the spacing between two metallic grid lines on the ITO slab [226]. In order to circumvent the ITO sheet resistance drop, the area of the device was required to be $< 1 \text{ cm}^2$ since for a 5% efficient solar cell (area = 1 cm^2 , $J_{\text{SC}} = 13 \text{ mA/cm}^2$, $V_{\text{OC}} = 0.6 \text{ V}$, $\text{FF} = 0.65$, $J_{\text{max}} = 10 \text{ mA/cm}^2$, $V_{\text{max}} = 0.5 \text{ V}$) the fractional power loss $p = P_{\text{loss}}/P_{\text{max}}$, given by,

$$p = \frac{P_{\text{loss}}}{P_{\text{max}}} = \frac{J_{\text{max}}}{V_{\text{max}}} R_{\text{sheet}} \frac{L^2}{12} \quad (6.4)$$

is 16% where $P_{\max} = V_{\max}J_{\max} \times bL$. Our present results suggest the benefits of further pixilation within this 1 cm^2 area of the metal cathode. The cathode pixilation which can be easily done with physical masks or printing methods can enable the device to utilize the higher efficiencies observed in smaller area device, which can more than compensate the loss arising from a decreased net active-area.

6.5 Summary

In conclusion, we have demonstrated the contributions from the optical and electrical effects to the area dependence of PCE in organic solar cells. The design of large area solar cells can incorporate factors such as the substrate thickness, beam profiles, and the possibility of the constructing an hierarchy in the patterns where the ITO is patterned at a larger length scale and cathodes are patterned at smaller levels to enable extraction of high levels of performance from these structures.

CHAPTER 7

SUMMARY AND FUTURE DIRECTIONS

A thorough study of the photophysical processes which can limit the performance parameters has been presented in this thesis. The overall results and the relevant remarks on the charge and energy transfer mechanism deciding the performance of the solar cell has been summarized.

Variable band gap poly[2-methoxy-5-(2-ethylhexyloxy)-1,4-phenylene vinylene] (MEHPPV) polymers, namely the low conjugated (LC, 10% conjugated, high band gap ~ 2.6 eV) and high conjugated (HC, 100% conjugated, low band gap ~ 2.1 eV), are model polymer systems to study energy and charge transfer processes in a ternary blend device. In the three component blend of HC, LC and CNPPV (acceptor), with optimized concentration of LC, a cascaded process of charge carrier generation takes place. Charge transfer and energy transfer efficiencies of different interfaces dictates the photogeneration quantum yield. Charge transfer in LC:CNPPV and HC:CNPPV is highly efficient, although, the photocurrent quantum efficiency of LC:CNPPV is limited by low yield of separation of bound CT-exciton. The yield can be substantiated by channeling the excitons to a relatively more efficient HC:CNPPV interface. In LC:HC interface the energy transfer efficiency is almost 100%. LC polymer absorbs blue part of the visible spectrum which give rise to generation of singlet exciton and its subsequent transfer to the nearby high conjugated (HC) segment by Förster-type energy transfer mechanism. Charge transfer and separation of the geminate pair at the HC-CNPPV interface

is highly efficient. An enhancement in the quantum efficiency was achieved in the blue region of the spectrum as well as in the green region of the spectrum. Presence of LC seems to be helping in enhancing effective carrier mobility.

JV-response of MEHPPV:CNPPV devices with Al cathode manifests concave (“S” shaped) nature in the fourth quadrant. The FF improves from 12.5% to 30% upon introducing Calcium as the cathode material. Experimentally in spite of a higher V_{OC} of 1.2 V, all active-polymer solar cells based on MEHPPV-CNPPV blend has much lower FF (30%) resulting in a lower PCE as compared to poly[3-hexylthiophene] (P3HT)-[6,6]-phenyl-C61-butyric acid methyl ester (PCBM) (FF \sim 68%). Lower FF stems out from the low mobility in the PPV systems and consequent low exciton dissociation rate. The characteristic “S-shaped” JV-curve is the signature of a counter-injecting diode which arises due to charge accumulation near one of the electrode. Charge carrier accumulation can be a contact-driven process if either there is any thin contamination layer (in form of oxide) present or the metal-polymer interface has void spaces. Two model systems with balanced $\mu\tau$, P3HT-PCBM and MEHPPV-CNPPV, was chosen to investigate the importance of contact-effects to the FF. Bulk material properties of the polymers affect the FF in two ways: (i) accumulation of charge carriers due to unbalanced mobility of electrons and holes and subsequent space charge effect and (ii) the strong field dependence of photocurrent in the third quadrant of the JV-characteristics. The shape of the JV characteristics in the power generating fourth quadrant strongly depends on the quality of polymer cathode interface and does not always bear the fingerprint of bulk material properties. A partial metal coverage or a chemically modified layer can reduce the fill factor drastically in an otherwise efficient solar cell device. The polymer film has a microscopically rough surface, so that the metal does not have uniform contact and there are a vast number of sites forming blind

alleys, which act as electron traps. High electron density over a very sharp edge (\sim nm) gives rise to concentrated electric field which facilitates the injection of holes from the metal (under large reverse bias). This explains the high photocurrent observed in reverse bias regime (third quadrant) in a fast-grown Al-cathode device.

The role of device geometry and size of the active area on the power conversion efficiency has been investigated. Larger the area of the device larger is the resistance of the bottom indium tin oxide (ITO) electrode material. When the short circuit current density becomes high this gives rise to larger power loss in the ITO contact due to the ITO sheet resistance. To avoid the series resistance contribution due to the ITO, it is preferable to keep the device area (which is decided by the overlap area of the top cathode electrode, Aluminum and bottom anode, ITO) smaller. It has been observed that the active-area described by the overlap region of ITO and Al is not the only photoactive region. The measured current in case of flooded illumination is always accompanied with the extra current from the peripheral regions. The origin of this current is partially due to optical effects like beam spreading inside the thick glass substrate and light scattering from the rough interfaces, the other reason being the lateral diffusion of photogenerated charge carriers. Lateral diffusion phenomenon in case of organic semiconductors was firstly observed in our laboratory in pristine polymer systems by local spot illumination outside the overlap region. Same set of experiments were extended to find out lateral diffusion length scales in case of polymer blends and attempts has been made to correlate device performance to the active area related issues in organic solar cells.

The studies of this thesis can further be taken to understand and quantify the photocurrent contribution from the peripheral regions. The transport mechanism and rate of transport can be investigated by studying the temperature dependence

in order to reveal the effect of trap states in the transport. The optical effects can be simulated and quantified using standard simulation tools. These information can be utilized to design a proper grid pattern for solar cells.

Appendix to Chapter 4

Efficient energy transfer from LC to HC has been demonstrated both in blend-film and in solution of the HC (100%)/LC (10%) in chloroform. However the efficiency of energy transfer depends on the phase segregation of HC and LC. Upon addition of controlled amount of cyclohexane (non-solvent for HC polymer alone) the HC chain starts collapsing and give rise to micron sized phase segregated domains. The modulation of phase separation with controlled amount of non-solvent (NS) was useful to study the energy transfer efficiency [179]. At a high concentration of cyclohexane, the fluorescence data revealed the co-collapse of HC and LC. During the collapsing process, LC polymer gets encapsulated within HC. This observation prompted the utilization of cyclohexane in ternary blend devices (HC:LC:CNPPV) in order to study the effect of LC encapsulation within HC. Cyclohexane is a non-solvent for both HC and CNPPV. Polymer solution was prepared by dissolving HC:LC:CNPPV in 2:1:2 weight ratio in chloroform. Controlled amount of cyclohexane (0%, 20%, 40%, 60% by volume fraction) was added to the solution while keeping the concentration of the polymer in the chloroform+cyclohexane mixture same. Devices were prepared by spin coating polymer solutions onto the ITO coated cover slips and by subsequent evaporation of Aluminium cathode.

Wide field photocurrent images and confocal microscopy tools were used to characterize the micro-phase separation in the blends and its effect on

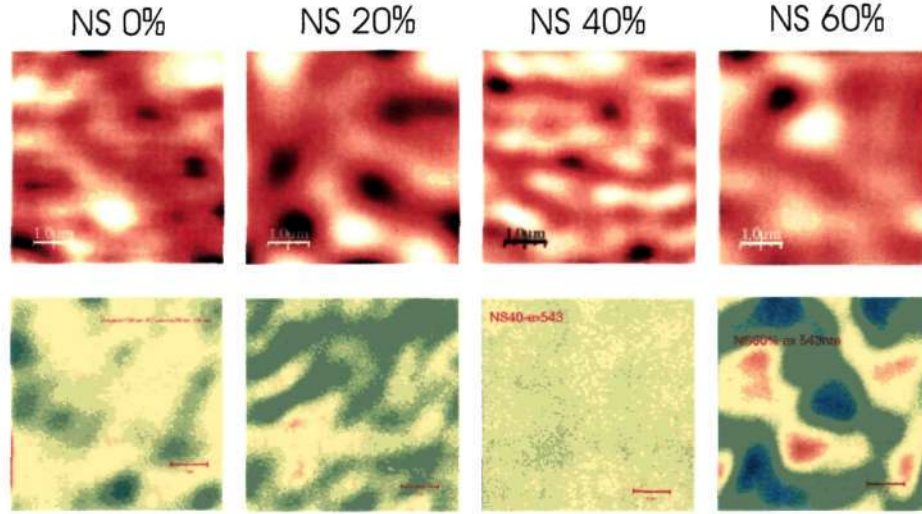


Figure A.1: The photocurrent contrast microscopy images of the devices containing controlled amount of non-solvent (top panel) using 473 nm excitation and $20 \mu\text{m} \times 20 \mu\text{m}$ scan window. Confocal PL images of the ternary blend devices using 543 nm (power ~ 500 nW) excitation and collecting PL emission from 560 nm to 650 nm (bottom panel). The scale bar corresponds to $1 \mu\text{m}$. NS: non-solvent.

NS (in %)	60	40	20	0
I_{ph}	47.60%	57%	34.86%	41.35%
$(I_{\text{ph}})^{\text{max}}$	130 pA	75 pA	13 pA	33 pA
PL	35%	58.23%	43.60%	74.45%

Table A.1: Summary of results obtained from the scanned images on ternary blend devices. I_{ph} indicates fractional area that contributes to the high photocurrent. PL indicates the fractional area where HC PL emission is quenched. $(I_{\text{ph}})^{\text{max}}$ indicates maximum photocurrent magnitude.

photocurrent. Local illumination laser beam revealed highest photocurrent magnitude from the device containing 60% non-solvent concentration. Analysis revealed that the 40% nonsolvent mixed device has most optimum sizeable donor-acceptor homogeneous network through out the film. The confocal local spectroscopic data reveal the quenched PL from HC region. Area histogram analysis for confocal and photocurrent images were found to be correlated, though measurements were carried out on separate samples.

Photocurrent imaging was done on ($20\ \mu\text{m} \times 20\ \mu\text{m}$) area, almost similar phase separation was found throughout the scanned region for smaller scanned window ($5\ \mu\text{m} \times 5\ \mu\text{m}$) of higher resolution. Images were processed using wavelet analysis in WsXm software, in order to improve the resolution (step size = 100 nm, beam spot ~ 400 nm). Although local spot illumination revealed higher photocurrent, a controlled experiment with varying spot size (to replicate broad-band illumination condition) didn't reveal similar trends.

Appendix

A.0.1 Comments on Chapter 3

1. Charge transfer at a polymer/polymer interface, a fundamental issue in this study, depends on the band alignment of the two polymers at the interface. Therefore, it would be helpful if a table listing the energetic values of the HOMO and LUMO levels of ALL polymers used in this study was provided in chapter.

Polymer	HOMO (eV)	LUMO (eV)	Bandgap (eV)
P3HT	4.9	2.7	2.2
PCBM	6.1	3.7	2.4
HC-MEHPPV (100%)	5	2.8	2.2
LC-MEHPPV (10%)	-	-	2.6
CNPPV	5.4	3.2	2.2

Table A.1: Summary of energy levels and bandgap of all the polymers used. The bandgap of the LC-MEHPPV was estimated from the absorption edge near the 370 nm peak.

2. A general comment regarding methodology: details on the PL measurements were not provided in section 3.4.1 despite the section title. This information, mainly the excitation wavelengths used should be clearly indicated in each PL spectra (if different) because this has a major effect on the absorption, energy transfer and emission.

Photoluminescence (PL) measurements on all the HC-MEHPPV and LC-MEHPPV polymers and HC-LC blend films for the present study were done in a Perkin Elmer spectrophotometer with 370 nm excitation unless otherwise stated. The polymer films were coated on quartz substrates and measurements were done in reflection geometry with an excitation wavelength cut-off filter in the emitted light path.

A.0.2 Comments on Chapter 4

1. The PL of HC in Figure 4.2 shows a peak at 600 nm with a broad tail to longer wavelength; while that in Figure 4.4 shows the peak closer to 550 nm. What is the reason for this discrepancy? A different polymer batch? This should be indicated.

Photoluminescence spectra shown in Figure (4.4) of the polymer blend films in different weight ratio using 370 nm excitation. In the blend the PL resembles the feature of HC polymer and the PL of LC phase gets completely quenched. The resultant PL peak of the blend films is slightly blue shifted (575 nm) as compared to pristine HC PL peak (600 nm). This can be attributed to incomplete elimination of the LC-polymer precursor

2. The discussion over PL quenching on Page 83 should include the type of excitation used for the PL measurements. This information is absolutely necessary to follow the arguments of energy transfer. For example: Was the quantum yield of PL measured for both HC and LC using the same excitation wavelength? Is the increase in PL intensity as a function of LC fraction in the HC/LC blends (Figure 4.4) due to the fact that the wavelength used for excitation suits the LC polymer, but not the HC polymer?

PL measurements were done with 370 nm excitation characteristic of LC absorption peak. The quantum efficiency of both the polymers (HC and LC) was

also measured using 370 nm excitation. The enhancement is solely due to energy transfer from LC to HC and the final PL response is characteristic of HC PL response.

3. The similar V_{oc} obtained for all devices is somewhat surprising because it should reflect the "efficient interface for charge separation" which is the HC/CNPPV in two of the blends, but not in the LC/CNPPV. Please comment on this result

Similar V_{oc} (~ 1.1 V) obtained from all the three types of devices, viz. HC:CNPPV, LC:CNPPV and HC:LC:CNPPV blend devices indicates that it is not solely controlled by the LUMO of the acceptor and HOMO of the donor. Al cathode forms a Schottky contact and the work-function difference of cathode and anode also dictates the measured V_{oc} . A thin layer of aluminum oxide formed between metal-polymer interface give rise to charge carrier accumulation near cathode which can also affect V_{oc} .

References

- [1] C. K. Chiang, C. R. Fincher, Y. W. Park, A. J. Heeger, H. Shirakawa, E. J. Louis, S. C. Gau, and A. G. MacDiarmid. Electrical conductivity in doped polyacetylene. *Physical Review Letters*, 39(17):1098–1101, 1977. Cited By (since 1996): 610.
- [2] A. J. Heeger. Semiconducting and metallic polymers: The fourth generation of polymeric materials (nobel lecture). *Angewandte Chemie - International Edition*, 40(14):2591–2611, 2001. Cited By (since 1996): 286.
- [3] A. J. Heeger. Semiconducting and metallic polymers: The fourth generation of polymeric materials. *Synthetic Metals*, 125(1):23–42, 2001. Cited By (since 1996): 39.
- [4] C. W. Tang. Two-layer organic photovoltaic cell. *Applied Physics Letters*, 48(2):183–185, 1986. Cited By (since 1996): 900.
- [5] C. W. Tang and S. A. Vanslyke. Organic electroluminescent diodes. *Applied Physics Letters*, 51(12):913–915, 1987. Cited By (since 1996): 4505.
- [6] J. H. Burroughes, D. D. C. Bradley, A. R. Brown, R. N. Marks, K. Mackay, R. H. Friend, P. L. Burns, and A. B. Holmes. Light-emitting diodes based on conjugated polymers. *Nature*, 347(6293):539–541, 1990. Cited By (since 1996): 5535.
- [7] G. Yu, J. Gao, J. C. Hummelen, F. Wudl, and A. J. Heeger. Polymer photovoltaic cells: Enhanced efficiencies via a network of internal donor-acceptor heterojunctions. *Science*, 270(5243):1789–1791, 1995. Cited By (since 1996): 1566.
- [8] Gilles Horowitz, Denis Fichou, Xuezhou Peng, Zhigang Xu, and Francis Garnier. Field-effect transistor based on conjugated alpha-sexithienyl. *Solid State Communications*, 72(4):381–384, 1989. Cited By (since 1996): 203.
- [9] F. Garnier, G. Horowitz, X. Peng, and D. Fichou. An all-organic “soft” thin film transistor with very high carrier mobility. *Advanced Materials*, 2(12):592–594, 1990. Cited By (since 1996): 226.

- [10] G. Horowitz, X. Peng, D. Fichou, and F. Garnier. The oligothiophene-based field-effect transistor: How it works and how to improve it. *Journal of Applied Physics*, 67(1):528–532, 1990. Cited By (since 1996): 114.
- [11] A. Dodabalapur, Z. Bao, A. Makhija, J. G. Laquindanum, V. R. Raju, Y. Feng, H. E. Katz, and J. Rogers. Organic smart pixels. *Applied Physics Letters*, 73(2):142–144, 1998. Cited By (since 1996): 211.
- [12] H. Sirringhaus, N. Tessler, and R. H. Friend. Integrated optoelectronic devices based on conjugated polymers. *Science*, 280(5370):1741–1744, 1998. Cited By (since 1996): 1049.
- [13] Z. L. Li, S. C. Yang, H. F. Meng, Y. S. Chen, Y. Z. Yang, C. H. Liu, S. F. Horng, C. S. Hsu, L. C. Chen, J. P. Hu, and R. H. Lee. Patterning-free integration of polymer light-emitting diode and polymer transistor. *Applied Physics Letters*, 84(18):3558–3560, 2004.
- [14] G. Yu, K. Pakbaz, and A. J. Heeger. Semiconducting polymer diodes: Large size, low cost photodetectors with excellent visible-ultraviolet sensitivity. *Applied Physics Letters*, 64(25):3422–3424, 1994. Cited By (since 1996): 156.
- [15] G. Yu, J. Wang, J. McElvain, and A. J. Heeger. Large-area, full-color image sensors made with semiconducting polymers. *Advanced Materials*, 10(17):1431–1434, 1998. Cited By (since 1996): 115.
- [16] G. Yu, G. Srdanov, J. Wang, H. Wang, Y. Cao, and A. J. Heeger. Large area, full-color, digital image sensors made with semiconducting polymers. *Synthetic Metals*, 111:133–137, 2000. Cited By (since 1996): 24.
- [17] C. J. Drury, C. M. J. Mutsaers, C. M. Hart, M. Matters, and D. M. De Leeuw. Low-cost all-polymer integrated circuits. *Applied Physics Letters*, 73(1):108–110, 1998. Cited By (since 1996): 468.
- [18] A. Hepp, H. Heil, W. Weise, M. Ahles, R. Schmechel, and H. Von Seggern. Light-emitting field-effect transistor based on a tetracene thin film. *Physical Review Letters*, 91(15):1574061–1574064, 2003. Cited By (since 1996): 111.
- [19] P. F. Baude, D. A. Ender, M. A. Haase, T. W. Kelley, D. V. Muyres, and S. D. Theiss. Pentacene-based radio-frequency identification circuitry. *Applied Physics Letters*, 82(22):3964–3966, 2003. Cited By (since 1996): 210.
- [20] J. Zaumseil, R. H. Friend, and H. Sirringhaus. Spatial control of the recombination zone in an ambipolar light-emitting organic transistor. *Nature Materials*, 5(1):69–74, 2006. Cited By (since 1996): 56.

- [21] S. Steudel, K. Myny, V. Arkhipov, G. Deibel, S. De Vusser, J. Genoe, and P. Heremans. 50 MHz rectifier based on an organic diode. *Nature Materials*, 4(8):597–600, 2005. Cited By (since 1996): 17.
- [22] M. Hamedi, R. Forchheimer, and O. Inganäs. Towards woven logic from organic electronic fibres. *Nature Materials*, 6(5):357–362, 2007. Cited By (since 1996): 4.
- [23] R. E Peierls. *Quantum Theory of Solids*. Clarendon, Oxford, 1955.
- [24] I. H. Campbell, T. W. Hagler, D. L. Smith, and J. P. Ferraris. Direct measurement of conjugated polymer electronic excitation energies using metal/polymer/metal structures. *Physical Review Letters*, 76(11):1900–1903, 1996. Cited By (since 1996): 253.
- [25] Y. Shao and Y. Yang. Efficient organic heterojunction photovoltaic cells based on triplet materials. *Advanced Materials*, 17(23):2841–2844, 2005. Cited By (since 1996): 30.
- [26] N. Ananthakrishnan, G. Padmanaban, S. Ramakrishnan, and J. R. Reynolds. Tuning polymer light-emitting device emission colors in ternary blends composed of conjugated and nonconjugated polymers. *Macromolecules*, 38(18):7660–7669, 2005. Cited By (since 1996): 15.
- [27] J. J. M. Halls, J. Cornil, D. A. dos Santos, R. Silbey, D.-H. Hwang, A. B. Holmes, J. L. Bredas, and R. H. Friend. Charge- and energy-transfer processes at polymer/polymer interfaces: A joint experimental and theoretical study. *Physical Review B - Condensed Matter and Materials Physics*, 60(8):5721–5727, 1999. Cited By (since 1996): 78.
- [28] P. Peumans, A. Yakimov, and S. R. Forrest. Small molecular weight organic thin-film photodetectors and solar cells. *Journal of Applied Physics*, 93(7):3693–3723, 2003. Cited By (since 1996): 422.
- [29] A. C. Morteani, A. S. Dhoot, J.-S. Kim, C. Silva, N. C. Greenham, C. Murphy, E. Moons, S. Cina, J. H. Burroughes, and R. H. Friend. Barrier-free electron-hole capture in polymer blend heterojunction light-emitting diodes. *Advanced Materials*, 15(20):1708–1712, 2003. Cited By (since 1996): 96.
- [30] L. Onsager. Deviations from ohm’s law in weak electrolytes. *The Journal of Chemical Physics*, 2(9):599–615, 1934. Cited By (since 1996): 186.
- [31] L. Onsager. Initial recombination of ions. *Physical Review*, 54(8):554–557, 1938. Cited By (since 1996): 355.

- [32] C. L. Braun. Electric field assisted dissociation of charge transfer states as a mechanism of photocarrier production. *The Journal of Chemical Physics*, 80(9):4157–4161, 1984. Cited By (since 1996): 73.
- [33] C. J. Brabec, G. Zerza, G. Cerullo, S. De Silvestri, S. Luzzati, J. C. Hummelen, and S. Sariciftci. Tracing photoinduced electron transfer process in conjugated polymer/fullerene bulk heterojunctions in real time. *Chemical Physics Letters*, 340(3-4):232–236, 2001. Cited By (since 1996): 154.
- [34] V. D. Mihailetschi, L. J. A. Koster, J. C. Hummelen, and P. W. M. Blom. Photocurrent generation in polymer-fullerene bulk heterojunctions. *Physical Review Letters*, 93(21):216601–1–216601–4, 2004. Cited By (since 1996): 67.
- [35] A. C. Morteani, P. Sreearunothai, L. M. Herz, R. H. Friend, and C. Silva. Exciton regeneration at polymeric semiconductor heterojunctions. *Physical Review Letters*, 92(24):247402–1, 2004. Cited By (since 1996): 61.
- [36] A. C. Morteani, R. H. Friend, and C. Silva. Endothermic exciplex-exciton energy-transfer in a blue-emitting polymeric heterojunction system. *Chemical Physics Letters*, 391(1-3):81–84, 2004. Cited By (since 1996): 10.
- [37] H. J. Snaith, A. C. Arias, A. C. Morteani, C. Silva, and R. H. Friend. Charge generation kinetics and transport mechanisms in blended polyfluorene photovoltaic devices. *Nano Letters*, 2(12):1353–1357, 2002. Cited By (since 1996): 75.
- [38] C. R. McNeill, S. Westenhoff, C. Groves, R. H. Friend, and N. C. Greenham. Influence of nanoscale phase separation on the charge generation dynamics and photovoltaic performance of conjugated polymer blends: Balancing charge generation and separation. *Journal of Physical Chemistry C*, 111(51):19153–19160, 2007.
- [39] T. Granlund, L. A. A. Pettersson, M. R. Anderson, and O. Inganäs. Interference phenomenon determines the color in an organic light emitting diode. *Journal of Applied Physics*, 81(12):8097–8104, 1997. Cited By (since 1996): 52.
- [40] D. D. Gebler, Y. Z. Wang, D.-K. Fu, T. M. Swager, and A. J. Epstein. Exciplex emission from bilayers of poly(vinylcarbazole) and pyridine based conjugated copolymers. *Journal of Chemical Physics*, 108(18):7842–7848, 1998. Cited By (since 1996): 43.
- [41] N. F. Mott and E. A. Davis. *Electronic processes in Non-crystalline Materials*. (Oxford:Clarendon Press) 2nd Ed., 1979.

- [42] A. Miller and E. Abrahams. Impurity conduction at low concentrations. *Physical Review*, 120(3):745–755, 1960. Cited By (since 1996): 369.
- [43] H. Scher and E. W. Montroll. Anomalous transit-time dispersion in amorphous solids. *Physical Review B*, 12(6):2455–2477, 1975. Cited By (since 1996): 585.
- [44] M. E. Scharfe. Transient photoconductivity in vitreous As_2Se_3 . *Physical Review B*, 2(12):5025–5034, 1970. Cited By (since 1996): 12.
- [45] D. M. Pai and M. E. Scharfe. Charge transport in films of amorphous Arsenic Triselenide. *Journal of Non-Crystalline Solids*, 8-10:752–759, 1972. Cited By (since 1996): 2.
- [46] G. Pfister and C. H. Griffiths. Temperature dependence of transient hole hopping transport in disordered organic solids: Carbazole polymers. *Physical Review Letters*, 40(10):659–662, 1978. Cited By (since 1996): 20.
- [47] P. M. Borsenberger, L. T. Pautmeier, and H. Bässler. Nondispersive-to-dispersive charge-transport transition in disordered molecular solids. *Physical Review B*, 46(19):12145–12153, 1992. Cited By (since 1996): 55.
- [48] H. J. Yuh and M. Stolka. Origin of dispersion of transiting charge carriers in molecularly doped polymers. *Philosophical Magazine B: Physics of Condensed Matter; Electronic, Optical and Magnetic Properties*, 58(5):539–549, 1988. Cited By (since 1996): 14.
- [49] L. B. Schein, J. C. Scott, L. T. Pautmeier, and R. H. Young. Anomalous charge transport in molecularly doped polymers. *Molecular Crystals and Liquid Crystals*, 228(1):175–184, 1993.
- [50] P. M. Borsenberger, L. T. Pautmeier, and H. Bässler. Scaling behavior of nondispersive charge transport in disordered molecular solids. *Physical Review B*, 48(5):3066–3073, 1993. Cited By (since 1996): 37.
- [51] M. Van Der Auweraer, F. C. De Schryver, P. M. Borsenberger, and H. Bässler. Disorder in charge transport in doped polymers. *Advanced Materials*, 6(3):199–213, 1994. Cited By (since 1996): 75.
- [52] H Bässler. Charge transport in disordered organic photoconductors: A monte carlo simulation study. *Physica Status Solidi (b)*, 175(15):15–56, 1993.
- [53] S. D. Baranovskii, H. Cordes, F. Hensel, and G. Leising. Charge-carrier transport in disordered organic solids. *Physical Review B*, 62(12):7934, 2000.
- [54] D. Hertel and H. Bassler. Photoconduction in amorphous organic solids. *ChemPhysChem*, 9(5):666–688, 2008. Cited By (since 1996): 1.

- [55] N. Rappaport, Y. Bar, O. Solomeshch, and N. Tessler. Mobility spatial distribution function: Comparative method for conjugated polymers/molecules. *Applied Physics Letters*, 89(25):252117, 2006.
- [56] D. Monroe. Hopping in exponential band tails. *Physical Review Letters*, 54(2):146–149, 1985. Cited By (since 1996): 131.
- [57] S. D Baranovskii, P Thomas, and G. J Adriaenssens. The concept of transport energy and its application to steady-state photoconductivity in amorphous silicon. *Journal of Non-Crystalline Solids*, 190:283–287, 1995.
- [58] D. M. Pai. Transient photoconductivity in poly(N-vinylcarbazole). *Journal of Chemical Physics*, 52(5):2285–2291, 1970. Cited By (since 1996): 105.
- [59] J. Frenkel. On pre-breakdown phenomena in insulators and electronic semiconductors. *Physical Review*, 54(8):647–648, 1938. Cited By (since 1996): 337.
- [60] W. D. Gill. Drift mobilities in amorphous charge-transfer complexes of trinitrofluorenone and poly-N-vinylcarbazole. *Journal of Applied Physics*, 43(12):5033–5040, 1972. Cited By (since 1996): 359.
- [61] W. F. Pasveer, J. Cottaar, C. Tanase, R. Coehoorn, P. A. Bobbert, P. W. M. Blom, M. De Leeuw, and M. A. J. Michels. Unified description of charge-carrier mobilities in disordered semiconducting polymers. *Physical Review Letters*, 94(20):1–4, 2005. Cited By (since 1996): 5.
- [62] C. Tanase, P. W. M. Blom, and D. M. De Leeuw. Origin of the enhanced space-charge-limited current in poly(p-phenylene vinylene). *Physical Review B - Condensed Matter and Materials Physics*, 70(19):1–4, 2004. Cited By (since 1996): 1.
- [63] C. Tanase, J. Wildeman, P. W. M. Blom, M. E. M. Benito, D. M. De Leeuw, A. J. J. M. Van Breemen, P. T. Herwig, C. H. T. Chlon, J. Sweelssen, and H. F. M. Schoo. Optimization of the charge transport in poly(phenylene vinylene) derivatives by processing and chemical modification. *Journal of Applied Physics*, 97(12):1–6, 2005. Cited By (since 1996): 3.
- [64] C. Tanase, P. W. M. Blom, D. M. De Leeuw, and E. J. Meijer. Charge carrier density dependence of the hole mobility in poly(p-phenylene vinylene). *Physica Status Solidi (A) Applied Research*, 201(6):1236–1245, 2004. Cited By (since 1996): 25.
- [65] P. Langevin. *Ann. Chim. Phys.*, 28:433, 1903.

- [66] D. R. Bates. Ionic recombination in a high density ambient gas. *Journal of Physics B: Atomic and Molecular Physics*, 8(16):2722–2727, 1975. Cited By (since 1996): 1.
- [67] K. G. Emeleus and J. R. M. Coulter. Recombination of positive and negative ions in a dense gas. *International Journal of Electronics*, 67(2):257–260, 1989.
- [68] G. Sommer N. Karl. Field dependent losses of electrons and holes by bimolecular volume recombination in the excitation layer of anthracene single crystals studied by drift current pulses. *Physica Status Solidi (a)*, 6(1):231–241, 1971.
- [69] G Juska, M Viliunas, O Klima, E Sipek, and J Kocka. New features in space-charge-limited photocurrent transients. *Philosophical Magazine B*, 69(2):277–289, 1994.
- [70] G. Juka, M. Viliunas, K. Arlauskas, and J. Kocka. Space-charge-limited photocurrent transients: The influence of bimolecular recombination. *Physical Review B*, 51(23):16668–16676, 1995. Cited By (since 1996): 17.
- [71] J. Kocka, O. Klima, G. Juska, M. Hoheisel, and R. Plattner. SCLC transients in a-Si:H. new features and possibilities. *Journal of Non-Crystalline Solids*, 137-38(pt 1):427–430, 1991. Cited By (since 1996): 7.
- [72] A. Pivrikas, G. Juska, A. J. Mozer, M. Scharber, K. Arlauskas, N. S. Sariciftci, H. Stubb, and R. Osterbacka. Bimolecular recombination coefficient as a sensitive testing parameter for low-mobility solar-cell materials. *Physical Review Letters*, 94(17):1–4, 2005. Cited By (since 1996): 3.
- [73] A. Pivrikas, G. Juska, R. Osterbacka, M. Westerling, M. Viliunas, K. Arlauskas, and H. Stubb. Langevin recombination and space-charge-perturbed current transients in regiorandom poly(3-hexylthiophene). *Physical Review B - Condensed Matter and Materials Physics*, 71(12):1–5, 2005. Cited By (since 1996): 2.
- [74] F. Laquai, G. Wegner, C. Im, H. Bässler, and S. Heun. Nondispersive hole transport in carbazole- and anthracene-containing polyspirobifluorene copolymers studied by the charge-generation layer time-of-flight technique. *Journal of Applied Physics*, 99(3):033710, 2006.
- [75] F. Laquai, G. Wegner, C. Im, H. Bässler, and S. Heun. Comparative study of hole transport in polyspirobifluorene polymers measured by the charge-generation layer time-of-flight technique. *Journal of Applied Physics*, 99(2):1–7, 2006. Cited By (since 1996): 1.

- [76] P. M. Borsenberger, L. Pautmeier, and H. Bässler. Hole transport in bis(4-N,N-diethylamino-2-methylphenyl)-4-methylphenylmethane. *The Journal of Chemical Physics*, 95(2):1258–1265, 1991. Cited By (since 1996): 28.
- [77] N. Rappaport, O. Solomesch, and N. Tessler. The mobility spatial distribution function: Turn-on dynamics of polymer photocells. *Journal of Applied Physics*, 99(6):064507, 2006.
- [78] J. S. Wilson, A. S. Dhoot, A. J. A. B. Seeley, M. S. Khan, A. Kohler, and R. H. Friend. Spin-dependent exciton formation in π -conjugated compounds. *Nature*, 413(6858):828–831, 2001. Cited By (since 1996): 206.
- [79] P. W. M. Blom, M. J. M. De Jong, and J. J. M. Vleggaar. Electron and hole transport in poly(p-phenylene vinylene) devices. *Applied Physics Letters*, 68(23):3308–3310, 1996. Cited By (since 1996): 308.
- [80] H. C. F. Martens, W. F. Pasveer, H. B. Brom, J. N. Huiberts, and P. W. M. Blom. Crossover from space-charge-limited to recombination-limited transport in polymer light-emitting diodes. *Physical Review B - Condensed Matter and Materials Physics*, 63(12):1253281–1253287, 2001. Cited By (since 1996): 31.
- [81] D. Poplavskyy and J. Nelson. Nondispersive hole transport in amorphous films of methoxy-spirofluorene-arylamine organic compound. *Journal of Applied Physics*, 93(1):341–346, 2003. Cited By (since 1996): 50.
- [82] G. Juska, K. Genevicius, G. Sliuzys, A. Pivrikas, M. Scharber, and R. Österbacka. Double-injection current transients as a way of measuring transport in insulating organic films. *Journal of Applied Physics*, 101(11), 2007. Cited By (since 1996): 1.
- [83] N. S. Sariciftci, L. Smilowitz, A. J. Heeger, and F. Wudl. Photoinduced electron transfer from a conducting polymer to buckminsterfullerene. *Science*, 258(5087):1474–1476, 1992. Cited By (since 1996): 1193.
- [84] S. E. Shaheen, C. J. Brabec, N. S. Sariciftci, F. Padinger, T. Fromherz, and J. C. Hummelen. 2.5% efficient organic plastic solar cells. *Applied Physics Letters*, 78(6):841–843, 2001. Cited By (since 1996): 866.
- [85] C. J. Brabec, S. E. Shaheen, C. Winder, N. Serdar Sariciftci, and P. Denk. Effect of LiF/metal electrodes on the performance of plastic solar cells. *Applied Physics Letters*, 80(7):1288, 2002. Cited By (since 1996): 194.
- [86] J. J. M. Halls, C. A. Walsh, N. C. Greenham, E. A. Marseglla, R. H. Friend, S. C. Moratti, and A. B. Holmes. Efficient photodiodes from interpenetrating

- polymer networks. *Nature*, 376(6540):498–500, 1995. Cited By (since 1996): 997.
- [87] M. M. Koetse, J. Sweelssen, K. T. Hoekerd, H. F. M. Schoo, S. C. Veenstra, J. M. Kroon, X. Yang, and J. Loos. Efficient polymer: Polymer bulk heterojunction solar cells. *Applied Physics Letters*, 88(8), 2006. Cited By (since 1996): 2.
- [88] S. C. Veenstra, W. J. H. Verhees, J. M. Kroon, M. M. Koetse, J. Sweelssen, J. J. A. M. Bastiaansen, H. F. M. Schoo, X. Yang, A. Alexeev, J. Loos, U. S. Schubert, and M. M. Wienk. Photovoltaic properties of a conjugated polymer blend of mdmo-ppv and pcnepv. *Chemistry of Materials*, 16(12):2503–2508, 2004. Cited By (since 1996): 43.
- [89] C. R. McNeill, A. Abrusci, J. Zaumseil, R. Wilson, M. J. McKiernan, J. H. Burroughes, J. J. M. Halls, N. C. Greenham, and R. H. Friend. Dual electron donor/electron acceptor character of a conjugated polymer in efficient photovoltaic diodes. *Applied Physics Letters*, 90(19), 2007. Cited By (since 1996): 1.
- [90] N. C. Greenham, X. Peng, and A. P. Alivisatos. Charge separation and transport in conjugated-polymer/semiconductor-nanocrystal composites studied by photoluminescence quenching and photoconductivity. *Physical Review B - Condensed Matter and Materials Physics*, 54(24):17628–17637, 1996. Cited By (since 1996): 437.
- [91] W. U. Huynh, J. J. Dittmer, and A. P. Alivisatos. Hybrid nanorod-polymer solar cells. *Science*, 295(5564):2425–2427, 2002. Cited By (since 1996): 1044.
- [92] B. Sun, H. J. Snaith, A. S. Dhoot, S. Westenhoff, and N. C. Greenham. Vertically segregated hybrid blends for photovoltaic devices with improved efficiency. *Journal of Applied Physics*, 97(1), 2005. Cited By (since 1996): 43.
- [93] W. J. E. Beek, M. M. Wienk, and R. A. J. Janssen. Efficient hybrid solar cells from zinc oxide nanoparticles and a conjugated polymer. *Advanced Materials*, 16(12):1009–1013, 2004. Cited By (since 1996): 121.
- [94] A. C. Arango, S. A. Carter, and P. J. Brock. Charge transfer in photovoltaics consisting of interpenetrating networks of conjugated polymer and TiO₂ nanoparticles. *Applied Physics Letters*, 74(12):1698–1700, 1999. Cited By (since 1996): 128.
- [95] J. Peet, J. Y. Kim, N. E. Coates, W. L. Ma, D. Moses, A. J. Heeger, and G. C. Bazan. Efficiency enhancement in low-bandgap polymer solar cells by

- processing with alkane dithiols. *Nature Materials*, 6(7):497–500, 2007. Cited By (since 1996): 22.
- [96] S. E. Shaheen, D. Vangeneugden, R. Kiebooms, D. Vanderzande, T. Fromherz, F. Padinger, C. J. Brabec, and N. S. Sariciftci. Low band-gap polymeric photovoltaic devices. *Synthetic Metals*, 121(1-3):1583–1584, 2001. Cited By (since 1996): 30.
- [97] D. Mühlbacher, M. Scharber, M. Morana, Z. Zhu, D. Waller, R. Gaudiana, and C. Brabec. High photovoltaic performance of a low-bandgap polymer. *Advanced Materials*, 18(21):2884–2889, 2006. Cited By (since 1996): 43.
- [98] W. Ma, C. Yang, X. Gong, K. Lee, and A. J. Heeger. Thermally stable, efficient polymer solar cells with nanoscale control of the interpenetrating network morphology. *Advanced Functional Materials*, 15(10):1617–1622, 2005. Cited By (since 1996): 362.
- [99] G. Li, V. Shrotriya, J. Huang, Y. Yao, T. Moriarty, K. Emery, and Y. Yang. High-efficiency solution processable polymer photovoltaic cells by self-organization of polymer blends. *Nature Materials*, 4(11):864–868, 2005. Cited By (since 1996): 339.
- [100] M. Reyes-Reyes, K. Kim, J. Dewald, R. Lopez-Sandoval, A. Avadhanula, S. Curran, and D. L. Carroll. Meso-structure formation for enhanced organic photovoltaic cells. *Organic Letters*, 7(26):5749–5752, 2005. Cited By (since 1996): 60.
- [101] A. C. Mayer, Scully, B. E. S. R. Hardin, M. W. Rowell, and M. D. McGehee. Polymer-based solar cells. *Materials Today*, 10(11):28–23, 2007.
- [102] M. Reyes-Reyes, K. Kim, and D. L. Carroll. High-efficiency photovoltaic devices based on annealed poly(3-hexylthiophene) and 1-(3-methoxycarbonyl)propyl-1-phenyl-(6,6)c₆₁ blends. *Applied Physics Letters*, 87(8):1–3, 2005. Cited By (since 1996): 16.
- [103] M. Campoy-Quiles, T. Ferenczi, T. Agostinelli, P. G. Etchegoin, Y. Kim, T. D. Anthopoulos, P. N. Stavrinou, D. D. C. Bradley, and J. Nelson. Morphology evolution via self-organization and lateral and vertical diffusion in polymer:fullerene solar cell blends. *Nature Materials*, 7(2):158–164, 2008. Cited By (since 1996): 1.
- [104] E. Bundgaard and F. C. Krebs. Low band gap polymers for organic photovoltaics. *Solar Energy Materials and Solar Cells*, 91(11):954–985, 2007. Cited By (since 1996): 27.

- [105] E. Menard, M. A. Meitl, Y. Sun, J.-U. Park, D. J.-L. Shir, Y.-S. Nam, S. Jeon, and J. A. Rogers. Micro- and nanopatterning techniques for organic electronic and optoelectronic systems. *Chemical Reviews*, 107(4):1117–1160, 2007. Cited By (since 1996): 16.
- [106] K. M. Coakley, Y. Liu, C. Goh, and M. D. McGehee. Ordered organic-inorganic bulk heterojunction photovoltaic cells. *MRS Bulletin*, 30(1):37–40, 2005. Cited By (since 1996): 32.
- [107] Z. Zhu, D. Waller, R. Gaudiana, M. Morana, D. Mühlbacher, M. Scharber, and C. Brabec. Panchromatic conjugated polymers containing alternating donor/ acceptor units for photovoltaic applications. *Macromolecules*, 40(6):1981–1986, 2007. Cited By (since 1996): 3.
- [108] I.W. Hwang, C. Soci, D. Moses, Z. Zhu, D. Waller, R. Gaudiana, C. J. Brabec, and A. J. Heeger. Ultrafast electron transfer and decay dynamics in a small band gap bulk heterojunction material. *Advanced Materials*, 19(17):2307–2312, 2007. Cited By (since 1996): 3.
- [109] D. Mühlbacher, M. Scharber, M. Morana, Z. Zhu, D. Waller, R. Gaudiana, and C. Brabec. High photovoltaic performance of a low-bandgap polymer. *Advanced Materials*, 18(21):2884–2889, 2006. Cited By (since 1996): 43.
- [110] K. Lee, J. Y. Kim, S. H. Park, S. H. Kim, S. Cho, and A. J. Heeger. Air-stable polymer electronic devices. *Advanced Materials*, 19(18):2445–2449, 2007. Cited By (since 1996): 2.
- [111] J. Peet, J. Y. Kim, N. E. Coates, W. L. Ma, D. Moses, A. J. Heeger, and G. C. Bazan. Efficiency enhancement in low-bandgap polymer solar cells by processing with alkane dithiols. *Nature Materials*, 6(7):497–500, 2007. Cited By (since 1996): 25.
- [112] Y. K. Jin, K. Lee, N. E. Coates, D. Moses, T.-Q. Nguyen, M. Dante, and A. J. Heeger. Efficient tandem polymer solar cells fabricated by all-solution processing. *Science*, 317(5835):222–225, 2007. Cited By (since 1996): 8.
- [113] K. M. Coakley and M. D. McGehee. Photovoltaic cells made from conjugated polymers infiltrated into mesoporous titania. *Applied Physics Letters*, 83(16):3380–3382, 2003. Cited By (since 1996): 112.
- [114] V. Gowrishankar, N. Miller, M. D. McGehee, M. J. Misner, D. Y. Ryu, T. P. Russell, E. Drockenmuller, and C. J. Hawker. Fabrication of densely packed, well-ordered, high-aspect-ratio silicon nanopillars over large areas using block copolymer lithography. *Thin Solid Films*, 513(1-2):289–294, 2006. Cited By (since 1996): 9.

- [115] G. K. Mor, O. K. Varghese, M. Paulose, K. Shankar, and C. A. Grimes. A review on highly ordered, vertically oriented TiO_2 nanotube arrays: Fabrication, material properties, and solar energy applications. *Solar Energy Materials and Solar Cells*, 90(14):2011–2075, 2006. Cited By (since 1996): 62.
- [116] P. Ravirajan, A. M. Peiro, M. K. Nazeeruddin, M. Graetzel, D. D. C. Bradley, J. R. Durrant, and J. Nelson. Hybrid polymer/zinc oxide photovoltaic devices with vertically oriented ZnO nanorods and an amphiphilic molecular interface layer. *Journal of Physical Chemistry B*, 110(15):7635–7639, 2006. Cited By (since 1996): 44.
- [117] J. Y. Kim, S. H. Kim, H.-H. Lee, K. Lee, W. Ma, X. Gong, and A. J. Heeger. New architecture for high-efficiency polymer photovoltaic cells using solution-based titanium oxide as an optical spacer. *Advanced Materials*, 18(5):572–576, 2006. Cited By (since 1996): 80.
- [118] K. Lee, J. Y. Kim, S. H. Park, S. H. Kim, S. Cho, and A. J. Heeger. Air-stable polymer electronic devices. *Advanced Materials*, 19(18):2445–2449, 2007. Cited By (since 1996): 2.
- [119] G. Dennler, K. Forberich, T. Ameri, C. Waldauf, P. Denk, C. J. Brabec, K. Hingerl, and A. J. Heeger. Design of efficient organic tandem cells: On the interplay between molecular absorption and layer sequence. *Journal of Applied Physics*, 102(12), 2007.
- [120] P. W. M. Blom, V. D. Mihailechi, L. J. A. Koster, and D. E. Markov. Device physics of polymer:fullerene bulk heterojunction solar cells. *Advanced Materials*, 19(12):1551–1566, 2007. Cited By (since 1996): 14.
- [121] P.E. Shaw, A. Ruseckas, and I.D.W. Samuel. Exciton diffusion measurements in poly(3-hexylthiophene). *Advanced Materials*, 10.1002/adma.200800982, 2008.
- [122] V. D. Mihailechi, J. K. J. Van Duren, P. W. M. Blom, J. C. Hummelen, R. A. J. Janssen, J. M. Kroon, M. T. Rispens, W. J. H. Verhees, and M. M. Wienk. Electron transport in a methanofullerene. *Advanced Functional Materials*, 13(1):43–46, 2003. Cited By (since 1996): 99.
- [123] P. W. M. Blom, M. J. M. De Jong, and M. G. Van Munster. Electric-field and temperature dependence of the hole mobility in poly(p-phenylene vinylene). *Physical Review B - Condensed Matter and Materials Physics*, 55(2):R656–R659, 1997. Cited By (since 1996): 232.
- [124] W. Geens, S. E. Shaheen, C. J. Brabec, J. Poortmans, and N. Serdar Sariciftci. Field-effect mobility measurements of conjugated polymer/fullerene photovoltaic blends. volume 544, pages 516–520, 2000.

- [125] C. Tanase, E. J. Meijer, P. W. M. Blom, and D. M. De Leeuw. Unification of the hole transport in polymeric field-effect transistors and light-emitting diodes. *Physical Review Letters*, 91(21):216601/1–216601/4, 2003. Cited By (since 1996): 114.
- [126] S. A. Choulis, J. Nelson, Y. Kim, D. Poplavskyy, T. Kreouzis, J. R. Durrant, and D. D. C. Bradley. Investigation of transport properties in polymer/fullerene blends using time-of-flight photocurrent measurements. *Applied Physics Letters*, 83(18):3812–3814, 2003. Cited By (since 1996): 54.
- [127] R. Pacios, J. Nelson, D. D. C. Bradley, and C. J. Brabec. Composition dependence of electron and hole transport in polyfluorene:[6,6]-phenyl c_{61} -butyric acid methyl ester blend films. *Applied Physics Letters*, 83(23):4764–4766, 2003. Cited By (since 1996): 28.
- [128] C. Melzer, E. J. Koop, V. D. Mihailetschi, and P. W. M. Blom. Hole transport in poly(phenylene vinylene)/methanofullerene bulk-heterojunction solar cells. *Advanced Functional Materials*, 14(9):865–870, 2004. Cited By (since 1996): 69.
- [129] V. D. Mihailetschi, L. J. A. Koster, P. W. M. Blom, C. Melzer, B. De Boer, J. K. J. Van Duren, and R. A. J. Janssen. Compositional dependence of the performance of poly(p-phenylene vinylene):methanofullerene bulk-heterojunction solar cells. *Advanced Functional Materials*, 15(5):795–801, 2005. Cited By (since 1996): 55.
- [130] V. D. Mihailetschi, P. W. M. Blom, J. C. Hummelen, and M. T. Rispens. Cathode dependence of the open-circuit voltage of polymer:fullerene bulk heterojunction solar cells. *Journal of Applied Physics*, 94(10):6849–6854, 2003. Cited By (since 1996): 98.
- [131] H. Frohne, S. E. Shaheen, C. J. Brabec, D. C. Muller, N. S. Sariciftci, and K. Meerholz. Influence of the anodic work function on the performance of organic solar cells. *ChemPhysChem*, 3(9):795–799, 2002. Cited By (since 1996): 43.
- [132] C. J. Brabec, A. Cravino, D. Meissner, N. Serdar Sariciftci, T. Fromherz, M. T. Rispens, L. Sanchez, and J. C. Hummelen. Origin of the open circuit voltage of plastic solar cells. *Advanced Functional Materials*, 11(5):374–380, 2001. Cited By (since 1996): 239.
- [133] R. Richert, L. Pautmeier, and H. Bässler. Diffusion and drift of charge carriers in a random potential: Deviation from einsteins law. *Physical Review Letters*, 63(5):547–550, 1989. Cited By (since 1996): 38.

- [134] Y. Preezant, Y. Roichman, and N. Tessler. Amorphous organic devices - degenerate semiconductors. *Journal of Physics Condensed Matter*, 14(42):9913–9924, 2002. Cited By (since 1996): 5.
- [135] Y. Roichman and N. Tessler. Generalized einstein relation for disordered semiconductors-implications for device performance. *Applied Physics Letters*, 80(11):1948, 2002. Cited By (since 1996): 51.
- [136] Y. Roichman and N. Tessler. Charge transport in conjugated polymers - the influence of charge concentration. *Synthetic Metals*, 135-136:443–444, 2003. Cited By (since 1996): 14.
- [137] J. A. Barker, C. M. Ramsdale, and N. C. Greenham. Modeling the current-voltage characteristics of bilayer polymer photovoltaic devices. *Physical Review B - Condensed Matter and Materials Physics*, 67(7):752051–752059, 2003. Cited By (since 1996): 55.
- [138] L. J. A. Koster, E. C. P. Smits, V. D. Mihailetschi, and P. W. M. Blom. Device model for the operation of polymer/fullerene bulk heterojunction solar cells. *Physical Review B - Condensed Matter and Materials Physics*, 72(8):1–9, 2005. Cited By (since 1996): 8.
- [139] H. J. Snaith, I. B. Malone, M. R. Catherine, R. H. Friend, and N. C. Greenham. Charge transport and efficiency in photovoltaic devices based on polyfluorene blends. *Proceedings of SPIE*, 5520:26–35, 2004.
- [140] V. D. Mihailetschi, J. Wildeman, and P. W. M. Blom. Space-charge limited photocurrent. *Physical Review Letters*, 94(12):1–4, 2005. Cited By (since 1996): 5.
- [141] A. M. Goodman and A. Rose. Double extraction of uniformly generated electron-hole pairs from insulators with noninjecting contacts. *Journal of Applied Physics*, 42(7):2823–2830, 1971. Cited By (since 1996): 33.
- [142] N. Tessler and N. Rappaport. Excitation density dependence of photocurrent efficiency in low mobility semiconductors. *Journal of Applied Physics*, 96(2):1083–1087, 2004. Cited By (since 1996): 6.
- [143] N. Rappaport, O. Solomesch, and N. Tessler. The interplay between space charge and recombination in conjugated polymer/molecule photocells. *Journal of Applied Physics*, 98(3):1–4, 2005. Cited By (since 1996): 1.
- [144] L. J. A. Koster, V. D. Mihailetschi, and P. W. M. Blom. Bimolecular recombination in polymer/fullerene bulk heterojunction solar cells. *Applied Physics Letters*, 88(5):1–3, 2006. Cited By (since 1996): 3.

- [145] M. M. Mandoc, L. J. A. Koster, and P. W. M. Blom. Optimum charge carrier mobility in organic solar cells. *Applied Physics Letters*, 90(13):133504, 2007.
- [146] K. Y. Jen, R. Oboodi, and R. L. Elsenbaumer. Processible and environmentally stable conducting polymer. 1985.
- [147] R. D. McCullough. The chemistry of conducting polythiophenes. *Advanced Materials*, 10(2):93–116, 1998. Cited By (since 1996): 456.
- [148] V. Bhatia, D. Gupta, D. Kabra, and K.S. Narayan. Optical and electrical features of surface ordered regioregular polyhexylthiophene. *Journal of Material Science: Material Electronics*, 18:925–930, 2007.
- [149] T. A. Chen, X. Wu, and R. D. Rieke. Regiocontrolled synthesis of poly(3-alkylthiophenes) mediated by rieke zinc: Their characterization and solid-state properties. *Journal of the American Chemical Society*, 117(1):233–244, 1995. Cited By (since 1996): 587.
- [150] J. K. Herrema, J. Wildeman, F. van Bolhuis, and G. Hadziioannou. Synthesis and crystal structures of two dialkyl-substituted sexithiophenes. *Synthetic Metals*, 60(3):239–248, 1993. Cited By (since 1996): 50.
- [151] H. Mao, B. Xu, and S. Holdcroft. Synthesis and structure-property relationships of regiorregular poly(3-hexylthiophenes). *Macromolecules*, 26(5):1163–1169, 1993. Cited By (since 1996): 64.
- [152] A. Stabel and J. P. Rabe. Scanning tunnelling microscopy of alkylated oligothiophenes at interfaces with graphite. *Synthetic Metals*, 67(1-3):47–53, 1994. Cited By (since 1996): 37.
- [153] T. J. Prosa, M. J. Winokur, J. Moulton, P. Smith, and A. J. Heeger. X-ray structural studies of poly(3-alkylthiophenes): An example of an inverse comb. *Macromolecules*, 25(17):4364–4372, 1992. Cited By (since 1996): 150.
- [154] Y. Kim, S. Cook, S. M. Tuladhar, S. A. Choulis, J. Nelson, J. R. Durrant, D. D. C. Bradley, M. Giles, I. McCulloch, C. . Ha, and M. Ree. A strong regioregularity effect in self-organizing conjugated polymer films and high-efficiency polythiophene:fullerene solar cells. *Nature Materials*, 5(3):197–203, 2006. Cited By (since 1996): 133.
- [155] P. Schilinsky, U. Asawapirom, U. Scherf, M. Biele, and C. J. Brabec. Influence of the molecular weight of poly(3-hexylthiophene) on the performance of bulk heterojunction solar cells. *Chemistry of Materials*, 17(8):2175–2180, 2005. Cited By (since 1996): 50.

- [156] G. Padmanaban, K. Nagesh, and S. Ramakrishnan. Segmented poly[2-methoxy-5-(2-ethylhexyloxy)-1,4-phenylene vinylene] via xanthate and dithiocarbamate precursors: A comparative study of thermal eliminations. *Journal of Polymer Science, Part A: Polymer Chemistry*, 41(24):3929–3940, 2003. Cited By (since 1996): 8.
- [157] G. Padmanaban and S. Ramakrishnan. Conjugation length control in soluble poly[2-methoxy-5-((2'-ethylhexyl) oxy)-1,4-phenylenevinylene] (MEHPPV): Synthesis, optical properties, and energy transfer. *Journal of the American Chemical Society*, 122(10):2244–2251, 2000. Cited By (since 1996): 81.
- [158] F. Wudl. Fullerene materials. *Journal of Materials Chemistry*, 12(7):1959–1963, 2002. Cited By (since 1996): 68.
- [159] Shigenori Morita, Anvar A. Zakhidov, and Katsumi Yoshino. Doping effect of buckminsterfullerene in conducting polymer. change of absorption spectrum and quenching of luminescence. *Solid State Communications*, 82(4):249–252, 1992. Cited By (since 1996): 218.
- [160] N. S. Sariciftci, D. Braun, C. Zhang, V. I. Srdanov, A. J. Heeger, G. Stucky, and F. Wudl. Semiconducting polymer-buckminsterfullerene heterojunctions: Diodes, photodiodes, and photovoltaic cells. *Applied Physics Letters*, 62(6):585–587, 1993. Cited By (since 1996): 388.
- [161] J. C. Hummelen, B. W. Knight, F. Lepeq, F. Wudl, J. Yao, and C. L. Wilkins. Preparation and characterization of fulleroid and methanofullerene derivatives. *Journal of Organic Chemistry*, 60(3):532–538, 1995. Cited By (since 1996): 264.
- [162] R. A. J. Janssen, J. C. Hummelen, K. Lee, K. Pakbaz, N. Serdar Sariciftci, A. J. Heeger, and F. Wudl. Photoinduced electron transfer from π -conjugated polymers onto buckminsterfullerene, fulleroids, and methanofullerenes. *The Journal of Chemical Physics*, 103(2):788–793, 1995. Cited By (since 1996): 40.
- [163] L. Groenendaal, F. Jonas, D. Freitag, H. Pielartzik, and J. R. Reynolds. Poly(3,4-ethylenedioxythiophene) and its derivatives: past, present, and future. *Advanced Materials*, 12(7):481–494, 2000. Cited By (since 1996): 717.
- [164] F. Louwet, L. Groenendaal, J. Dhaen, J. Manca, J. Van Luppen, E. Verdonck, and L. Leenders. PEDOT/PSS: Synthesis, characterization, properties and applications. *Synthetic Metals*, 135-136:115–117, 2003. Cited By (since 1996): 21.

- [165] J. Huang, P. F. Miller, J. S. Wilson, A. J. De Mello, J. C. De Mello, and D. D. C. Bradley. Investigation of the effects of doping and post-deposition treatments on the conductivity, morphology, and work function of poly(3,4-ethylenedioxythiophene)/poly(styrenesulfonate) films. *Advanced Functional Materials*, 15(2):290–296, 2005. Cited By (since 1996): 22.
- [166] T. M. Brown, J. S. Kim, R. H. Friend, F. Cacialli, R. Daik, and W. J. Feast. Built-in field electroabsorption spectroscopy of polymer light-emitting diodes incorporating a doped poly(3,4-ethylene dioxythiophene) hole injection layer. *Applied Physics Letters*, 75(12):1679–1681, 1999. Cited By (since 1996): 185.
- [167] J. S. Kim, M. Granström, R. H. Friend, N. Johansson, W. R. Salaneck, R. Daik, W. J. Feast, and F. Cacialli. Indium-tin oxide treatments for single- and double-layer polymeric light-emitting diodes: The relation between the anode physical, chemical, and morphological properties and the device performance. *Journal of Applied Physics*, 84(12):6859–6870, 1998. Cited By (since 1996): 344.
- [168] K. Nagesh, D. Gupta, D. Kabra, K. S. Narayan, and S. Ramakrishnan. Tunable two-colour patterning of MEHPPV from a single precursor. *Journal of Materials Chemistry*, 17(17):1682–1686, 2007.
- [169] M. G. Harrison, J. Grüner, and G. C. W. Spencer. Analysis of the photocurrent action spectra of MEH-PPV polymer photodiodes. *Physical Review B - Condensed Matter and Materials Physics*, 55(12):7831–7849, 1997. Cited By (since 1996): 96.
- [170] L. Bozano, S. A. Carter, J. C. Scott, G. G. Malliaras, and P. J. Brock. Temperature- and field-dependent electron and hole mobilities in polymer light-emitting diodes. *Applied Physics Letters*, 74(8):1132–1134, 1999. Cited By (since 1996): 172.
- [171] E. Frankevich, Y. Maruyama, and H. Ogata. Mobility of charge carriers in vapor-phase grown single crystal C₆₀. *Chem. Phys. Lett.*, 214(1):39–44, 1993. Cited By (since 1996): 39.
- [172] G. Yu and A. J. Heeger. Charge separation and photovoltaic conversion in polymer composites with internal donor/acceptor heterojunctions. *Journal of Applied Physics*, 78(7):4510–4515, 1995. Cited By (since 1996): 351.
- [173] A. J. Breeze, Z. Schlesinger, S. A. Carter, H. Tillmann, and H.-H. Hörhold. Improving power efficiencies in polymer - polymer blend photovoltaics. *Solar Energy Materials and Solar Cells*, 83(2-3):263–271, 2004. Cited By (since 1996): 29.

- [174] T. Kietzke, H.-H. Hörhold, and D. Neher. Efficient polymer solar cells based on M3EH-PPV. *Chemistry of Materials*, 17(26):6532–6537, 2005. Cited By (since 1996): 31.
- [175] A. C. Arias. Vertically segregated polymer blends: Their use in organic electronics. *Journal of Macromolecular Science: Polymer Reviews*, 46(1):103–125, 2006. Cited By (since 1996): 3.
- [176] A. C. Arias, N. Corcoran, M. Banach, R. H. Friend, J. D. MacKenzie, and W. T. S. Huck. Vertically segregated polymer-blend photovoltaic thin-film structures through surface-mediated solution processing. *Applied Physics Letters*, 80(10):1695, 2002. Cited By (since 1996): 77.
- [177] L.-L. Chua, P. K. H. Ho, H. Sirringhaus, and R. H. Friend. Observation of field-effect transistor behavior at self-organized interfaces. *Advanced Materials*, 16(18):1609–1615, 2004. Cited By (since 1996): 25.
- [178] A. Salleo and A. C. Arias. Solution based self-assembly of an array of polymeric thin-film transistors. *Advanced Materials*, 19(21):3540–3543, 2007.
- [179] K. Nagesh, D. Kabra, K.S. Narayan, and S Ramakrishnan. Modulating phase-separation in blends of MEHPPV-x with different conjugation lengths. *Synthetic Metals*, 155(2):295–298, 2005.
- [180] M. Berggren, A. Dodabalapur, R.E. Slusher, and Z. Bao. Light amplification in organic thin films using cascade energy transfer. *Nature*, 389:466, 1997.
- [181] L. Chen, L. S. Roman, D. M. Johansson, M. Svensson, M. R. Andersson, R. A. J. Janssen, and O. Inganäs. Excitation transfer in polymer photodiodes for enhanced quantum efficiency. *Advanced Materials*, 12(15):1110–1114, 2000. Cited By (since 1996): 32.
- [182] Y. G. Kim, B. C. Thompson, N. Ananthakrishnan, G. Padmanaban, S. Ramakrishnan, and J. R. Reynolds. Variable band gap conjugated polymers for optoelectronic and redox applications. *Journal of Materials Research*, 20(12):3188–3198, 2005. Cited By (since 1996): 8.
- [183] A. J. Breeze, Z. Schlesinger, S. A. Carter, and P. J. Brock. Charge transport in TiO₂/MEHPPV polymer photovoltaics. *Physical Review B - Condensed Matter and Materials Physics*, 64(12):1252051–1252059, 2001. Cited By (since 1996): 120.
- [184] L. P. Candeias, F. C. Grozema, G. Padmanaban, S. Ramakrishnan, L. D. A. Siebbeles, and J. M. Warman. Positive charge carriers on isolated chains of MEHPPV with broken conjugation: Optical absorption and mobility.

- Journal of Physical Chemistry B*, 107(7):1554–1558, 2003. Cited By (since 1996): 25.
- [185] C. H. Lee, G. Yu, D. Moses, and A. J. Heeger. Picosecond transient photoconductivity in poly(p-phenylenevinylene). *Physical Review B*, 49(4):2396–2407, 1994. Cited By (since 1996): 78.
- [186] G. Padmanaban and S. Ramakrishnan. Conjugation length control in soluble poly[2-methoxy-5-((2'-ethylhexyl)oxy)-1,4-phenylenevinylene] (MEHPPV): Synthesis, optical properties, and energy transfer. *Journal of the American Chemical Society*, 122(10):2244–2251, 2000. Cited By (since 1996): 81.
- [187] G. Padmanaban and S. Ramakrishnan. Fluorescence spectroscopic studies of solvent- and temperature-induced conformational transition in segmented poly[2-methoxy-5-(2'-ethylhexyl)oxy-1,4-phenylenevinylene] (MEHPPV). *Journal of Physical Chemistry B*, 108(39):14933–14941, 2004. Cited By (since 1996): 21.
- [188] J. L. Young, Y. K. Doo, J. K. Grey, and P. F. Barbara. Variable temperature single-molecule dynamics of MEHPPV. *ChemPhysChem*, 6(11):2404–2409, 2005. Cited By (since 1996): 2.
- [189] C. J. Brabec, F. Padinger, N. S. Sariciftci, and J. C. Hummelen. Photovoltaic properties of conjugated polymer/methanofullerene composites embedded in a polystyrene matrix. *Journal of Applied Physics*, 85(9):6866–6872, 1999. Cited By (since 1996): 84.
- [190] H. Benten, M. Ogawa, H. Ohkita, and S. Ito. Design of multilayered nanostructures and donor-acceptor interfaces in solution-processed thin-film organic solar cells. *Advanced Functional Materials*, 18(10):1563–1572, 2008.
- [191] P. C. Dastoor, C. R. McNeill, H. Frohne, C. J. Foster, B. Dean, C. J. Fell, W. J. Belcher, W. M. Campbell, D. L. Officer, I. M. Blake, P. Thordarson, M. J. Crossley, N. S. Hush, and J. R. Reimers. Understanding and improving solid-state polymer/ C_{60} -fullerene bulk-heterojunction solar cells using ternary porphyrin blends. *Journal of Physical Chemistry C*, 111(42):15415–15426, 2007. Cited By (since 1996): 1.
- [192] M. Jørgensen, K. Norrman, and F. C. Krebs. Stability/degradation of polymer solar cells. *Solar Energy Materials and Solar Cells*, 92(7):686–714, 2008.
- [193] F. C. Krebs and K. Norrman. Analysis of the failure mechanism for a stable organic photovoltaic during 10,000 h of testing. *Progress in Photovoltaics: Research and Applications*, 15(8):697–712, 2007. Cited By (since 1996): 9.

- [194] P. Peumans and S. R. Forrest. Separation of geminate charge-pairs at donor-acceptor interfaces in disordered solids. *Chemical Physics Letters*, 398(1-3):27–31, 2004. Cited By (since 1996): 29.
- [195] M. Lenes, L. J. A. Koster, V. D. Mihailetschi, and P. W. M. Blom. Thickness dependence of the efficiency of polymer:fullerene bulk heterojunction solar cells. *Applied Physics Letters*, 88(24), 2006. Cited By (since 1996): 1.
- [196] M. C. Scharber, D. Mühlbacher, M. Koppe, P. Denk, C. Waldauf, A. J. Heeger, and C. J. Brabec. Design rules for donors in bulk-heterojunction solar cells-towards 10% energy-conversion efficiency. *Advanced Materials*, 18(6):789–794, 2006. Cited By (since 1996): 105.
- [197] P. Schilinsky, C. Waldauf, J. Hauch, and C. J. Brabec. Simulation of light intensity dependent current characteristics of polymer solar cells. *Journal of Applied Physics*, 95(5):2816–2819, 2004. Cited By (since 1996): 50.
- [198] D. Gupta, D. Kabra, N. Kolishetti, S. Ramakrishnan, and K. S. Narayan. An efficient bulk-heterojunction photovoltaic cell based on energy transfer in graded-bandgap polymers. *Advanced Functional Materials*, 17(2):226–232, 2007. Cited By (since 1996): 1.
- [199] M. Granström, K. Petritsch, A. C. Arias, A. Lux, M. R. Andersson, and R. H. Friend. Laminated fabrication of polymeric photovoltaic diodes. *Nature*, 395(6699):257–260, 1998. Cited By (since 1996): 602.
- [200] M. M. Mandoc, W. Veurman, L. J. A. Koster, B. De Boer, and P. W. M. Blom. Origin of the reduced fill factor and photocurrent in MD-MOPPV:PCNEPV all-polymer solar cells. *Advanced Functional Materials*, 17(13):2167–2173, 2007. Cited By (since 1996): 3.
- [201] S.B. Rim, R. F. Fink, J. C. Schoneboom, P. Erk, and P. Peumans. Effect of molecular packing on the exciton diffusion length in organic solar cells. *Applied Physics Letters*, 91(17):173504, 2007.
- [202] Q. L. Song, M. L. Wang, E. G. Obbard, X. Y. Sun, X. M. Ding, X. Y. Hou, and C. M. Li. Degradation of small-molecule organic solar cells. *Applied Physics Letters*, 89(25):251118, 2006. Cited By (since 1996): 1.
- [203] V. P. Singh, R. S. Singh, B. Parthasarathy, A. Aguilera, J. Anthony, and M. Payne. Copper-phthalocyanine-based organic solar cells with high open-circuit voltage. *Applied Physics Letters*, 86(8):1–3, 2005. Cited By (since 1996): 1.

- [204] M. Glatthaar, M. Riede, N. Keegan, K. Sylvester-Hvid, B. Zimmermann, M. Niggemann, A. Hinsch, and A. Gombert. Efficiency limiting factors of organic bulk heterojunction solar cells identified by electrical impedance spectroscopy. *Solar Energy Materials and Solar Cells*, 91(5):390–393, 2007. Cited By (since 1996): 9.
- [205] V. Djara and J. C. Bernède. Effect of the interface morphology on the fill factor of plastic solar cells. *Thin Solid Films*, 493(1-2):273–277, 2005. Cited By (since 1996): 2.
- [206] E. Ahlswede, J. Hanisch, and M. Powalla. Influence of cathode sputter deposition on organic solar cells. *Applied Physics Letters*, 90(6):063513, 2007.
- [207] M. Hiramoto, T. Imahigashi, and M. Yokoyama. Photocurrent multiplication in organic pigment films. *Applied Physics Letters*, 64(2):187–189, 1994. Cited By (since 1996): 42.
- [208] M. Hiramoto, K.-I. Nakayama, T. Katsume, and M. Yokoyama. Field-activated structural traps at organic pigment/metal interfaces causing photocurrent multiplication phenomena. *Applied Physics Letters*, 73(18):2627–2629, 1998. Cited By (since 1996): 9.
- [209] M. Hiramoto, K. Nakayama, I. Sato, H. Kumaoka, and M. Yokoyama. Photocurrent multiplication phenomena at organic/metal and organic/organic interfaces. *Thin Solid Films*, 331(1-2):71–75, 1998. Cited By (since 1996): 14.
- [210] S. T. Zhang, Y. C. Zhou, J. M. Zhao, Y. Q. Zhan, Z. J. Wang, Y. Wu, X. M. Ding, and X. Y. Hou. Role of hole playing in improving performance of organic light-emitting devices with an Al_2O_3 layer inserted at the cathode-organic interface. *Applied Physics Letters*, 89(4):043502, 2006. Cited By (since 1996): 1.
- [211] G. Li, V. Shrotriya, Y. Yao, and Y. Yang. Investigation of annealing effects and film thickness dependence of polymer solar cells based on poly(3-hexylthiophene). *Journal of Applied Physics*, 98(4):1–5, 2005. Cited By (since 1996): 10.
- [212] D. Gupta, M. Bag, and K. S. Narayan. Correlating reduced fill factor in polymer solar cells to contact effects. *Applied Physics Letters*, 92(9):093301, 2008.
- [213] G. P. Smestad, F. C. Krebs, C. G. Lampert, C. G. Granqvist, K. L. Chopra, X. Mathew, and H. Takakura. Reporting solar cell efficiencies in solar energy materials and solar cells. *Solar Energy Materials and Solar Cells*, 92(4):371–373.

- [214] V. Shrotriya, G. Li, Y. Yao, T. Moriarty, K. Emery, and Y. Yang. Accurate measurement and characterization of organic solar cells. *Advanced Functional Materials*, 16(15):2016–2023, 2006. Cited By (since 1996): 30.
- [215] K. Kim, J. Liu, M. A. G. Namboothiry, and D. L. Carroll. Roles of donor and acceptor nanodomains in 6% efficient thermally annealed polymer photovoltaics. *Applied Physics Letters*, 90(16):163511, 2007. Cited By (since 1996): 3.
- [216] D. L. Carroll, J. Liu, M. Namboothiry, and K. Kim. Response to comment on “roles of donor and acceptor nanodomains in 6% efficient thermally annealed polymer photovoltaics” (appl. phys. lett. 91, 266101 (2007)). *Applied Physics Letters*, 91(26):266102, 2007.
- [217] A. Cravino, P. Schilinsky, and C. J. Brabec. Characterization of organic solar cells: The importance of device layout. *Advanced Functional Materials*, 17(18):3906–3910, 2007. Cited By (since 1996): 1.
- [218] M.-S. Kim, M.-G. Kang, L. J. Guo, and J. Kim. Choice of electrode geometry for accurate measurement of organic photovoltaic cell performance. *Applied Physics Letters*, 92(13):133301, 2008.
- [219] J. Krc, M. Zeman, F. Smole, and M. Topic. Optical modeling of a-si:h solar cells deposited on textured glass/sno₂ substrates. *Journal of Applied Physics*, 92(2):749, 2002. Cited By (since 1996): 19.
- [220] T. Wilson and E. M. McCabe. Distribution of charge carriers generated in a semiconductor by a focused convergent light beam. *Journal of Applied Physics*, 59(8):2638–2642, 1986. Cited By (since 1996): 3.
- [221] S. Ito, Md K. Nazeeruddin, P. Liska, P. Comte, R. Charvet, P. Pechy, M. Jirousek, A. Kay, S. M. Zakeeruddin, and M. Gratzel. Photovoltaic characterization of dye-sensitized solar cells: Effect of device masking on conversion efficiency. *Progress in Photovoltaics: Research and Applications*, 14(7):589–601, 2006. Cited By (since 1996): 15.
- [222] M. J. Currie, J. K. Mapel, T. D. Heidel, S. Goffri, and M. A. Baldo. High-efficiency organic solar concentrators for photovoltaics. *Science*, 321(5886):226–228, 2008.
- [223] D. Kabra and K. S. Narayan. Direct estimate of transport length scales in semiconducting polymers. *Advanced Materials*, 19(11):1465–1470, 2007.
- [224] A. K. Pandey, J. M. Nunzi, B. Ratier, and A. Moliton. Size effect on organic optoelectronics devices: Example of photovoltaic cell efficiency. *Physics Letters, Section A: General, Atomic and Solid State Physics*, 372(8):1333–1336, 2008.

- [225] C. Lungenschmied, G. Dennler, H. Neugebauer, S. N. Sariciftci, M. Glatthaar, T. Meyer, and A. Meyer. Flexible, long-lived, large-area, organic solar cells. *Solar Energy Materials and Solar Cells*, 91(5):379–384, 2007. Cited By (since 1996): 24.
- [226] M. A. Green. *Solar cells, operating principles, technology and system applications*. University of New South Wales, Kensington, NSW 2033, December 1998.

621.312 44
P08

04 MAR 2009

Recd on 05/1/09

JNCASR

592J

LIBRARY